Architecting Superatomic Metal Chalcogenide Clusters for Materials Design

Andrew Pinkard

Submitted in partial fulfillment of the requirements for the degree of Doctor of

Philosophy in the Graduate School of Arts and Sciences

Columbia University

2018

ABSTRACT

Architecting Superatomic Metal Chalcogenide Clusters for Materials Design

Andrew Pinkard

This dissertation describes and summarizes the research I performed as a member of the Roy group. The Roy group uses molecular clusters as nanoscale building blocks for new materials, in addition to several other topics of related interest including the design and synthesis of molecular wires to study the movement of electrons (conductance) at the molecular level.

Chapter 1 introduces molecular clusters as superatomic nanoscale building blocks and describes how superatomic crystals, analogous to ionic crystals, can be controllably assembled from these building blocks. Next, Chapter 2 examines how the atomic properties of ionization energy and electron affinity can be extended to superatoms by investigating the $Co_6S_8(PEt_3)_6(CO)_{6-x}$ family of clusters. As the degree of cabonylation increases, the superatom moves from alkali-like to halogen-like behavior; i.e., it becomes harder to ionize and easier to add an electron to the superatom as PEt_3 ligands are replaced with CO ligands while still maintaining the overall electron count of the cluster. Chapter 3 then moves to discuss how the related building blocks, $Co_6Te_8(PEt_3)_6$ and its derivatives, can be assembled into superatomic crystals using the electron-accepting $Fe_8O_4pz_{12}Cl_4$ cluster. Chapter 4 then uses this same $Fe_8O_4pz_{12}Cl_4$ cluster as a probe for singlet fission triplet dynamics by functionalizing this cluster with a singlet fission chromophore. Chapter 5 continues the idea of ligand design by exploring a series of

oligophenylenediamine molecules capable of binding to gold (and presumably other metals), and it is observed that the conductance dramatically increases by applying a high positive bias to the molecules when they are bound to the tips of two gold electrodes. This dissertation concludes with Chapter 6, which discusses how new cobalt chalcogenide materials prepared from superatomic precursors can be deployed as new battery electrode materials for lithium and sodium ion batteries. Each of these chapters help illustrate how synthetic chemistry can be used to both elucidate interesting chemical phenomena and to design new materials with tailored properties.

Table of Contents

LIST OF FIGURES AND TABLES

ACKNOWLEDGEMENTS

I begin by acknowledging and thanking each and every excellent teacher, instructor, and professor I've had the privilege to share a classroom. These teachers instilled in me not only a fundamental basis of the scientific process, but also an interest, a passion, and a sense of wonder in science and the natural world. Without their teachings and encouragement, I would not have had the ability or the confidence to pursue an advanced degree in chemistry, and I am immensely grateful for their help. I want to specifically acknowledge professor Nancy Lee of MiraCosta College whose passion for teaching chemistry convinced me to pursue a degree in chemistry.

I sincerely thank Dr. Todd Deutsch of the National Renewable Energy Laboratory who gave me one of the best opportunities of my life thus far to do research at this amazing laboratory. His interest in quality science taught me how to perform proper electrochemical measurements and how to analyze the scientific literature with a keen, discerning eye. His mentorship inspired me to pursue a graduate degree and his encouragement and support helped me to believe that I could accomplish this goal. And his light-heartedness and humor showed me that scientists can also be humans. I wouldn't have gotten to where I am without him.

I also thank Dr. Lisa Nadolny of Celgene who gave me my first opportunity in research outside of academia. She taught me the fundamentals of organic synthetic chemistry, being both knowledgeable and down-to-earth, a combination of qualities that can be difficult to come across. Without the opportunities she gave me as a summer intern at Celgene, I would not have the knowledge or skills that I needed to pursue and complete a Ph. D. in chemistry. She taught me that chemistry can be a combination of

useful, practical, efficient, and life-changing, and I enjoyed every minute of my time at Celgene because of her mentorship.

Next, I want to acknowledge Bonnie Choi and Evan O'Brien who started this journey in the Roy group together with me as doe-eyed first year graduate students. We built the Roy lab from the ground up and it was our hard work and determination that got the lab going. They have also been some of my best friends in graduate school whose love and support I could not do without in finishing this degree.

I want to also acknowledge Anouck Champsaur of the Nuckolls group who worked extensively on molecular clusters. Her hard work and fearlessness in exploring materials designed with these interesting, yet challenging, molecules laid the foundations of a powerful research program in this area at Columbia. She was always a source of knowledge, help, and inspiration, and she felt like an honorary member of the Roy Lab. She was indispensable in understanding how to work with the molecular clusters we commonly used in the Roy group, and my work would have been almost impossible without her support and guidance.

I also acknowledge the many undergraduates who have done research in our lab, specifically Ari Turkiewicz, Chiara Butler, and Ivy Huang. Their interest in scientific research at such a young age was indispensable in making progress on many projects in the Roy Lab, including my own. They tackled, and in many cases conquered, projects that would have been daunting for me as an undergraduate, and they've gone on to pursue research in materials chemistry or professions in the chemical industry.

Next, I want to acknowledge my committee members, my professor Xavier, Roy, Prof. Colin Nuckolls, Prof. Latha Venkataraman, and Dr. Mike Steigerwarld whose

helpful conversations, scientific insights, and kind words in passing in the hallway were a source of inspiration in motivation during some of my darkest times in graduate school. With the opportunity they afforded me, I could not have completed this disagree. I've appreciated their support and learned an immense amount about science and academic research from their examples.

I thank the many friends I've made during graduate school both within and outside of the chemistry department. Their friendship was essential for completing this process and their presence necessary for my mental well-being.

Last, I want to thank Drs. Dat Hoang, Jonathan Kuo, and Travis Valdez, and Nate Schuster, who all completed their graduate degrees at Columbia while I was a graduate student in the chemistry department, along with Dr. Bijoy Desai, a postdoctoral researcher in the Gonzalez group in the chemistry department. Their friendship, support, and love helped me to believe in myself as both a scientist and a person. They taught me the importance of being a whole person, not just a researcher, and modeled how to be a confident, strong, and secure human being. I will always look back at my time with these individuals fondly and happily.

Preamble

Elucidating the connection between how interactions of matter at the nanoscale affect its macroscale properties is the heart of materials chemistry and is the driving force for research in the Roy group. In making progress towards this goal, the group uses discrete aggregates of atoms called molecular clusters as nanoscale building blocks to design and tailor materials with desired properties. Clusters contain a diverse set of chemical interactions (covalent, ionic, metal-metal, metal-ligand, ligand-ligand, etc.) and some of these clusters can behave as nanoscale versions of the very atoms that compose the periodic table. In this respect, the group often refers to clusters as "superatoms" to reflect this analogy. This broad research interest requires interplay from several major subdivisions of chemistry – organic, inorganic, physical, and theoretical – in order to synthesize, characterize, and understand how these superatomic building blocks assemble into bulk materials. Specifically, organic chemistry is used in designing ligands to support the inorganic cores of many of these cluster building blocks, and physical chemistry is used to understand the properties of these clusters and the resultant materials properties, while theoretical chemistry used to explain and rationalize the properties and trends that are observed.

In this context, my research in the Roy lab has been varied and diverse as opposed to focused and niche. I have worked on a variety of projects including the design and synthesis of novel inorganic clusters, ligand design and synthesis, controlling cluster-cluster interactions to direct self-assembly into the solid-state, solid-state chemistry of inorganic clusters, designing and synthesizing molecular wires, and deploying cluster-based materials in new battery materials, among other projects. While seemingly

1

disparate, these projects all share the motif of using synthetic chemistry to design and understand the evolution of nanoscale properties into bulk properties of materials.

This dissertation was constructed by integrating several of these research projects that highlight the work I've carried out in the Roy group. Chapter 1 introduces the concept of using molecular clusters as nanoscale building blocks for materials design by using several recent examples from the group to illustrate this concept, a topic which I recently authored a review. Chapter 2 then moves to discuss recent work done by myself, as well as collaborators from the Bowen (John Hopkins University) and Khanna (Virginia Commonwealth University) groups, in understanding precisely how atomic properties – ionization energy and electron affinity – manifest themselves in superatoms. Next, Chapter 3 discusses the assembly of these superatoms into superatomic crystals and how ligand modification can change the crystal packing in a tunable way useful to materials design. Chapter 4 continues with the idea of ligand modification by demonstrating how ligands can be designed for molecular clusters in a way that allows for interesting physical phenomena such as singlet fission to be further studied and understood. In Chapter 5, I then move to discuss how molecular wires that can coordinate to metal centers (i.e. those in clusters or other nanoscale building blocks) can be synthesized to study how electrons move through these ligands as the molecular scale. Finally, Chapter 6 concludes by examining how cluster-assembled materials can be used to make new battery electrodes for both lithium and sodium ion batteries.

From my work on these projects, I have learned how to use synthetic chemistry as a powerful tool in both the design and understanding of materials, and I will demonstrate this throughout this dissertation.

Chapter 1: Inorganic Clusters as Superatomic Building Blocks in Materials Chemistry

1.1: Preface

This chapter was adapted in part from the review "Molecular Clusters: Nanoscale Building Blocks for Solid-State Materials" published in Accounts of Chemical Research. I authored this review along with Dr. Anouck Champsaur and Prof. Xavier Roy where we reviewed recent efforts of the Roy lab and others in using superatomic inorganic clusters as nanoscale building blocks towards new materials. The results of my recent work, along with others, is highlighted and contextualized and demonstrates the promise of using molecular clusters to design and architect new materials.

1.2: Introduction

The rational design of functional materials is a major endeavor in modern materials chemistry. Driven by ever-increasing demands for new sources of energy and its subsequent storage, as well as the rapid miniaturization of electronic devices, new materials are required to meet these societal challenges. One attractive approach towards synthesizing these new kinds of materials is to design nanoscale building blocks that can be rationally programmed, controlled, and self-assembled into bulk hierarchical materials. Nanocrystals, for example, have been extensively explored as building blocks to assemble superlattices exhibiting remarkable tunability and functionalities.[1–3] These materials, however, intrinsically lack atomic precision owing to the polydispersity and complex surface chemistry of nanocrystals, creating challenges in both the design and control of the resulting solids.

In this context, molecular clusters are an attractive set of building blocks as they are atomically precise and structurally and compositionally diverse.[4,5] Due to the pioneering work of Holm,[6-9] Long,[10-12] Fedorov,[13-15] Fenske,[16-18] Steigerwald,[19-21] Dehnen,[22] and others, the literature is rich with a library of molecular clusters possessing a host of attractive properties including redox activity, large magnetic moments, and luminescence. And while there are past examples of molecular clusters used as building blocks in solid-state materials,[10,11,13,20,21,23-26] they have only recently re-emerged as valuable precursors towards new materials. Roy *et al.* has been at the forefront of this re-emergence,[27-40] focusing not only on developing novel synthetic strategies but also on the relationship between atomic structure and materials properties.

My initial interest in cluster-based materials was stimulated by the discovery that electron-rich metal chalcogenide clusters react with C_{60} fullerene to produce crystalline superatomic analogues of traditional ionic solids.[28] The resulting assemblies, which we now term superatomic crystals (SACs), are held together by electrostatic interactions in the solid state, analogous to how atoms (ions) are held together in ionic solids. Thus we often refer to our molecular clusters as "superatoms" because of this analogy. And indeed, recent work by Khanna supports the superatom concept for many of the most commonly utilized building blocks discussed herein.[41-43]

This thesis discusses my efforts in both designing molecular clusters to have desired tailored properties, as well as my efforts in constructing materials from cluster-based building blocks. This introduction highlights fundamental concepts of molecular clusters for the purpose of materials design, such as cluster cores and core nuclearity, as well as discussing the role of a passivating ligand shell. It also highlights some recent

examples of molecular clusters effectively designed into new materials and highlights some of their properties. The thesis then discusses molecular clusters focusing both on properties of discrete superatomic clusters to discussing their assembly into both crystalline and amorphous materials. Chapter 2 discusses a unique study of the "ionization energy" and "electron affinity," properties usually used to describe atoms, as applied to a family of carbonylated $Co_6S_8(CO)_x(PEt_3)_{6-x}$ superatoms. Next, Chapter 3 discusses crystalline assemblies of the related $Co_6Se_8(PR_3)_6$ and $Co_6Te_8(PR_3)_6$ (R = alkyl, aryl) with the electron-accepting $Fe_8O_4pz_{12}Cl_4$ molecular cluster (pz = pyrazolate, $C_3N_2H_3$). Chapter 4 then moves to discuss architecting ligands for the $Fe_8O_4pz_{12}Cl_4$ molecular cluster as a probe of the dynamics of singlet fission-generated triplet as a first step in attempting to design materials capable of harnessing the power of singlet fission. In keeping with ligand design as a tool for architecting molecular clusters, Chapter 5 discusses the conductance polyphenylenediamine molecular wires as a proxy of charge transfer through ligand backbones. The thesis then concludes with a discussion of recent work towards fabricating materials from $Co_6S_8(CO)_x(PEt_3)_{6-x}$ and using the resultant material as an electrode for lithium and sodium ion batteries.

1.3: Molecular Cluster Building Blocks: Design, Synthesis, and Functionalization

Molecular clusters are typically composed of an inorganic core and a passivating ligand shell, the latter affording both stability and solubility. While the library of molecular clusters is extensive, the work described herein focuses primarily on metal chalcogenide clusters. In this section, we discuss select features of these building blocks that enables assembly into solid-state materials.

1.4: Molecular Clusters: Cluster Cores

The metal chalcogenide core of a cluster governs its electronic, optical, and magnetic properties. Figure 1.1 presents two of the most common core structures used throughout the thesis, the M_6E_8 and M_4E_4 motifs, and some of their features are discussed.
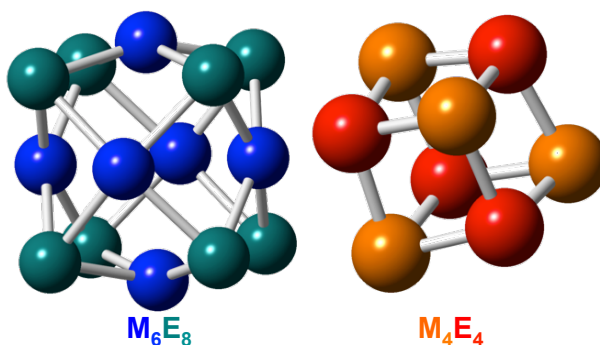
M_6E_8 M_4E_4

Figure 1.1. Structure of common cluster cores used throughout this work, octahedral M_6E_8 and cubane M_4E_4.

The M_6E_8 motif features an octahedron of metal atoms (M_6) co-centric with a cube of face-capping chalcogen atoms (E_8). Each metal atom is also capped with a ligand, L, typically a phosphine, to give molecules of the type $M_6E_8L_6$. Examples of this motif have been previously reviewed[5] and interest in this building block stems, in part, from its structural similarities to superconducting Chevrel phases,[22,44] which feature the Mo_6E_8 motif in the solid state.

Much of my initial synthetic effort has focused on the Co_6E_8 core, owing to its straightforward preparation, scalability, and amenability to a variety of phosphine ligands. Two strategies have been developed to synthesize $Co_6E_8(PR_3)_6$. The first method

uses Co^{2+} with excess phosphine and H_2S^{45} or $Se(TMS)_2^{18}$ (TMS = trimethylsilyl). The second approach uses dicobalt octacarbonyl, $Co_2(CO)_8$, with various phosphine chalcogenides.[21] These clusters are typically electron rich and tunable via modification of the phosphine ligand shell, a feature exploited to direct the assembly process into the solid state.

The M_4E_4 cubane structure is another common core structure used in this work. Clusters from this family contain a M_4E_4 core in which M and E alternate to approximate the vertices of a cube. This structural motif is ubiquitous in biological systems containing iron-sulfur proteins, where the Fe_4S_4 cluster acts as a redox-active catalytic site for a variety of transformations.[46] It was this redox activity that attracted attention to this family of clusters. In particular, the cluster $Fe_8O_4pz_{12}Cl_4$ (pz = pyrazolate, $C_3H_3N_2^-$), has good solubility in organic solvents and can reversibly accept up to four electrons.[47] With this particular cluster, the cubane Fe_4O_4 core is expanded with four additional Fe atoms connected to the oxo ligands and is supported by three pyrazolate ligands to form an approximately tetrahedral geometry. The four surface Fe ions are capped with Cl ligands, which can act as sites for further functionalization. This cluster has been studied in amorphous solid-state materials,[48] and this cluster has since assembled this building block into several of well-defined assemblies.[30,35]

1.5: Molecular Clusters: Ligand Shell

Molecular clusters are typically passivated by supporting ligands that provide stability and solution processability to the cluster cores. These ligands present both challenges and opportunities. For example, the ligands act as barriers limiting interactions between cluster cores, yet they can also be used to decorate the cores with functionalities

that can direct self-assembly or allow more fundamental studies of individual clusters.[27,35,36] To this end, a variety of more complex phosphine ligands has been developed that can be appended to the inorganic core (Figure 1.2). For example, starting with $Co_6E_8(PEt_3)_6$ as the parent cluster, an ethyl moiety can be replaced with 9-ethynylphenanthrene (Scheme 1c) to create a molecular recognition site for C_{60} fullerene. Additionally, the phosphines can be functionalized with a 4-(methylthio)phenyl moiety (Scheme 1d), which can be used to measure conductance through single Co_6S_8 molecular junctions.[27,36]

Scheme 1 highlights two general strategies toward functionalizing the $Co_6E_8P_6$ cluster: (1) designing the phosphine ligand and subsequently forming the Co_6E_8 core using this ligand (Scheme 1a, c, d) or (2) synthesizing the cluster with a phosphine that can be further modified after synthesis of the cluster core. Scheme 1b illustrates the latter approach where $Co_6Se_8(PEt_2PhBr)_6$ can be successively reacted with *n*-BuLi, CO_2 and HCl to produce the carboxylic acid-functionalized superatom $Co_6Se_8(PEt_2PhCOOH)_6$. This superatom can be used as a building block to form assemblies with distinct pre-assembled clusters in the framework.

a

b

c

d
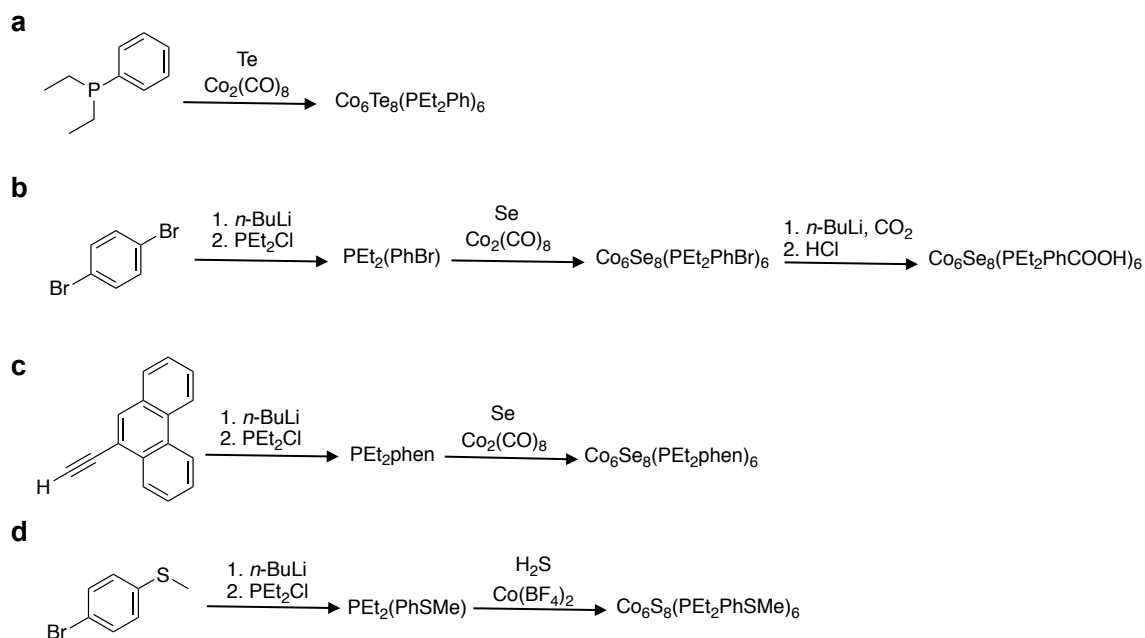
Figure 1.2. Scheme illustrating synthetic approach to functionalized $Co_6E_8L_6$ molecular clusters.

1.6: Molecular Clusters Assembly into SAC

There are several methods to create multi-component solid-state materials from molecular cluster superatomic building blocks. These building blocks combine atomic precision, stability, and tunability, and many of the resulting materials can be visualized as superatomic analogues of traditional binary atomic compounds. Different modes of assembly are highlighted, including inter-superatom charge transfer, molecular recognition, and directed formation of coordination frameworks.

1.7: SAC Self-Assembly: Charge Transfer

One simple strategy for creating SACs is to use charge transfer between neutral clusters and subsequent inter-cluster electrostatic attraction as a driving force for co-assembly and crystallization (Figure 1.3).
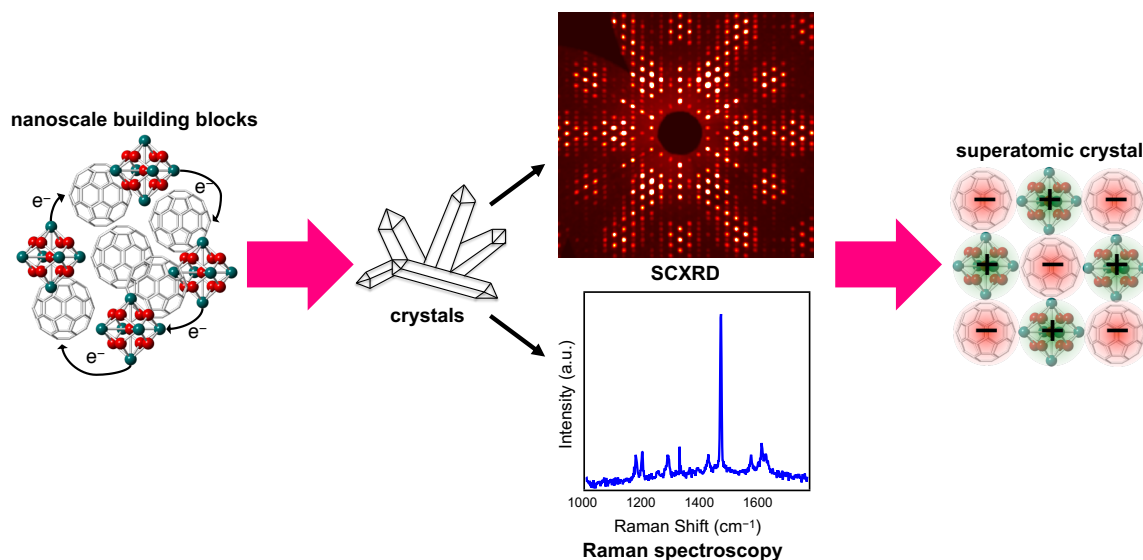
Figure 1.3. Schematic of SAC formation via charge transfer. The atomic structure of SACs is determined by SCXRD. The charge of each building block is inferred by examining changes in the vibrational frequency of the constituents (typically measured by Raman spectroscopy) and by bond distance analysis in the crystal structure.

To prepare these binary solid-state compounds, pairs of structurally and electronically complementary superatoms are combined in solution where one cluster is electron donating and the other is electron accepting. The internal structure of the constituent clusters remains unchanged, but charge is transferred amongst them, resulting in solid-state compounds that can be characterized by single crystal x-ray diffraction (SCXRD). More complex superstructures can be formed through simple modification of the superatom ligand spheres. Figure 1.4 presents a selection of superatomic crystals that have been prepared using this approach.

10
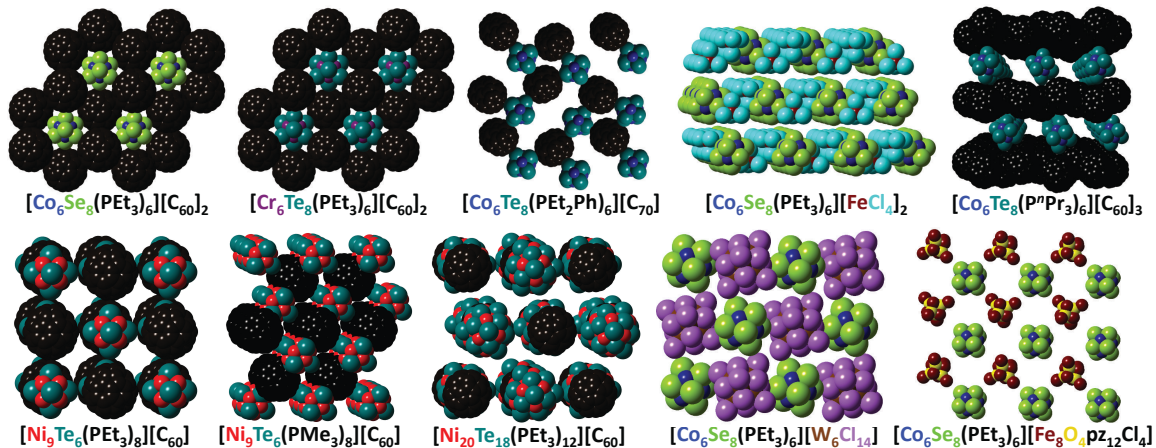
Figure 1.4. Library of SACs self-assembled using complementary charge transfer between superatomic building blocks. Supporting ligands omitted for clarity.

The SAC $[Co_6Te_8(PEt_3)_6][Fe_8O_4pz_{12}Cl_4]$ is an example of this phenomen using $Co_6Te_8(PEt_3)_6$ as the electron donor and $Fe_8O_4pz_{12}Cl_4$ as the electron acceptor. This work will be discussed in detail in Chapter 3 as an example of a SAC I synthesized using this approach.

Fullerenes, too, can be used as the electron-accepting component instead of $Fe_8O_4pz_{12}Cl_4$. Fullerenes are attractive building blocks due to their ability to accept electrons and mediate electronic coupling. Taking advantage of these features, a whole family of SACs has been synthesized by assembling C_{60} with a variety of electron-rich metal chalcogenide clusters. For example, electron-donating $Co_6Se_8(PEt_3)_6$, $Cr_6Te_8(PEt_3)_6$, $Ni_9Te_6(PEt_3)_8$ can be combined with C_{60} to form $Co_6Se_8(PEt_3)_6][C_{60}]_2$, $[Cr_6Te_8(PEt_3)_6][C_{60}]_2$, and $[Ni_9Te_6(PEt_3)_8][C_{60}]$, respectively.[28] The structure of these SACs is shown in Figure 1.4. The charge of the building blocks is determined through a combination of Raman spectroscopy and analysis of crystallographic data, outlined in Figure 1.3.

This strategy is not restricted to only C_{60} fullerene; different fullerenes such as C_{70} and endohedral C_{80} have been utilized as well. For example, reacting a nickel telluride cluster with the endohedral fullerene $Lu_3N@C_{80}$ in a mixture of toluene and quinoline produces black crystals of $[Ni_{12}Te_{12}(PEt_3)_8]_2[(Lu_3N@C_{80})2]$ in which $Ni_{12}Te_{12}(PEt_3)_8$ bears a 1+ charge and Lu3N@C80 dimerizes upon reduction to generate a dianion.[38] A similar dimerization process has been observed with C_{70} in recent work by Bejger *et al.*[49] However, this is the first example of a SAC containing an endohedral fullerene building block. The encapsulated Lu_3N molecule displays a unique orientation that is collinear and coplanar with the intercage carbon bond, not observed in the other endohedral fullerene dimers. This illustrates a unique way SACs can be tuned by inserting substituents inside the core of fullerene building blocks.
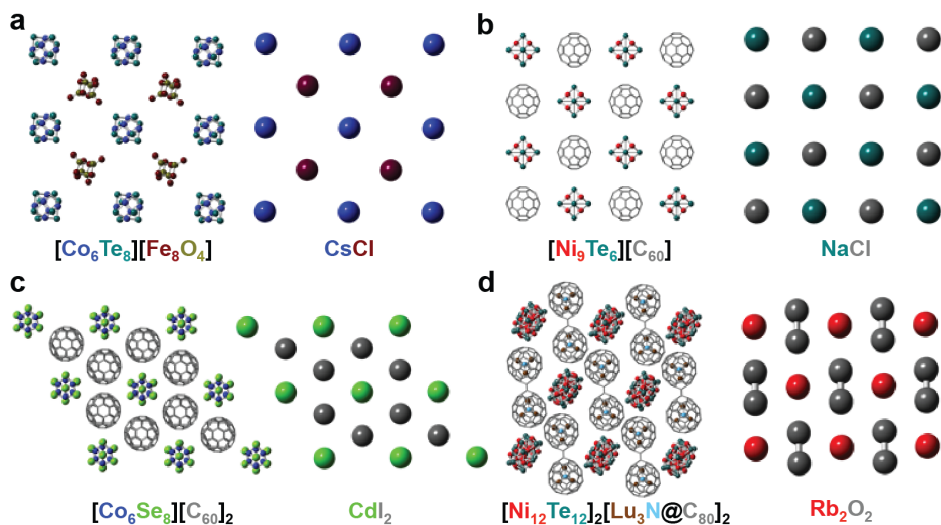
Figure 1.5. Select SACs and their atomic structural analogues.

Many SACs form structural analogues of traditional binary ionic compounds. Figure 1.5 illustrates this structural analogy for select examples. For example, the superstructure of $[Co_6Te_8(PEt_3)_6][Fe_8O_4pz_{12}Cl_4]$ is superatomic analogue of CsCl

illustrated in Figure 1.5a. Other simple lattice types include NaCl and CdI_2 for $[Ni_9Te_6(PEt_3)_8][C_{60}]$ and $[Co_6Se_8(PEt_3)_6][C_{60}]_2$, respectively (Figure 1.5b, 1.5c). Dimerization of the fullerene in $[Ni_{12}Te_{12}(PEt_3)_8]_2[(Lu_3N@C_{80})_2]$ produces a compound whose lattice can be visualized as the superatomic structural analogue of the binary atomic compound rubidium peroxide, Rb_2O_2 (Figure 1.5d).

1.7: SAC Self-Assembly: Molecular Recognition

Beyond simple charge transfer assemblies, the synthetic flexibility of molecular clusters offers new possibilities for directing assembly. For example, by designing molecular recognition motifs in the ligand shell of the Co_6E_8 cluster, new layered van der Waals (vdW) compounds have been prepared that self-assemble from a structure-directing building block and C_{60}.[32] The structure-directing building block is composed of the Co_6Se_8 core, decorated with six diethyl(9-ethynylphenanthrene)phosphine ligands (phen). While the phenanthrenes on each phosphine are flat and provide only weak vdW interactions with C_{60}, three phenanthrene groups can rotate in concert to form a host-guest structure with C_{60}. Reaction of $Co_6Se_8(phen)_6$ with C_{60} produces $[Co_6Se_8(phen)_6][C_{60}]_5$.
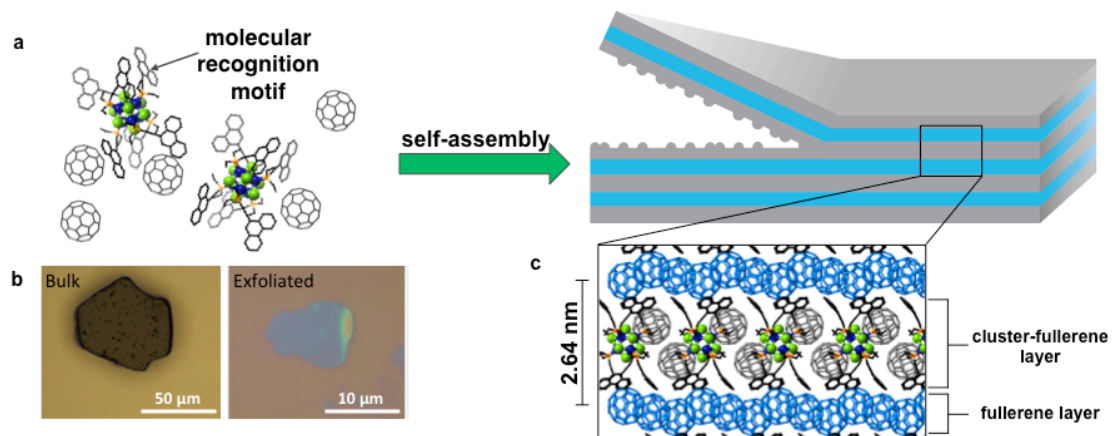
Figure 1.6. (a) Illustration of a nanoscale molecular recognition site directing self assembly of [Co6Se8(phen)6][C60]5. (b) Optical microscope images showing a crystal of the material before and after exfoliation. (c) Crystal structure differentiating the cluster-fullerene layer from the fullerene only layer.

The resulting compound, shown in Figure 1.6c, is a layered 2D material comprised of neutral, corrugated monolayers, which can be mechanically exfoliated. Notably, each fullerene layer is neutral and held together by vdW interactions. This conclusion is supported by the position of the A_{2g} mode of the fullerene in the Raman spectrum of the compound, which is identical to neutral C_{60}, and by the Co–P bond distances in the crystal structure, which are consistent with the neutral molecular cluster. The layered structure of $[Co_6Se_8(phen)_6][C_{60}]_5$ suggests it may be amenable to mechanical exfoliation. Figure 1.6b illustrates this process: under an optical microscope, exfoliated crystals display various colors that we interpret as interference fringes suggesting flakes of different thickness are produced by mechanical exfoliation. Atomic force microscopy (AFM) confirms that thin (~130 nm) flakes with a smooth surface can be obtained. Furthermore, electronic absorption spectroscopy suggests an optical gap of 390 ± 40 meV, consistent with the activation energy measured from electrical transport measurements. This value is decidedly distinct from that of bulk fullerene making this system ideal for measuring the effects of dimensional confinement of C_{60}.

14

1.7: SAC Self-Assembly: Intercalation

By analogy to traditional layered atomic materials, SACs can be intercalated with redox-active guests and maintain their atomic structure.
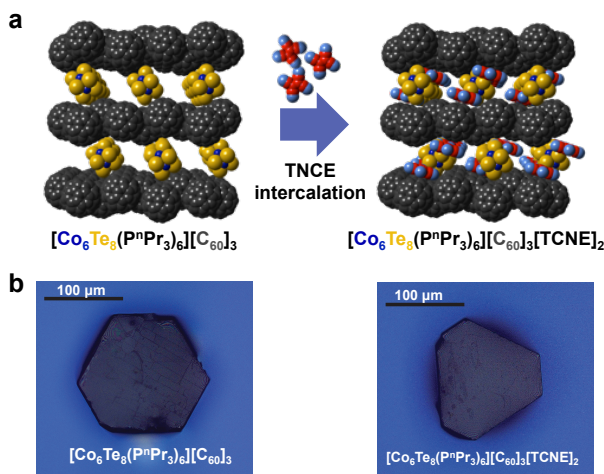
Figure 1.7. (a) SCXRD structure of host $[Co_6Te_8(P^nPr_3)_6][C_{60}]_3$ and intercalation compound $[Co_6Te_8(P^nPr_3)_6][C_{60}]_3[TCNE]_2$. (b) Image of a crystal before and after TCNE intercalation.

A new family of SAC was prepared by the intercalation of SAC $[Co_6Te_8(P^nPr_3)_6][C_{60}]_3$ whose layered structure is shown in Figure 1.7.[37] The pseudorhombohedral structure is composed of two alternating trigonal layers of $Co_6Te_8(P^nPr_3)_6$ and C_{60}. In the solid state, $Co_6Te_8(P^nPr_3)_6$ transfers one electron to the $3C_{60}$ motif, giving an overall charge state of $[Co_6Te_8(P^nPr_3)_6^+][C_{60}^{-1/3}]_3$. The intercalation compounds are synthesized by immersing crystals of $[Co_6Te_8(P^nPr_3)_6][C_{60}]_3$ in a solution of redox-active tetracyanoethylene (TCNE). Crystallographic analysis shows that the intercalation reaction preserves the crystallinity of the material, explicitly confirming the single-crystal-to-single-crystal transformation (Figure 1.7b). Figure 1.7a (right) shows the crystal structure of the intercalation compound $[Co_6Te_8(P^nPr_3)_6][C_{60}]_3[TCNE]_2$, which contains two ordered TCNE molecules occupying interstitial sites in the gap between the

C_{60} layers. The intercalation process is driven by the oxidation of the host by TCNE. To verify this, the charge of each component was determined using vibrational spectroscopy and SCXRD. These measurements indicate that the charges in the intercalation compound are $[Co_6Te_8(P^nPr_3)_6^{2+}][C_{60}^0]_3[TCNE^-]_2$. This intercalation strategy allows the optical, electronic, and magnetic properties SAC-based materials to be modulated in much the same way as has been used to tune atomic solids.

1.8: Collective Properties of SAC: Electronic Transport

In many respects, SACs behave less like molecular co-crystals and more like solid-state compounds. For example, several fullerene-based SACs exhibit thermally activated electronic transport. Two- and four-probe electrical resistivity measurements were performed on single crystals and pressed pellets of $[Cr_6Te_8(PEt_3)_6][C_{60}]_2$ and $[Co_6Se_8(PEt_3)_6][C_{60}]_2$ to determine their electrical properties.[28] The conductance (G) of these materials decreases exponentially with decreasing temperature, suggesting thermally activated behavior. The activation energy, E_a, can be calculated from the slope of the Arrhenius plot. It is found that E_a varies with the structure and composition of the SAC: Ea ~100, ~150, ~200 and ~400 meV for $[Cr_6Te_8(PEt_3)_6][C_{60}]_2$, $[Co_6Se_8(PEt_3)_6][C_{60}]_2$, $[Co_6Te_8(P^nPr_3)_6][C_{60}]_3$ and $[Co_6Se_8(phen)_6][C_{60}]5$, respectively.[28,32,37]

The electrical conductivity can be modified by inserting redox-active guests into the lattice. $[Co_6Te_8(P^nPr_3)_6][C_{60}]_3$ is an example of how the carrier density of the SAC can be tuned to modulate its electrical properties.[37] Figure 1.8a shows how the electrical conductivity (σ) of the intercalation compound $[Co_6Te_8(P^nPr_3)_6][C_{60}]_3[TCNE]_x$ changes with x. At room temperature, σ ~ 0.2 S m–1 for x = 0 and decreases monotonically by

16

four orders of magnitude as x increases. Simultaneously, the electrical transport activation energy increases from 200 to 850 meV as x increases. This increase of E_a agrees well with optical measurements showing a widening of the bandgap to ~0.65 eV upon TCNE intercalation.
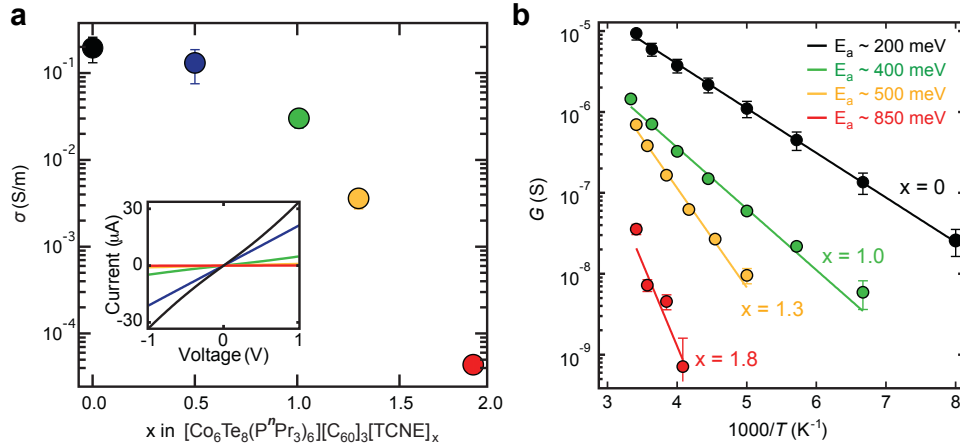
Figure 1.8. (a) Room-temperature σ as a function of x in $[Co_6Te_8(P^nPr_3)_6][C_{60}]_3[TCNE]_x$ inset: representative current versus voltage curves. (b) Plot of conductance (G) versus 1/T for $[Co_6Te_8(P^nPr_3)_6][C_{60}]_3[TCNE]_x$. The Arrhenius fits, shown as solid lines, are used to extract the activation energy E_a.

1.9: Collective Properties of SAC: Thermal Transport

In traditional atomic semiconductors, thermal energy is transported by quantized lattice vibrations (i.e. phonons). The atomically-precise hierarchical structure of SACs, composed of diverse intra- and inter-superatom interactions, gives rise to a more complex vibrational landscape, which offers unique opportunities to study the fundamental properties of phonons and can lead to unexpected thermal transport behaviors. In such materials, the superatoms are too small for bulk-like properties to emerge within individual clusters. Thermal transport cannot be understood by only considering the phonon spectra of the individual superatoms. Instead, the extended phonon states of the entire structure must be considered, in contrast with nanocrystal superlattices, which are

17

well described by effective medium approximations. Recently we showed thermal transport in SACs is mediated by two contributions: (i) intra-superatom vibrations, and (ii) collective inter-superatom phonons whose mean free paths can be modulated by the spacing and the strength of the interactions between the superatoms.[33] This second contribution is uniquely important and emerges as a result of the atomic precision of the lattice. Using a combination of SCXRD, differential scanning calorimetry (DSC), frequency domain thermoreflectance (FDTR), and DFT calculations, we investigated the thermal conductivity properties of single-component $Co_6E_8(PEt_3)_6$ (E = S, Se, Te) and binary $[Co_6E_8(PEt_3)_6][C_{60}]_2$. The calculated heat capacities of these compounds are consistently 20-35% lower than the experimental values measured by DSC (Figure 1.9a), a difference attributed to the collective low-frequency, inter-superatom vibrational modes that emerge upon crystallization and which are not captured by the calculations. This conclusion is further supported by FDTR thermal conductivity measurements: the thermal conductivity scales linearly with sound speed, a strong indication that thermal transport in SACs has dominant contributions from extended phonon states that naturally emerge from collective wave effects (Figure 1.9b).

The thermal conductivity of these SACs exhibits a peculiar temperature dependence. In particular, one material, $[Co_6Se_8(PEt_3)_6][C_{60}]_2$, exhibits an unusual transition from amorphous to crystalline thermal transport behavior at approximately 200 K (Figure 1.9c). This change is attributed to a structural phase transformation between a high-symmetry, dynamically-disordered phase at higher temperatures and a low-symmetry, highly-ordered phase at lower temperatures. Below the phase transition temperature, the free rotation of the C_{60} cages is suppressed and the material becomes

18

orientationally ordered. This reduces the scattering of phonons and increases their mean free path. The overall effect is that the thermal conductivity of the material increases rapidly with decreasing temperature, akin to crystalline atomic solids.
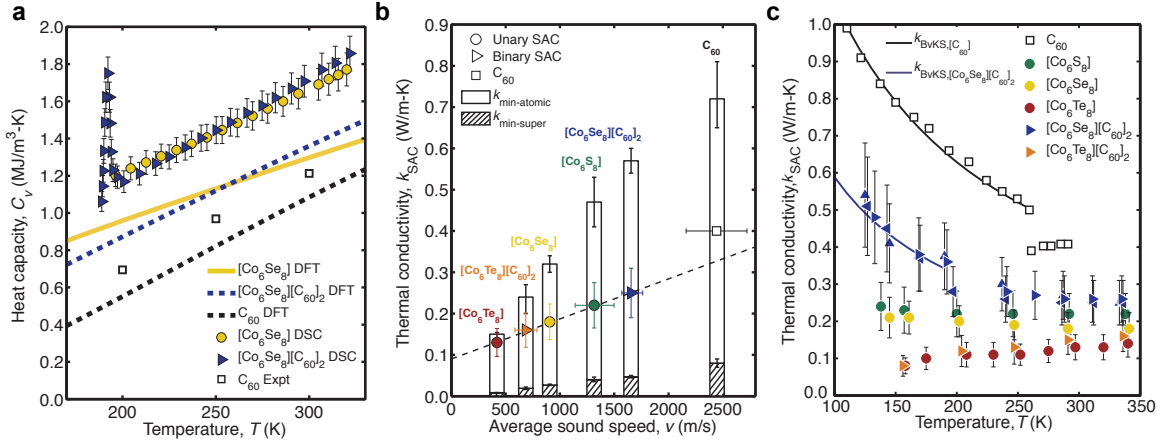
Figure 1.9. (a) Temperature dependence of the experimental (DSC) and calculated (DFT) heat capacities of $Co_6Se_8(PEt_3)_6$, C_{60}, and $[Co_6Se_8(PEt_3)_6][C_{60}]_2$. (b) Room temperature thermal conductivity of SACs (k_{SAC}) as a function of the sound speed. k_{SAC} is proportional to the average sound speed. The dotted line through the experimental data is a guide to the eye. The Cahill-Pohl minimum thermal conductivity calculations using the full SAC atomic density (kmin-atomic) and the SAC superatom density (kmin-super) bound our results. The dotted line through the experimental data is a guide to the eye. (c) Temperature dependence of k_{SAC}. The Born-von Karman k model for crystalline solids (k_{BvK}) provides a good fit to the low-temperature data of $[Co_6Se_8][C_{60}]_2$ and C_{60}.

1.9: Collective Properties of SAC: Magnetic Ordering

In atomic solids, localized spin centers can interact to produce long-range cooperative magnetic properties such as ferromagnetism or antiferromagnetism. Many inorganic molecular clusters possess large magnetic moments but their interaction is typically weak, thus preventing the observation of bulk magnetically ordered phases. Using superconducting quantum interference device (SQUID) magnetometry and muon spin relaxation, it has been demonstrated that in the SAC $[Ni_9Te_6(PEt_3)_8][C_{60}]$, the magnetic motifs of the Ni_9Te_6 cores spontaneously couple to stabilize a ferromagnetic ground state at low temperature,[29] studied theoretically by Khanna *et al.*[43] The

temperature dependence of the zero-field cooled (ZFC) and field cooled (FC) magnetizations for $[Ni_9Te_6(PEt_3)_8][C_{60}]$ clearly shows the ferromagnetic phase transition below ~4 K (Figure 1.10a). Muon spin relaxation measurements also confirm the ferromagnetic ground state.
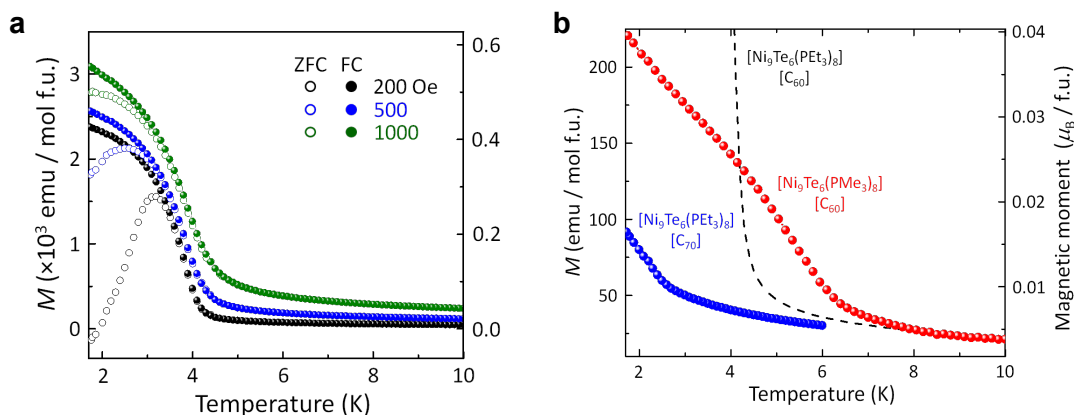
Figure 1.10. (a) Temperature dependence of the ZFC and FC magnetizations of $[Ni_9Te_6(PEt_3)_8][C_{60}]$ in external applied magnetic fields of 200, 500, and 1000 Oe. (b)Temperature dependence of the FC magnetizations of $[Ni_9Te_6(PEt_3)_8][C_{60}]$, $[Ni_9Te_6(PMe_3)_8][C_{60}]$, and $[Ni_9Te_6(PEt_3)_8][C_{70}]$ in an applied field of 100 Oe.

As a illustration of synthetic control, two additional structural analogues, $[Ni_9Te_6(PMe_3)_8][C_{60}]$ and $[Ni_9Te_6(PEt_3)_8][C_{70}]$, were prepared. The magnetic ordering temperature in $[Ni_9Te_6(PMe_3)_8][C_{60}]$ is higher than that of $[Ni_9Te_6(PEt_3)_8][C_{60}]$ as a result of closer physical proximity of the building blocks due to the smaller PMe_3 ligand (Figure 1.10b). Conversely, $[Ni_9Te_6(PEt_3)_8][C_{70}]$ has a lower magnetic ordering temperature than its C_{60} analogue due to the larger lattice parameter and the added orientational disorder of C_{70}. These results are an important step towards realizing the significant benefits of superatomic crystals: demonstrating that the magnetic behavior of the material is more than the simple average of the magnetic properties of the constituent subunits; and rational changes to the chemical structures of the subunits results in predictable changes in the collective properties of the solid.

20

1.9: Conclusion and Outlook

The bottom-up assembly of preformed molecular clusters towards well-defined hierarchical materials has proven to be a successful approach in the design of new functional materials. These materials exhibit collective physical properties that emerge as a result of their atomic precision. Work has been previously done to extensively modifying the building blocks with functional ligands. The thesis will continue by discussing superatoms more closely, as well as exploring charge transport between ligand and cluster core, ending with a study of battery electrodes synthesized from superatom precursors. Much like the materials discussed in this introduction, these materials hold new, exciting properties to explore.

1.9: References

(1) Collier, C. P.; Vossmeyer, T.; Heath, J. R. Nanocrystal Superlattices. *Annu. Rev. Phys. Chem.* **1998**, *49*, 371–404.

(2) Shevchenko, E. V.; Talapin, D. V.; Kotov, N. A.; O'Brien, S.; Murray, C. B. Structural Diversity in Binary Nanoparticle Superlattices. *Nature* **2006**, *439*, 55.

(3) Auyeung, E.; Cutler, J. I.; Macfarlane, R. J.; Jones, M. R.; Wu, J.; Liu, G.; Zhang, K.; Osberg, K. D.; Mirkin, C. A. Synthetically Programmable Nanoparticle Superlattices Using a Hollow Three-Dimensional Spacer Approach. *Nat. Nanotechnol.* **2012**, *7*, 24–28.

(4) Claridge, S. A.; Castleman, A. W.; Khanna, S. N.; Murray, C. B.; Sen, A.; Weiss, P. S. Cluster-Assembled Materials. *ACS Nano* **2009**, *3* (2), 244–255.

(5) Degroot, M. W.; Corrigan, J. F. High Nuclearity Clusters: Metal–Chalcogenide Polynuclear Complexes. In *Comprehensive Coordination Chemistry II*; Vol. 7, pp 57–123.

(6) Long, J. R.; McCarty, L. S.; Holm, R. H. A Solid-State Route to Molecular Clusters: Access to the Solution Chemistry of $[Re_6Q_8]^{2+}$ (Q = S, Se) Core-Containing Clusters via Dimensional Reduction. *J. Am. Chem. Soc.* **1996**, *118*, 4603–4616.

(7) Zheng, Z.; Long, J. R.; Holm, R. H. A Basis Set of Re_6Se_8 Cluster Building Blocks and Demonstration of Their Linking Capability: Directed Synthesis of an $Re_{12}Se_{16}$ Dicluster. *J. Am. Chem. Soc.* **1997**, *119*, 2163–2171.

(8) Franolic, J. D.; Long, J. R.; Holm, R. H. Comprehensive Tungsten-Iodine Cluster Chemistry: Isolated Intermediates in the Solid-State Nucleation of $[W_6I_{14}]^{2-}$. *J. Am. Chem. Soc.* **1995**, *117*, 8139–815.

(9) Long, J. R.; Williamson, A. S.; Holm, R. H. Dimensional Reduction of $Re_6Se_8Cl_2$: Sheets, Chains, and Discrete Clusters Composed of Chloride-Terminated $[Re_6Q_8]^{2+}$ (Q = S, Se) Cores. *Angew. Chem. Int. Ed. Engl.* **1995**, *34*, 226–229.

(10) Shores, M. P.; Beauvais, L. G.; Long, J. R. Cluster-Expanded Prussian Blue Analogues. *J. Am. Chem. Soc.* **1999**, *121*, 775–779.

(11) Tulsky, E. G.; Long, J. R. Dimensional Reduction: A Practical Formalism for Manipulating Solid Structures. *Chem. Mater.* **2001**, *13*, 1149–1166.

(12) Bennett, M. V.; Beauvais, L. G.; Shores, M. P.; Long, J. R. Expanded Prussian Blue Analogues Incorporating $[Re_6Se_8(CN)_6]^{3-/4-}$ Clusters: Adjusting Porosity via Charge Balance. *J. Am. Chem. Soc.* **2001**, *123*, 8022–8032.

(13) Mironov, Y. V.; Virovets, A. V.; Naumov, N. G.; Ikorskii, V. N.; Fedorov, V. E. Excision of the $\{Mo_6Se_8\}$ Cluster Core from a Chevrel Phase: Synthesis and Properties of the First Molybdenum Octahedral Cluster Selenocyanide Anions $[Mo_6Se_8(CN)_6]^{7-}$ and $[Mo_6S_8(CN)_6]^{6-}$. *Chem. Eur. J.* **2000**, *6*, 1361–1365.

(14) Yarovoi, S. S.; Mironov, Y. V.; Naumov, D. Y.; Gatilov, Y. V.; Kozlova, S. G.; Kim, S.-J.; Fedorov, V. E. Octahedral Hexahydroxo Rhenium Cluster Complexes $[Re_6Q_8(OH)_6]^{4-}$(Q = S, Se): Synthesis, Structure, and Properties. *Eur. J. Inorg. Chem.* **2005**, *2005*, 3945–3949.

(15) Shestopalov, M. A.; Mironov, Y. V.; Brylev, K. A.; Kozlova, S. G.; Fedorov, V. E.; Spies, H.; Pietzsch, H.-J.; Stephan, H.; Geipel, G.; Bernhard, G. Cluster Core Controlled Reactions of Substitution of Terminal Bromide Ligands by Triphenylphosphine in Octahedral Rhenium Chalcobromide Complexes. *J. Am. Chem. Soc.* **2007**, *129*, 3714–3721.

(16) Fenske, D.; Basoglu, R.; Hachgenei, J.; Rogel, F. Novel Clusters of Cobalt and Nickel with Organophosphorus Ligands. *Angew. Chem. Int. Ed. Engl.* **1984**, *23*, 160–162.

(17) Fenske, D.; Ohmer, J.; Hachgenei, J. Neue Co- Und Ni-Cluster Mit Se Und PPh_3 Als Liganden: $[Co_4(\mu_3\text{-Se})_4(PPh_3)_4]$, $[Co_6(\mu_3\text{-Se})_8(PPh_3)_6]$, $[Co_9(\mu_4\text{-Se})_3(\mu_3\text{-Se})_8(PPh_3)_6]$ Und $[Ni_{34}(\mu_5\text{-Se})_2(\mu_4\text{-Se})_{20}(PPh_3)_{10}]$. *Angew. Chem.* **1985**, *97*, 993–995.

(18) Fenske, D.; Ohmer, J.; Hachgenei, J.; Merzweiler, K. New Transition Metal Clusters with Ligands from Main Groups Five and Six. *Angew. Chem. Int. Ed. Engl.* **1988**, *27*, 1277–1296.

(19) Brennan, J. G.; Siegrist, T.; Stuczynski, S. M.; Steigerwald, M. L. The Transition from Molecules to Solids: Molecular Syntheses of $Ni_9Te_6(PEt_3)_8$, $Ni_{20}Te_{18}(PEt_3)_{12}$ and NiTe. *J. Am. Chem. Soc.* **1989**, *111*, 9240–9241.

(20)Steigerwald, M. L.; Siegrist, T.; Stuczynski, S. M. Octatelluridohexakis(Triethylphosphine)Hexacobalt and a Connection between Chevrel Clusters and the NiAs Structure. *Inorg. Chem.* **1991**, *30*, 2256–2257.

(21) Stuczynski, S. M.; Kwon, Y.-U.; Steigerwald, M. L. The Use of Phosphine Chalcogenides in the Preparation of Cobalt Chalcogenides. *J. Organomet. Chem.* **1993**, *449*, 167–172.

(22) Thiele, G.; You, Z.; Dehnen, S.; Molecular CHEVREL-like Clusters [(RhPPh$_3$)$_6$(μ_3-Se)$_8$] and [Pd$_6$(μ_3-Te)$_8$]$^{4-}$. *Inorg. Chem.*, **2015**, *54*, 2491–2493.

(23) Batail, P.; Livage, C.; Parkin, S. S. P.; Coulon, C.; Martin, J. D.; Canadell, E. Antiperovskite Structure with Ternary Tetrathiafulvalenium Salts: Construction, Distortion, and Antiferromagnetic Ordering. *Angew. Chem. Int. Ed.* **1991**, *30*, 1498–1500.

(24) Baudron, S. A.; Batail, P.; Coulon, C.; Clérac, R.; Canadell, E.; Laukhin, V.; Melzi, R.; Wzietek, P.; Jérome, D.; Auban-Senzier, P.; Ravy, S. (EDT-TTF-CONH$_2$)$_6$[Re$_6$Se$_8$(CN)$_6$], a Metallic Kagome-Type Organic−Inorganic Hybrid Compound: Electronic Instability, Molecular Motion, and Charge Localization. *J. Am. Chem. Soc.* **2005**, *127*, 11785–11797.

(25) Yoon, B.; Luedtke, W. D.; Barnett, R. N.; Gao, J.; Desireddy, A.; Conn, B. E.; Bigioni, T.; Landman, U. Hydrogen-Bonded Structure and Mechanical Chiral Response of a Silver Nanoparticle Superlattice. *Nat. Mater.* **2014**, *13*, 807–811.

(26) Corrigan, J. F.; Fuhr, O.; Fenske, D. Metal Chalcogenide Clusters on the Border between Molecules and Materials. *Adv. Mater.* **2009**, *21*, 1867–1871.

(27) Roy, X.; Schenck, C. L.; Ahn, S.; Lalancette, R. A.; Venkataraman, L.; Nuckolls, C.; Steigerwald, M. L. Quantum Soldering of Individual Quantum Dots. *Angew. Chem. Int. Ed.* **2012**, *51*, 12473–12476.

(28) Roy, X.; Lee, C.-H.; Crowther, A. C.; Schenck, C. L.; Besara, T.; Lalancette, R. A.; Siegrist, T.; Stephens, P. W.; Brus, L. E.; Kim, P.; Steigerwald, M. L.; Nuckolls, C. Nanoscale Atoms in Solid-State Chemistry. *Science* **2013**, *341*, 157–160.

(29) Lee, C.-H.; Liu, L.; Bejger, C.; Turkiewicz, A.; Goko, T.; Arguello, C. J.; Frandsen, B. A.; Cheung, S. C.; Medina, T.; Munsie, T. J. S.; D'Ortenzio, R.; Luke, G. M.; Besara, T.; Lalancette, R. A.; Siegrist, T.; Stephens, P. W.; Crowther, A. C.; Brus, L. E.; Matsuo, Y.; Nakamura, E.; Uemura, Y. J.; Kim, P.; Nuckolls, C.; Steigerwald, M. L.; Roy, X. Ferromagnetic Ordering in Superatomic Solids. *J. Am. Chem. Soc.* **2014**, *136*, 16926–16931.

(30) Turkiewicz, A.; Paley, D. W.; Besara, T.; Elbaz, G.; Pinkard, A.; Siegrist, T.; Roy, X. Assembling Hierarchical Cluster Solids with Atomic Precision. *J. Am. Chem. Soc.* **2014**, *136*, 15873–15876.

(31) Choi, B.; Paley, D. W.; Siegrist, T.; Steigerwald, M. L.; Roy, X. Ligand Control of Manganese Telluride Molecular Cluster Core Nuclearity. *Inorg. Chem.* **2015**, *54*, 8348–8355.

(32) Choi, B.; Yu, J.; Paley, D. W.; Trinh, M. T.; Paley, M. V.; Karch, J. M.; Crowther, A. C.; Lee, C.-H.; Lalancette, R. A.; Zhu, X.; Kim, P.; Steigerwald, M. L.; Nuckolls, C.; Roy, X. Van Der Waals Solids from Self-Assembled Nanoscale Building Blocks. *Nano Lett.* **2016**, *16*, 1445–1449.

(33) Champsaur, A. M.; Velian, A.; Paley, D. W.; Choi, B.; Roy, X.; Steigerwald, M. L.; Nuckolls, C. Building Diatomic and Triatomic Superatom Molecules. *Nano Lett.* **2016**, *16*, 5273–5277.

(34) Ong, W.-L.; O'Brien, E. S.; Dougherty, P. S. M.; Paley, D. W.; Fred Higgs Iii, C.; McGaughey, A. J. H.; Malen, J. A.; Roy, X. Orientational Order Controls Crystalline and Amorphous Thermal Transport in Superatomic Crystals. *Nat. Mater.* **2017**, *16*, 83–88.

(35) Trinh, M. T.; Pinkard, A.; Pun, A. B.; Sanders, S. N.; Kumarasamy, E.; Sfeir, M. Y.; Campos, L. M.; Roy, X.; Zhu, X.-Y. Distinct Properties of the Triplet Pair State from Singlet Fission. *Sci. Adv.* **2017**, *3*, e1700241.

(36) Lovat, G.; Choi, B.; Paley, D. W.; Steigerwald, M. L.; Venkataraman, L.; Roy, X. Room-Temperature Current Blockade in Atomically Defined Single-Cluster Junctions. *Nat. Nanotechnol.* **2017**, 12, 1050–1054.

(37) O'Brien, E. S.; Trinh, M. T.; Kann, R. L.; Chen, J.; Elbaz, G. A.; Masurkar, A.; Atallah, T. L.; Paley, M. V.; Patel, N.; Paley, D. W.; Kymissis, I.; Crowther, A. C.; Millis, A. J.; Reichman, D. R.; Zhu, X.-Y.; Roy, X. Single-Crystal-to-Single-Crystal Intercalation of a Low-Bandgap Superatomic Crystal. *Nat. Chem.* **2017**, *9*, 1170–1174.

(38) Voevodin, A.; Abella, L.; Castro, E.; Paley, D. W.; Campos, L. M.; Rodríguez-Fortea, A.; Poblet, J. M.; Echegoyen, L.; Roy, X. Dimerization of Endohedral Fullerene in a Superatomic Crystal. *Chem. Eur. J.* **2017**, *23*, 13305–13308.

(39) Champsaur, A. M.; Mézière, C.; Allain, M.; Paley, D. W.; Steigerwald, M. L.; Nuckolls, C.; Batail, P. Weaving Nanoscale Cloth through Electrostatic Templating. *J. Am. Chem. Soc.* **2017**, *139*, 11718–11721.

(40) Champsaur, A. M.; Yu, J.; Roy, X.; Paley, D. W.; Steigerwald, M. L.; Nuckolls, C.; Bejger, C. M. Two-Dimensional Nanosheets from Redox-Active Superatoms. *ACS Cent. Sci.* **2017**, *3*, 1050–1055.

(41) Reber, A. C.; Khanna, S. N. Superatoms: Electronic and Geometric Effects on Reactivity. *Acc. Chem. Res.* **2017**, *50*, 255–263.

(42) Chauhan, V.; Reber, A. C.; Khanna, S. N. Metal Chalcogenide Clusters with Closed Electronic Shells and the Electronic Properties of Alkalis and Halogens. *J. Am. Chem. Soc.* **2017**, *139*, 1871–1877.

(43) Chauhan, V.; Sahoo, S.; Khanna, S. N. $Ni_9Te_6(PEt_3)_8C_{60}$ Is a Superatomic Superalkali Superparamagnetic Cluster Assembled Material (S3-CAM). *J. Am. Chem. Soc.* **2016**, *138*, 1916–1921.

(44) Peña, O. Chevrel Phases: Past, Present and Future. *Phys. C Supercond. Its Appl.* **2015**, *514* (Supplement C), 95–112.

(45) Cecconi, F.; Ghilardi, C. A.; Midolllini, S.; Zanello, A. O. P. Synthesis, Properties and Structures of the Two "Electron Rich" Cobalt-Sulphur Clusters $[Co_6(\mu_3\text{-}S)_8(PEt_3)6]^{1+,0}$.

(46) Seino, H.; Hidai, M. Catalytic Functions of Cubane-Type M_4S_4 Clusters. *Chem. Sci.* **2011**, *2*, 847–857.

(47) Baran, P.; Boča, R.; Chakraborty, I.; Giapintzakis, J.; Herchel, R.; Huang, Q.; McGrady, J. E.; Raptis, R. G.; Sanakis, Y.; Simopoulos, A. Synthesis, Characterization, and Study of Octanuclear Iron-Oxo Clusters Containing a Redox-Active Fe_4O_4-Cubane Core. *Inorg. Chem.* **2008**, *47*, 645–655.

(48) Cao, X.-Y.; Hubbard, J. W.; Guerrero-Medina, J.; Hernández-Maldonado, A. J.; Mathivathanan, L.; Rinaldi, C.; Sanakis, Y.; Raptis, R. G. Spin-Glass Behavior of a Hierarchically-Organized, Hybrid Microporous Material, Based on an Extended Framework of Octanuclear Iron-Oxo Units. *Dalton Trans.* **2015**, *44*, 3399–3409.

(49) Shott, J. L.; Freeman, M. B.; Saleh, N.-A.; Jones, D. S.; Paley, D. W.; Bejger, C. Ball and Socket Assembly of Binary Superatomic Solids Containing Trinuclear Nickel Cluster Cations and Fulleride Anions. *Inorg. Chem.* **2017**, *56*, 10984–10990.

Chapter 2: Tuning the Electronic Properties of Hexanuclear Cobalt Sulfide Superatoms via Ligand Substitution

2.1: Preface

This chapter is based on a manuscript in preparation authored by Gaoxiang Liu, Andrew Pinkard, Sandra M. Ciborowski, Vikas Chauhan, Zhaoguo Zhu, Alexander Aydt, Shiv N. Khanna, Xavier Roy, and Kit H. Bowen. I synthesized the family of clusters discussed in this chapter and helped communicate the superatomic analogy of this atomic concept.

2.2: Introduction

Electron affinity and ionization energy are fundamental properties of the elements. Together they govern the interactions and bonding of close-contacting atoms and control the collective properties of solids. Because they are intrinsic to each element, however, the electron affinity and ionization energy of a given atom cannot be altered. This presents an immense synthetic challenge for the design of tunable materials as substituting atoms often leads to entirely new structures, interactions and collective behaviors.

By analogy to "atomic" building blocks, certain clusters can be used as "superatomic" building blocks for the assembly of novel materials.[1-22] Within this context, the family of metal chalcogenide molecular clusters has recently received

29

renewed attention for the creation of functional solids with tunable properties, including ferromagnetism, electrical conductivity, tunable optical gap and thermal switching[1,7, 23-32]. One of the key advantages of this approach over traditional atomic solids is that the characteristics of the building blocks could be tuned *pre-assembly* without changing the total electron count of the superatom. Using the molecular cluster $Co_6Te_8L_6$ (L = passivating ligand) as a model system, Khanna *et al.* recently predicted theoretically that changing L from PEt_3 to CO increases the electron affinity of the Co_6Te_8 core, in effect transforming the cluster from a superatomic alkali metal to superatomic halogen (33,34). Here we experimentally demonstrate this concept by directly probing the electron affinity (EA) and electronic structure of a series of cobalt sulfide clusters whose ligand shell is a combination of PEt_3 and CO using photoelectron spectroscopy. The compounds, $Co_6S_8(PEt_3)_{6-x}(CO)_x$, are synthesized from the parent cluster $Co_6S_8(PEt_3)_6$ by ligand substitution with CO, and then vaporized and ionized using a specialized infrared desorption/laser photoemission source. Mass spectrometry confirms the existence of carbonylated products with x up to 3 (i.e. $Co_6S_8(PEt_3)_5(CO)^-$, $Co_6S_8(PEt_3)_4(CO)_2^-$, and $Co_6S_8(PEt_3)_3(CO)_3^-$). We find that the measured electron affinity and vertical detachment energy increase with the number of CO ligands, demonstrating the electronic spectra tunability of this family of superatoms. These results help elucidate the superatom concept, which will prove useful in the design of materials synthesized starting from programmable building blocks.

2.3 Synthetic Strategy

Our strategy to synthesize $Co_6S_8(PEt_3)_{6-x}(CO)_x$ begins by preparing the parent compound $Co_6S_8(PEt_3)_6$ on a multigram scale. To achieve this, we have developed a new

approach detailed in the Supporting Information. Under a CO atmosphere, $Co_6S_8(PEt_3)_6$ is reacted with 6 equivalents of elementary S in toluene at ~100 °C to partially substitute CO for PEt_3, which is trapped as $S=PEt_3$. Using the mass spectrometry technique described below, we observe a mixture of clusters in which up to 3 CO ligands have been substituted for PEt_3. It is possible to separate these different species using column chromatography[35] but for this work we can use the mixture of clusters without additional purification. Details about synthesis are presented at this end of this chapter.

2.4 Ionization and Mass Detection

Measuring the electron affinity and electronic structure of $Co_6S_8(PEt_3)_{6-x}(CO)_x$ requires a photoelectron spectroscopic study on their parent anions, $Co_6S_8(PEt_3)_{6-x}(CO)_x^-$, in the gas phase. Common ionization methods (e.g. electrospray ionization and matrix-assisted laser desorption/ionization), however, these methods fail to generate the parent anions $Co_6S_8(PEt_3)_{6-x}(CO)_x^-$ in the gas phase due to the effect of solvent/matrix on neutral $Co_6S_8(PEt_3)_{6-x}(CO)_x$ clusters: the obtained anions are either dissociated or tagged by the solvent/matrix molecules. To make the parent anions in the gas phase, we instead employ a specialized infrared desorption/photoemission (IR/PE) source that combines pulsed infrared desorption to bring the neutral clusters into the gas phase, pulsed photoemission to provide electrons for attachment, and a pulsed helium jet expansion for cooling and transporting the resulting anions.[36] A typical anion mass spectrum of $Co_6S_8(PEt_3)_{6-x}(CO)_x^-$ obtained with the IR/PE source is shown in Figure 2.1. The spectrum contains two major series of anions; namely, $Co_6S_8(PEt_3)_n^-$ (n = 0–5) and $Co_6S_8(PEt_3)_{6-x}(CO)_x^-$ (x = 0–3). The $Co_6S_8(PEt_3)_n^-$ clusters are from the sequential elimination of PEt_3 from $Co_6S_8(PEt_3)_6$ during infrared desorption, while the $Co_6S_8(PEt_3)_{6-x}(CO)_x^-$ clusters are the

anions of interest. Though the $Co_6S_8(PEt_3)_{6-x}(CO)_x^-$ signals are weaker, their high cross-section with photon makes it possible for collecting their photoelectron spectra.
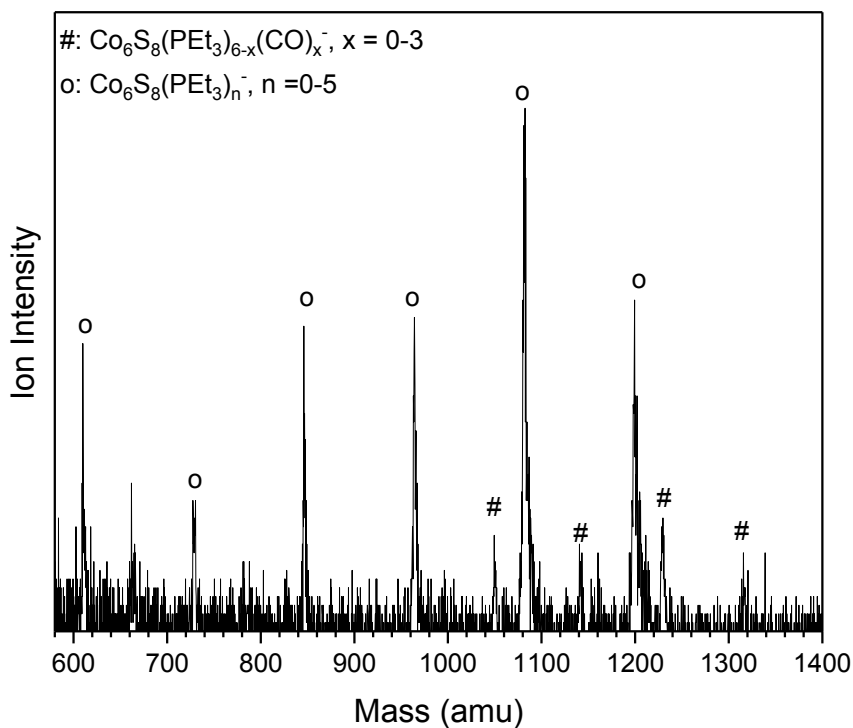
Figure 2.1. Anion mass spectrum of $Co_6S_8(PEt_3)_{6-x}(CO)_x^-$ generated using IR/PE anion source.

2.5 Ionization Energy and Electron Affinity

Figure 2.2 presents the photoelectron spectra of $Co_6S_8(PEt_3)_{6-x}(CO)_x^-$ (x = 0–3) from which the adiabatic electron affinity (AEA) and vertical detachment energy (VDE) of each cluster are determined. Note that the experimentally observed value is the adiabatic detachment energy (ADE) corresponding to the transition from the ground state of the anion to the relaxed configuration of its neutral counterpart, which is experimentally determined as the onset of the first peak in the photoelectron spectrum. When there is sufficient Franck-Condon overlap between the ground vibrational states of

32

anion and neutral species, ADE is equivalent to AEA in value. Since we are interested in the electron affinity of the superatoms, AEA is used throughout the discussion. The VDE is the vertical transition from the anion to the neutral state at the anion's geometry; it is determined as the electron binding energy value at which the first peak is at its maximum. Due to its higher intensity, VDE can be accurately determined by experiment and thus provide benchmark for theoretical calculations. From the spectra, the AEA of $Co_6S_8(PEt_3)_{6-x}(CO)_x$ are determined as 1.1, 1.3, 1.7 and 1.8 eV for x = 0, 1, 2, 3, respectively; while their anions' VDE are 1.30, 1.51, 1.95 and 2.09 eV, respectively. Therefore, by sequentially substituting half of the PEt_3 with CO, the AEA of this superatom is increased from 1.1 eV, which is close to the reducing agent SO_2 (1.11 eV), to 1.8 eV, which is close to the oxidizing agent SO_3 (1.90 eV). Noticeably, the AEA change in the superatom does not involve changing the oxidation state of the Co_6S_8 core, while for sulfur oxides the oxidation state change on S atom accounts for the leap in its AEA. The unambiguous trend of increasing AEA and VDE is a direct evidence that the electronic properties of this superatom can be tuned by ligand substitution.
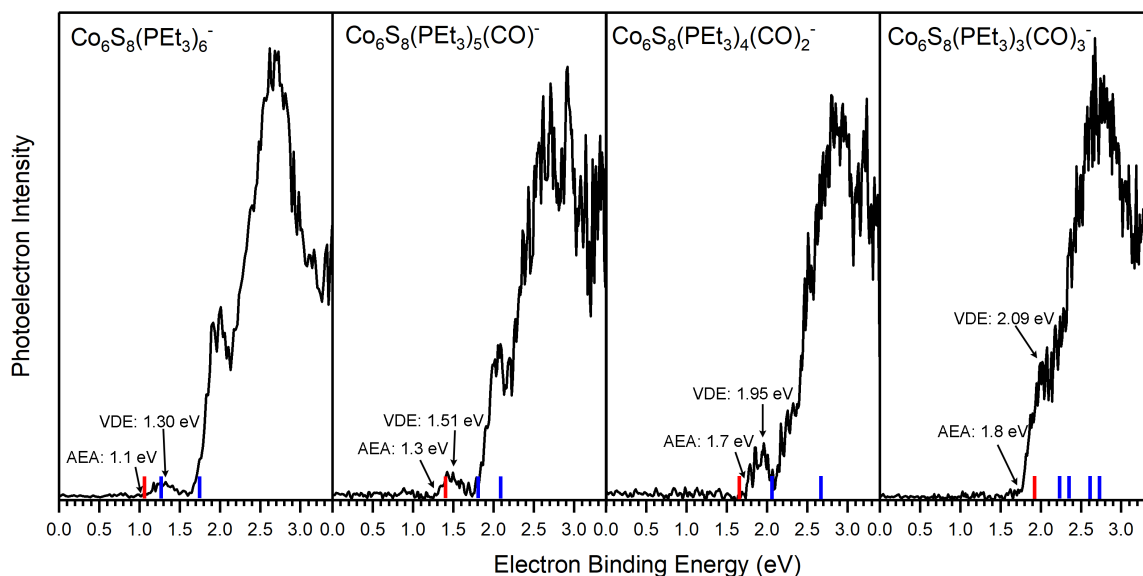
Figure 2.2. Photoelectron spectra of $Co_6S_8(PEt_3)_{6-x}(CO)_x^-$ (x = 0–3) collected using 355 nm (3.49 eV) Nd:YAG laser. The arrows point to the experimental values of AEA and VDE; the red lines correspond to theoretical AEA, and the blue lines correspond to vertical transitions from the anion to the singlet and triplet neutral states.

The tuning of the electronic properties can be further demonstrated by the spectral features at higher electron binding energy than the first peak, which arise from transitions from the anion ground state to various electronic excited states of the neutral cluster. The shape of these features relates to the absorption spectrum and reflects the electronic structure of the neutral clusters. While the photoelectron spectra of $Co_6S_8(PEt_3)_{6-x}(CO)_x^-$ shift to higher electron binding energy as x increases, their overall shapes are remarkably similar, confirming that the sequential exchange of PEt$_3$ with CO ligand leaves the electronic structure of $Co_6S_8(PEt_3)_{6-x}(CO)_x$ largely unchanged, but monotonically shifted to deeper energies.

^{2}Co$_6$S$_8$(PEt$_3$)$_6^-$
VDE^1 =1.28 eV
AEA = 1.06 eV

^{2}Co$_6$S$_8$(PEt$_3$)$_5$(CO)$^-$
VDE^1 =1.80 eV
AEA =1.40 eV

^{2}*trans*-Co$_6$S$_8$(PEt$_3$)$_4$(CO)$_2^-$
VDE^1 =1.62 eV
AEA =1.38 eV

^{2}*cis*-Co$_6$S$_8$(PEt$_3$)$_4$(CO)$_2^-$
VDE^1 =2.06 eV
AEA =1.65 eV

^{2}*mer*-Co$_6$S$_8$(PEt$_3$)$_3$(CO)$_3^-$
VDE^1 =2.22 eV
AEA =1.92 eV

^{2}*fac*-Co$_6$S$_8$(PEt$_3$)$_3$(CO)$_3^-$
VDE^1 =2.35 eV
AEA =1.93 eV
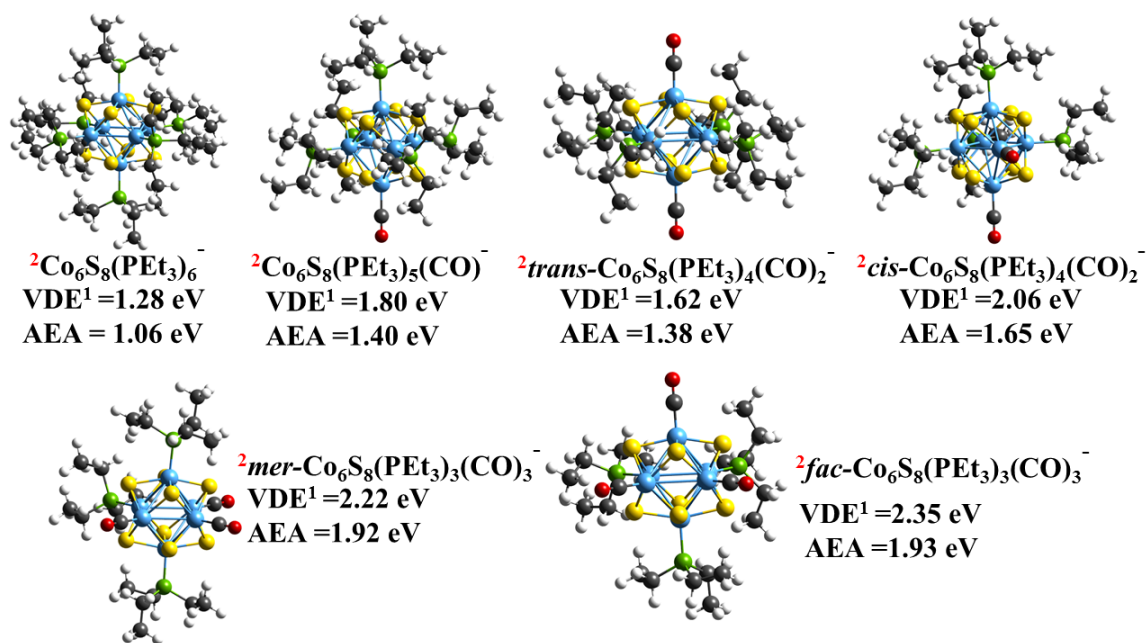
Figure 2.3. Optimized ground state structure of anionic Co$_6$S$_8$(PEt$_3$)$_{6-x}$(CO)$_x^-$ (x = 0–3) clusters. The red superscript indicates the spin multiplicity (2S+1) of each cluster.

Figure 2.3 shows the computed ground state structures of Co$_6$S$_8$(PEt$_3$)$_{6-x}$(CO)$_x^-$ along with VDE and AEA. In agreement with previous calculations of the Co$_6$Te$_8$(PEt$_3$)$_{6-x}$(CO)$_x$ system,[7] we find that the anionic clusters Co$_6$S$_8$(PEt$_3$)$_{6-x}$(CO)$_x^-$ have doublet spin ground state while the neutral species have singlet spin state. For Co$_6$S$_8$(PEt$_3$)$_4$(CO)$_2^-$, there are two possible structures: *trans*-Co$_6$S$_8$(PEt$_3$)$_4$(CO)$_2^-$ and *cis*-Co$_6$S$_8$(PEt$_3$)$_4$(CO)$_2^-$, with the latter lower in energy by 0.20 eV. The replacement of three PEt$_3$ ligands with CO leads to *fac*-Co$_6$S$_8$(PEt$_3$)$_3$(CO)$_3^-$ and *mer*-Co$_6$S$_8$(PEt$_3$)$_3$(CO)$_3^-$ isomers, with the latter isomer lower in energy by 0.07 eV. The small energy difference between the isomers suggests their co-existence in the experimental beam. Table S1 contains more calculation results on neutral and anionic species.

To support the experimental observations, we model the electronic structure of the superatoms using the photoelectron spectra as fingerprints of the ground state geometry

35

and electronic state of both the neutral and anionic clusters. In this work, the theoretical ground state of the system is established with three points of comparison: AEA, VDE and VDE*. The two VDEs are the vertical transitions from the anion ground state to the neutral with singlet and triplet spin multiplicity, respectively. Experimentally, VDE and VDE* correspond to the electron binding energy of the first and second peaks in the photoelectron spectrum. Table 1 lists these values, and the calculated values of AEA, VDE and VDE* are included in Figure 2.2 as red and blue lines. Using AEA, VDE and VDE* as reference to validate the computation, we observe close agreement between experimental and calculated values. The broadening of the peak onset in the photoelectron spectra is ascribed to small changes in the ground state structure upon removal of an electron from the anion, as well as due to the presence of different isomers in the experimental beam. The key result is that the AEA and both VDEs increase as PEt_3 ligands are successively replaced with CO. Starting with $Co_6S_8(PEt_3)_6^-$, the calculated AEA, VDE and VDE* of 1.06, 1.28 and 1.74 eV are close to the experimental values of 1.10, 1.30 eV and 1.91 eV, respectively. Experimentally, the replacement of one PEt_3 with a CO ligand results in a ~0.2 eV increase of the AEA (1.30 eV) and VDEs (1.51 and 2.05 eV), and the calculated AEA (1.40 eV) and VDEs (1.80 and 2.08 eV) for $Co_6S_8(PEt_3)_5CO^-$ are only slightly higher. For cis-$Co_6S_8(PEt_3)_4(CO)_2^-$ and $trans$-$Co_6S_8(PEt_3)_4(CO)_2^-$, the computed ground states have AEA of 1.65 and 1.38 eV, VDE of 2.06 and 1.62 eV, and VDE* of 2.66 and 2.16 eV, respectively. Note that the experimental results for $Co_6S_8(PEt_3)_4(CO)_2^-$ (AEA = 1.7 eV, VDE = 1.95 eV, and VDE* = 2.51 eV) agree best with the cis-isomer calculations. For n = 3, both the mer-$Co_6S_8(PEt_3)_3(CO)_3^-$ and fac-$Co_6S_8(PEt_3)_3(CO)_3^-$ have similar computed AEA and VDEs

that are consistent with the experimental data. Because the *mer-* and *fac*-clusters are close in energy in their neutral and anionic forms, it is very likely that they both exist in the ion beam and that the $Co_6S_8(PEt_3)_3(CO)_3^-$ photoelectron spectrum is an overlap of both isomers.
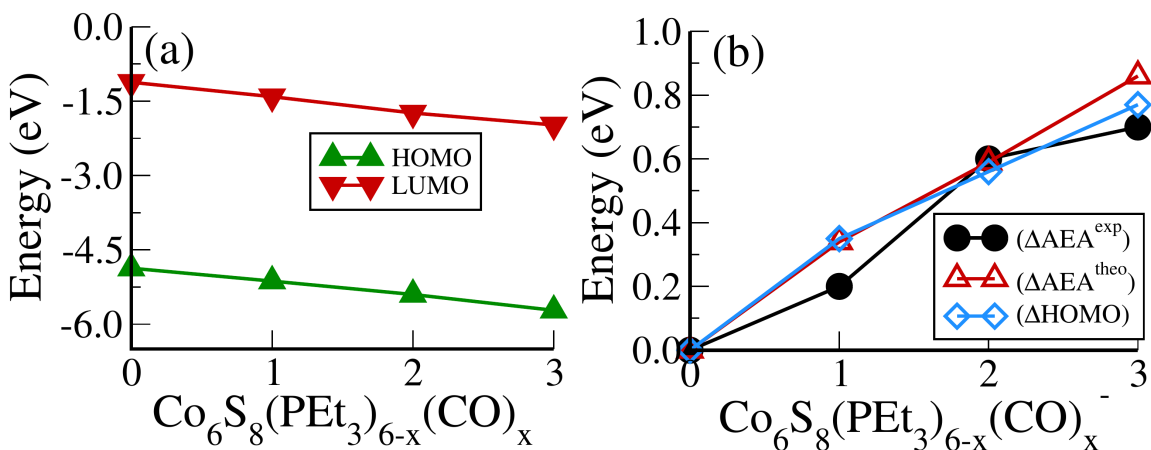
Figure 2.4. (a) The absolute energy values of the HOMO and LUMO of the neutral $Co_6S_8(PEt_3)_{6-x}(CO)_x$ (x = 1-3) clusters (b) Increment in the experimental AEA, theoretical AEA, and the LUMO of $Co_6S_8(PEt_3)_{6-x}(CO)_x$ (x = 1-3) with respect to $Co_6S_8(PEt_3)_6$. All the values are given in eV.

The replacement of PEt_3 ligands by CO concurrently lowers the energies of the highest occupied molecular orbital (HOMO) and lowest unoccupied molecular orbital (LUMO), with the result that the HOMO-LUMO gap is essentially unchanged across the cluster series. Figure 2.4 (a) illustrates this trend for the neutral species. The lowering of the HOMO and LUMO can be in part understood in terms of the vastly different ligand field effect of the cluster surface passivation: PEt_3 is a strong σ-donor that increases the electron density in the core while CO is a strong π-acceptor that removes electron density from the core, thus lowering the energy of the electronic spectrum.[7] The change in the AEA closely tracks the change in the LUMO as the electron is attached to the LUMO of the neutral. This is illustrated in Figure 2.4 (b), which shows the changes in the energy of the LUMO (ΔLUMO), theoretical AEA (ΔAEA^{Theo}) and experimental AEA (ΔAEA^{exp})

of $Co_6S_8(PEt_3)_{6-x}(CO)_x$ as x increases from 0 to 3. In addition to traditional ligand field effects, PEt_3 and CO form charge transfer complexes, and the induced dipoles at the cluster surface play a critical role in changing the electronic properties. As a reference, surface dipoles can either increase or decrease the work function of metals.[8] In this case, as PEt_3 are replaced by CO, the sign of the dipole changes and hence AEA increases as more CO are bound to the core.

Though the ionization energy of $Co_6S_8(PEt_3)_{6-x}(CO)_x$ is not measured here, the successive raise in AEA and lowering of HOMO are evident of a trend of increasing ionization energy as PEt_3 is substituted by CO.

2.6 Conclusion

Through this combined study of inorganic synthesis, gas-phase photoelectron spectroscopy, and electronic structure calculation, we demonstrate that the electronic properties of metal chalcogenide superatomic clusters can be tuned by substituting the capping ligands without involving changing the total electron count. We hope that the present study can shed light on designing novel functional materials with superatomic building blocks.

2.7 Synthetic Details

Unless otherwise stated, all reactions and sample preparations were carried out under inert atmosphere using standard Schlenk techniques or in a nitrogen-filled glovebox. The preparation of $Co_6S_8(PEt_3)_6$ has been previously described, but was instead prepared using the method detailed below.

$Co_6S_8(PEt_3)_6$. In a 200 mL Schlenk flask, elemental sulfur (1.16 g, 0.0362 mol, 3 eq) was suspended and stirred in approximately 30 mL of toluene. In two separate flasks,

$Co_2(CO)_8$ (4.12 g, 0.0120 mol, 1 eq) and triethylphosphine (4.27 g, 0.0351 mol, 3 eq) was dissolved in approximately 20 mL of toluene. The solution of $Co_2(CO)_8$ was added to the suspension of elemental sulfur followed by quick addition of the triethylphosphine solution the reaction mixture. The reaction mixture was then refluxed under nitrogen for 2 days. (NOTE: this reaction can be monitored by IR spectroscopy by taking small aliquots from the reaction mixture, removing the solvent, and checking the solid for the disappearance of the CO stretches.) Next, the reaction mixture was cooled to 100 °C, opened to air, and hot filtered through a bed of Celite. The filtrate was cooled to room temperature and left to stand for approximately 3 hours. This suspension was then filtered through a fine frit and the precipitate washed with toluene, followed by ether. The dark, black crystals were then collected, dried under vacuum, and stored under nitrogen. Yield: 2.2 g (42%). MS-MALDI m/z+ calculated 1317.9220; found, 1317.9467.

$Co_6S_8(PEt_3)_{6-x}(CO)_x$. In a 200 mL Schlenk flask, $Co_6S_8(PEt_3)_6$ (1.00 g, 0.758 mmol, 1 eq) and elemental sulfur (0.146 g, 4.55 mmol, 6 eq) were suspended in toluene. An external bubbler was attached to the system, and the mixture was then sparged with CO gas for 30 minutes and left under a gentle stream of CO for the duration of the reaction. The mixture was heated to 100 °C and stirred under a CO atmosphere for 16 h. The reaction mixture was cooled to room temperature, sparged with N2, and the volatiles removed under vacuum. The resulting mixture was directly used without further purification.

39

2.8 References

(1)   Pinkard, A.; Champsaur, A. M.; Roy, X. Molecular Clusters: Nanoscale Building Blocks for Solid-State Materials. *Acc. Chem. Res.* **2018**, *51*, 919-929.

(2)   Claridge, S. A.; Castleman, A. W.; Khanna, S. N.; Murray, C. B.; Sen, A.; Weiss, P. S. Cluster-Assembled Materials. ACS Nano. **2009**, *3*, 244−255

(3)   Tulsky, E. G.; Long, J. R. Dimensional Reduction: A Practical Formalism for Manipulating Solid Structures. *Chem. Mater*. **2001**, *13*, 1149−1166

(4)   Baudron, S. A.; Batail, P.; Coulon, C.; Clerac, R.; Canadell, E.;́ Laukhin, V.; Melzi, R.; Wzietek, P.; Jerome, D.; Auban-Senzier, P.;́ Ravy, S. (EDT-TTF-CONH$_2$)$_6$[Re$_6$Se$_8$(CN)$_6$], a Metallic KagomeType Organic−Inorganic Hybrid Compound: Electronic Instability, Molecular Motion, and Charge Localization. *J. Am. Chem. Soc.* **2005**, *127*, 11785−11797

(5)   Yoon, B.; Luedtke, W. D.; Barnett, R. N.; Gao, J.; Desireddy, A.; Conn, B. E.; Bigioni, T.; Landman, U. Hydrogen-Bonded Structure and Mechanical Chiral Response of a Silver Nanoparticle Superlattice. *Nat. Mater*. **2014**, *13*, 807−811.

(6)   Corrigan, J. F.; Fuhr, O.; Fenske, D. Metal Chalcogenide Clusters on the Border between Molecules and Materials. *Adv. Mater*. **2009**, *21*, 1867−1871.

(7)   Roy, X.; Lee, C.-H.; Crowther, A. C.; Schenck, C. L.; Besara, T.; Lalancette, R. A.; Siegrist, T.; Stephens, P. W.; Brus, L. E.; Kim, P.; Steigerwald, M. L.; Nuckolls, C. Nanoscale Atoms in Solid-State Chemistry. *Science* **2013**, *341*, 157−160.

(8)   Khanna, S. N.; Jena, P. Atomic Clusters: Building Blocks for a Class of Solids. *Phys. Rev. B*. **1995**, *51*, 13705- 13716.

(9)   Castleman, A. W.; Khanna, S. N. Clusters, Superatoms, and Building Blocks of New Materials. *J. Phys. Chem. C*, **2009**, *113*, 2664–2675.

(10)   Reber, A. C.; Khanna, S. N. Superatoms: Electronic and Geometric Effects on Reactivity. *Acc. Chem. Res.*, **2017**, *50*, 255–263.

(11)   Lee, C.-H.; Liu, L.; Bejger, C.; Turkiewicz, A.; Goko, T.; Arguello, C. J.; Frandsen, B. A.; Cheung, S. C.; Medina, T.; Munsie, T. J. S.; D'Ortenzio, R.; Luke, G. M.; Besara, T.; Lalancette, R. A.; Siegrist, T.; Stephens, P. W.; Crowther, A. C.; Brus, L. E.; Matsuo, Y.; Nakamura, E.; Uemura, Y. J.; Kim, P.; Nuckolls, C.; Steigerwald, M. L.; Roy, X. Ferromagnetic Ordering in Superatomic Solids. *J. Am. Chem. Soc*. **2014**, *136*, 16926−16931.

(12)   Roy, X.; Schenck, C. L.; Ahn, S.; Lalancette, R. A.; Venkataraman, L.; Nuckolls, C.; Steigerwald, M. L. Quantum Soldering of Individual Quantum Dots. *Angew. Chem., Int. Ed*. **2012**, *51*, 12473−12476.

(13)   Trinh, M. T.; Pinkard, A.; Pun, A. B.; Sanders, S. N.; Kumarasamy, E.; Sfeir, M. Y.; Campos, L. M.; Roy, X.; Zhu, X.-Y. Distinct Properties of the Triplet Pair State from Singlet Fission. *Sci. Adv*. **2017**, *3*, e1700241

(14)   Chauhan, V.; Sahoo, S.; Khanna, S. N. $Ni_9Te_6(PEt_3)_8C_{60}$ Is a Superatomic Superalkali Superparamagnetic Cluster Assembled Material (S3-CAM). *J. Am. Chem. Soc*. **2016**, *138*, 1916−1921.

(15)   Khanna, S. N.; Reber, A. C. Superatomic Solids: Intercalation Without Altercation. *Nat. Chem*. **2017**, *9*, 1151–1152.

(16)   Tomalia, D. A.; Khanna, S. N. A Systematic Framework and Nanoperiodic Concept for Unifying Nanoscience: Hard/Soft Nanoelements, Superatoms, Meta-

Atoms, New Emerging Properties, Periodic Property Patterns, and Predictive Mendeleev-like Nanoperiodic Tables. *Chem. Rev.* **116**, 2705–2774 (2016).

(17)   Zheng, Z., Long, J. R. & Holm, R. H. A basis set of Re_6Se_8 cluster building blocks and demonstration of their linking capability: directed synthesis of an $Re_{12}Se_{16}$ dicluster. *J. Am. Chem. Soc.* **119**, 2163–2171 (1997).

(18)   Cargnello, M.; Johnston-Peck, A. C.; Diroll, B. T.; Wong, E.; Datta, B.; Damodhar, D.; Doan-Nguyen, V. V. T.; Herzing, A. A.; Kagan, C. R.; Murray, C. B. Substitutional Doping in Nanocrystal Superlattices. *Nature.* **2015**, *524*, 450–453.

(19)   O'Brien, M. N., Jones, M. R., Lee, B. & Mirkin, C. A. Anisotropic Nanoparticle Complementarity in DNA-mediated Co-Crystallization. *Nat. Mater.* **2015**, *14*, 833–839.

(20)   Yoon, B.; Luedtke, W. D.; Barnett, R. N.; Gao, J.; Desireddy, A.; Conn, B. E.; Bigioni, T.; Landman, U. Hydrogen-Bonded Structure and Mechanical Chiral Response of a Silver Nanoparticle Superlattice. *Nat. Mater.* **2014**, *13*, 807–811.

(21)   Poyser, C. L.; Czerniuk, T.; Akimov, A.; Diroll, B. T.; Gaudling, E. A.; Salasyuk, A. S.; Kent, A. J.; Yakovlev, D. R.; Bayer, M.; Murray, C. B. Coherent Acoustic Phonons in Colloidal Semiconductor Nanocrystal Superlattices. *ACS Nano.* **2016**, *10*, 1163–1169.

(22)   Ong, W.-L.; Rupich, S. M.; Talapin, D. V.; McGaughey, A. J. H.; Malen, J. A. Surface Chemistry Mediates Thermal Transport in Three-Dimensional Nanocrystal Arrays. *Nat. Mater.* **2013**, *12*, 410–415.

(23)   Voevodin, A.; Campos, L. M.; Roy, X. Multifunctional Vesicles from a Self-
         Assembled Cluster-Containing Diblock Copolymer. *J. Am. Chem. Soc.* **2018**, *140*,
         5607–5611.

(24)   Champsaur, A. M.; Yu, J.; Roy, X.; Paley, D. W.; Steigerwald, M. L.; Nuckolls,
         C.; Bejger, C. M. Two-Dimensional Nanosheets from Redox-Active Superatoms.
         ACS Cent. Sci. **2017**, *3*, 1050–1055.

(25)   Champsaur, A. M.; Mézière, C.; Allain, M.; Paley, D. W.; Steigerwald, M. L.;
         Nuckolls, C.; Batail, P. Weaving Nanoscale Cloth through Electrostatic
         Templating. *J. Am. Chem. Soc.* **2017**, *139*, 11718–11721.

(26)   O'Brien, E. S.; Trinh, M. T.; Kann, R. L.; Chen, J.; Elbaz, G. A.; Masurkar, A.;
         Atallah, T. L.; Paley, M. V.; Patel, N.; Paley, D. W.; Kymissis, I.; Crowther, A.
         C.; Millis, A. J.; Reichman, D. R.; Zhu, X.-Y.; Roy, X. Single-Crystal-to-Single-
         Crystal Intercalation of a Low-Bandgap Superatomic Crystal. *Nat. Chem.* **2017**, *9*,
         1170–1174.

(27)   Lovat, G.; Choi, B.; Paley, D. W.; Steigerwald, M. L.; Venkataraman, L.; Roy, X.
         Room-Temperature Current Blockade in Atomically Defined Single-Cluster
         Junctions. *Nat. Nanotechnol.* **2017**, 12, 1050–1054.

(28)   Ong, W.-L.; O'Brien, E. S.; Dougherty, P. S. M.; Paley, D. W.; Fred Higgs Iii, C.;
         McGaughey, A. J. H.; Malen, J. A.; Roy, X. Orientational Order Controls
         Crystalline and Amorphous Thermal Transport in Superatomic Crystals. *Nat.
         Mater.* **2017**, *16*, 83–88.

(29)   van der Waals Solids from Self-Assembled Nanoscale Building Blocks. Nano
         Lett., 2016, 16 (2), pp 1445–1449

(30) Champsaur, A. M.; Velian, A.; Paley, D. W.; Choi, B.; Roy, X.; Steigerwald, M. L.; Nuckolls, C. Building Diatomic and Triatomic Superatom Molecules. *Nano Lett.* **2016**, *16*, 5273–5277.

(31) Turkiewicz, A.; Paley, D. W.; Besara, T.; Elbaz, G.; Pinkard, A.; Siegrist, T.; Roy, X. Assembling Hierarchical Cluster Solids with Atomic Precision. *J. Am. Chem. Soc.* **2014**, *136*, 15873–15876.

(32) Yu, J.; Lee, C. H.; Bouilly, D.; Han, M.; Kim, P.; Steigerwald, M. L.; Roy, X.; Nuckolls, C. Patterning Superatom Dopants on Transition Metal Dichalcogenides. *Nano Lett.* **2016**, *16*, 3385-3389.

(33) Chauhan, V.; Reber, A. C.; Khanna, S. N. Metal Chalcogenide Clusters with Closed Electronic Shells and the Electronic Properties of Alkalis and Halogens. *J. Am. Chem. Soc.* **2017**, *139*, 1871–1877.

(34) Strong Effect of Organic Ligands on the Electronic Structure of Metal-Chalcogenide Clusters. J. Phys. Chem. A, 2018, 122 (28), pp 6014–6020

(35) Grubisic, A.; Wang, H.; Li, X.; Ko, Y. J.; Kocak, S.; Pederson, M. R.; Bowen, K. H.; Eichhorn, B. W. Photoelectron Spectroscopic and Computational Studies of the Pt@Pb$_{10}^{1-}$ and Pt@Pb$_{12}^{1-/2-}$. *PNAS.* **2011**, *108*, 14757-14762.

Chapter 3: Assembling Hierarchical Superatomic Crystals via Charge Transfer

3.1: Preface

This chapter is based on a journal article published in the *Journal of the American Chemical Society* entitled "Assembling Hierarchical Cluster Solids with Atomic Precision" by Ari Turkiewicz, Daniel W. Paley, Tiglet Besara, Giselle Elbaz, Andrew Pinkard, Theo Siegrist, and Xavier Roy. In tandem with Ari Turkiewicz, I synthesized several of the compounds studied in this project, as well as performing CV measurements. Dr. Tiglet Besara and Dr. Giselle Elbaz assisted with characterization of the synthesized compounds, while x-ray crystallography and structural analysis was performed by Dr. Dan Paley.

3.2: Introduction

In Chapter 1, SAC prepared via charge transfer of compatible superatoms was described. Here a family of binary solid-state compounds is described in more detail in which the fundamental building blocks were independently prepared, electronically and structurally complementary inorganic molecular clusters. Charge transfer between cobalt chalcogenide and iron oxide clusters generates atomically-defined hierarchical assemblies[1] in which the inter-cluster electrostatic attractions form the binary superlattice. We demonstrate various levels of control over the structure of the material: i) we modify the composition of the clusters while retaining the same cluster arrangement; ii) we change the orientation of the cluster building blocks while retaining

the same cluster superstructure; and iii) we force the superstructure to adopt an entirely different configuration that has polar symmetry.

Non-molecular compounds with identifiable cluster subunits (e.g., Chevrel and Zintl phases) can display remarkable materials properties[2-5] but their solid-state syntheses from elemental or polyatomic precursors inhibit the rational tuning of their structure and properties. Assembling solid-state materials from preformed and intact nanoscale building blocks with well-controlled and tunable properties offers significant benefits over traditional solid-state reactions and is expected to lead to the realization of materials by design.[6] Each type of building block, however, comes with its own set of benefits and limitations. For instance, nanocrystals have been assembled into remarkable superlattices but these materials intrinsically lack atomic precision.[7,8] Molecular clusters with discrete, atomically-defined structures can exhibit superatom-like collective properties[9,10] and offer rich chemistry.[12] Single-cluster-component functional materials have been prepared12-17 but the creation of crystallographically precise solids combining two or more cluster building units remains a challenge.[18,19]

3.3: Synthetic Strategy

The strategy for creating hierarchical binary assemblies of clusters was to use charge transfer and subsequent inter-cluster electrostatic attraction as a driving force for co-assembly and crystallization. We designed, synthesized and combined pairs of complementary building blocks in which one cluster is electron-donating and the other is electron-accepting.[20-22] Each superatom is comprised of a redox-active core encapsulated in a protective redox-inert shell of ligands. These building blocks are shown in Figure 3.1 with their respective energy levels as measured by cyclic voltammetry (CV). The

46

octahedral clusters $Co_6Se_8(PEt_3)_6$, $Co_6Te_8(PEt_3)_6$, $Co_6Te_8(P^nPr_3)_6$ and $Co_6Te_8(PEt_2Ph)_6$ are electron-rich and can reversibly donate up to five electrons (the first four are shown in Figure 3.1). Conversely, the cubane clusters $Fe_8O_4pz_{12}Cl4$ and $Fe_8O_4pz_{12}Br_4$ (pz = pyrazolide) are excellent electron acceptors and can reversibly take up to four electrons. Being electrically neutral, these donor and acceptor clusters are soluble in non-polar solvents such as toluene and benzene. Synthetic details are presented in section 3.5.
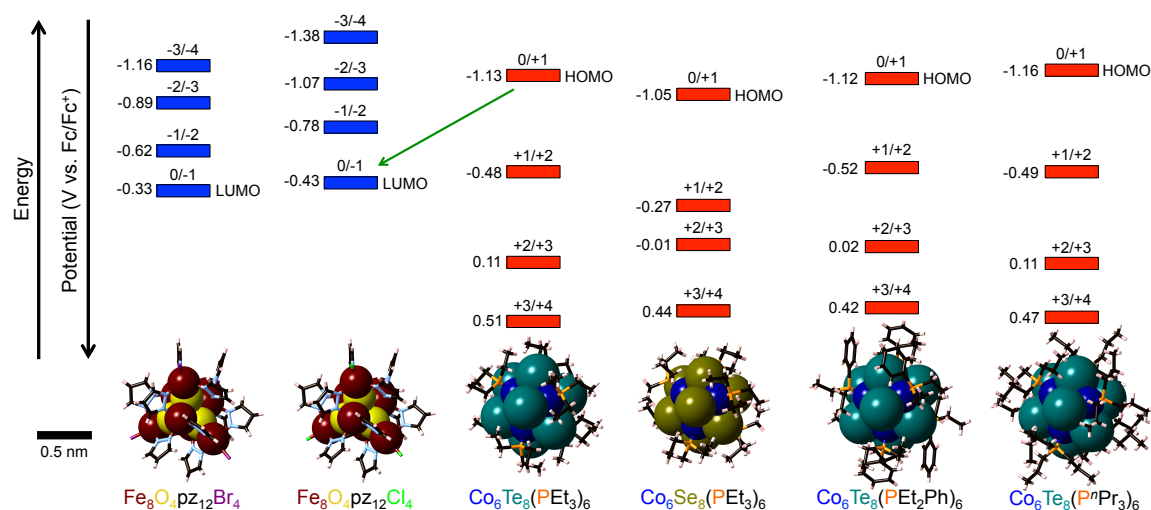
Figure 3.1. Molecular structure and redox potentials of the cluster building blocks as determined by SCXRD and CV. The clusters are depicted on the same size scale.

The respective redox potentials of $Co_6Te_8(PEt_3)_6$ and $Fe_8O_4pz_{12}Cl4$ indicate that the clusters undergo one-electron transfer in solution, although it is understood that the binary ionic lattice formation and symmetry will also govern the crystal lattice energy. $Co_6Te_8(PEt_3)_6$ and $Fe_8O_4pz_{12}Cl4$ are combined in toluene, and after approximately 12 hours, millimeter-sized black crystals are obtained that are insoluble in non-polar solvents but very soluble in polar organic solvents such as dichloromethane and tetrahydrofuran. The solubility of these crystals is consistent with the formation of an ionic compound.

3.3: Structural Analysis
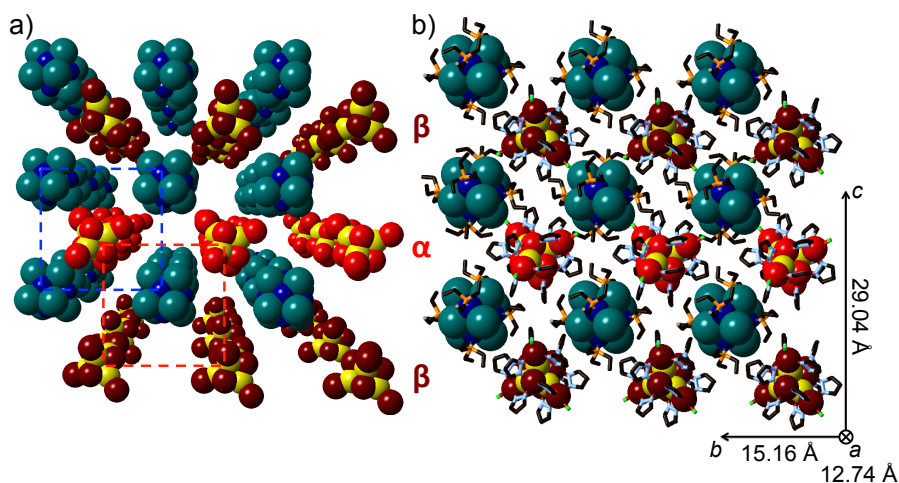
Figure 3.2. Crystal structure of $[Co_6Te_8(PEt_3)_6][Fe_8O_4pz_{12}Cl_4]$ showing the crystal packing looking down the a-axis. a) Perspective view with the capping ligands removed. b) View displaying the position of the ligands. Fe, dark and light red; O, yellow; Co, dark blue; Te, teal; P, orange; N, light blue; Cl, green; C, black. Hydrogen atoms were omitted to clarify the views.

Single crystal x-ray diffraction (SCXRD) established that the resulting solid is a crystalline 1:1 binary combination of the clusters (Figure 3.2), and the internal structures of the constituent clusters remain unchanged in the new solid-state compound. The overall packing of $[Co_6Te_8(PEt_3)_6][Fe_8O_4pz_{12}Cl_4]$ can be approximated to a primitive cubic lattice with a two-cluster basis that is the superatomic analogue of the CsCl lattice type.[23] The atomic resolution of SCXRD allows discernable, subtle crystallographic variations in the orientation of superatoms, which lower the symmetry of the crystal. While $Co_6Te_8(PEt_3)_6$ superatom adopts a single orientation, the triclinic unit cell contains two $Fe_8O_4pz_{12}Cl_4$ units related by an inversion center (clusters α and β shown in bright red and dark red in Figure 3.2). Thus, $Fe_8O_4pz_{12}Cl_4$ layers are alternating along the c-axis between two inversion-center related orientations. The centroid-to-centroid distance between two complementary adjacent clusters ranges from 11.81 to 12.75 Å.

48

3.3: Tuning SACs via Superatom Ligand Shell Modifications

Simple cubic superlattices are also obtained when donor and acceptor clusters with similar sizes, core structures and redox properties as to those of $Co_6Te_8(PEt_3)_6$ and $Fe_8O_4pz_{12}Cl_4$ are combined. The structures of the solid-state compounds $[Co_6Se_8(PEt_3)_6][Fe_8O_4pz_{12}Cl_4]$, $[Co_6Te_8(PEt_2Ph)_6][Fe_8O_4pz_{12}Cl_4]$, and $[Co_6Te_8(PEt_3)_6]$ $[Fe_8O_4pz_{12}Br_4]$ all approximate the CsCl packing but the crystallographic details of each solid differ. While the compounds $[Co_6Se_8(PEt_3)_6][Fe_8O_4pz_{12}Cl_4]$ and $[Co_6Te_8(PEt_3)_6]$ $[Fe_8O_4pz_{12}Br_4]$ adopt the same triclinic unit cell as $[Co_6Te_8(PEt_3)_6][Fe_8O_4pz_{12}Cl_4]$ with slightly different lattice parameters, the structure of $[Co_6Te_8(PEt_2Ph)_6][Fe_8O_4pz_{12}Cl_4]$ is more complex. The substitution of a rigid phenyl group on the phosphine capping ligands forces each building unit to adopt four different orientations in the monoclinic unit cell (Figure 3.3a).
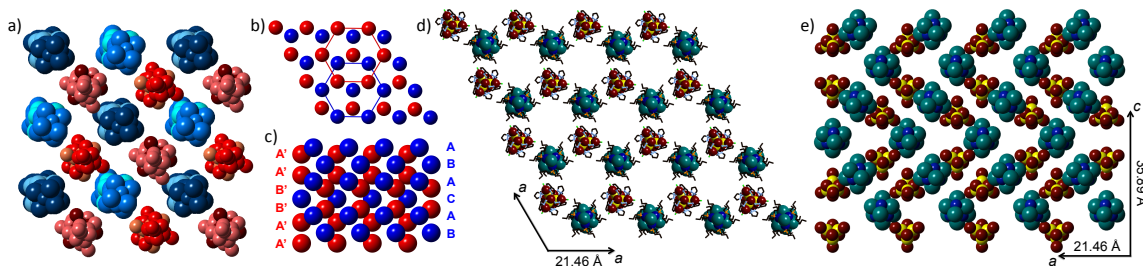
Figure 3.3. a) Crystal structure of $[Co_6Te_8(PEt_2Ph)_6][Fe_8O_4pz_{12}Cl_4]$ showing the various orientations of the superatomic cation and anion as different shades of blue and red, respectively. b) and c) Schematic views of the crystal packing of $[Co_6Te_8(P^nPr_3)_6][Fe_8O_4pz_{12}Cl_4]$. Cations are blue and anions are red. d) and e) Crystal structure of $[Co_6Te_8(P^nPr_3)_6][Fe_8O_4pz_{12}Cl_4]$. b) and d) Views of a single hexagonal layer looking down the c-axis. c) and e) Stacking sequence of the hexagonal layers along the c-axis. Capping ligands were removed in a) and e) to clarify the views. Colors as previously defined. Hydrogen atoms were omitted to clarify the views

The cluster $Co_6Te_8(P^nPr_3)_6$ has the same redox-active Co_6Te_8 core but the Co ions are capped with bulkier phosphines. Reaction of this larger donor superatom with the acceptor $Fe_8O_4pz_{12}Cl_4$ gives large hexagonal black plates that are 1:1 combinations of $Co_6Te_8(P^nPr_3)_6$ and $Fe_8O_4pz_{12}Cl_4$ as measured by SCXRD (Figure 3.3b-e). In this crystal,

the two clusters form alternating hexagonal close-packed layers with an unusual sequence of stacking along the c-axis. The cluster $Co_6Te_8(P^nPr_3)_6$ adopts an ABACA (hc) double hexagonal close-packed arrangement and the cluster $Fe_8O_4pz_{12}Cl_4$ follows the sequence A'A'B'B'A'A'. The combined stacking sequence is thus AB'BB'AA'CA' (hccc). The lattice parameter within each hexagonal layer is 21.46 Å and the shortest centroid-to-centroid distance between two neighboring complementary clusters is 12.86 Å. It noteworthy that this compound belongs to one of only ten pyroelectric[24] (or polar) point groups, C3v (or 3m), a structure that can be controlled simply by tuning the size (but not the relative electronics) of the phosphine ligand.

3.4: Charge Transfer and Electrostatic Interactions

To understand the formation of these binary compounds, a combination of CV, electronic absorption spectroscopy and crystallography. CV data suggests that the cobalt chalcogenide clusters transfer one electron to $Fe_8O_4pz_{12}Cl_4$ (see Figure 3.1). We verified that the binary hierarchical lattice of $[Co_6Te_8(PEt_3)_6][Fe_8O_4pz_{12}Cl_4]$ forms via a one-electron transfer process by comparing its electronic absorption spectrum with that of model compounds $[CoCp_2][Fe_8O_4pz_{12}Cl_4]$ and $[CoCp_2]_2[Fe_8O_4pz_{12}Cl_4]$. The cluster $Fe_8O_4pz_{12}Cl_4$ is composed of a cubical core of four high-spin Fe^{III} metal centers bridged by four 4-oxo ligands. A one-electron reduction of $Fe_8O_4pz_{12}Cl_4$ delocalizes the transferred electron between the metal ions in the redox-active Fe_4O_4 core, giving rise to an intervalence charge transfer (IVCT) band centered around 1650 nm.[25] Electronic absorption spectroscopy reveals that the IVCT band present in the near infrared (NIR) region of the $[CoCp_2][Fe_8O_4pz_{12}Cl_4]$ spectrum is absent in that of $[CoCp_2]_2[Fe_8O_4pz_{12}Cl_4]$. The electronic absorption spectrum of

$[Co_6Te_8(PEt_3)_6][Fe_8O_4pz_{12}Cl_4]$ in dichloromethane similarly shows a weak, broad IVCT band centered around 1650 nm. This IVCT transition, characteristic of a Robin and Day class II compound[25] between the oxo-bridged Fe ions, confirms the presence of the monoanion $[Fe_8O_4pz_{12}Cl_4]^-$ in $[Co_6Te_8(PEt_3)_6][Fe_8O_4pz_{12}Cl_4]$. Furthermore, the lengthening of the Co-P and Fe-Cl bonds in the crystal structure of $[Co_6Te_8(PEt_3)_6][Fe_8O_4pz_{12}Cl_4]$ compared to the neutral clusters provides further evidence[25,26] of the presence of these superatomic ions in the solid-state.

These binary solids are assembled from superatomic ions with multiple reversible redox states. The solubility of these crystals in dichloromethane allows us to measure their redox properties using CV. Figure 3.4 shows a typical cyclic voltammogram measured for $[Co_6Te_8(P^nPr_3)_6][Fe_8O_4pz_{12}Cl_4]$. This compound exhibits eight reversible redox couples that correspond to the shuttling of nine electrons in and out of the cluster units. While these redox processes were measured in solution, similar behaviors likely exist in the SAC, and could lead to the creation of new cluster-assembled intercalation compounds.
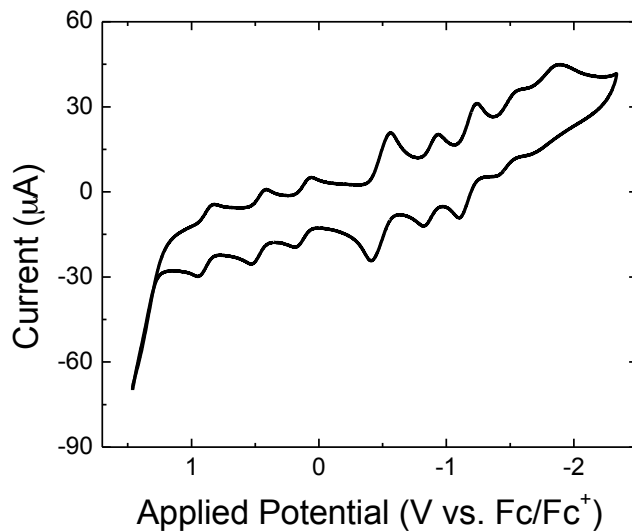
Figure 3.4. Cyclic voltammogram of $[Co_6Te_8(P^nPr_3)_6][Fe_8O_4pz_{12}Cl_4]$ (in 0.1 M $^tBu_4NPF_6$/DCM, scan rate 200 mV/s, glassy carbon working electrode, measured versus Fc/Fc$^+$).

3.4: Conclusion and Outlook

By combining molecular clusters with complementary electronic properties, binary solid-state compounds whose infinite crystalline structures are defined both on the superatomic and atomic scales have been synthesized. The packing of clusters with the same physical profile is can be modified without changes in the elements that populate the inorganic cores. By capitalizing on the synthetic variability of individual clusters, we have incorporated multiple redox-active clusters into a diverse family of solid-state materials. Subtle variation of the capping ligands on cluster cores produces significant changes in the atomic structure and the superatomic packing, such as the adoption of a configuration that has symmetry allowing pyroelectrical behavior. With a virtually limitless library of ligands available, the structures of these solid-state compounds are as versatile as one can imagine controlling cluster arrangements with great precision.

3.5: Synthetic Details

All reactions and sample preparations were carried out under an inert atmosphere using standard Schlenk techniques or in a nitrogen-filled glovebox. Dry and deoxygenated solvents were prepared by elution through a dual column (MBraun solvent purification system). Clusters $Co_6Se_8(PEt_3)_6$, $Co_6Te_8(PEt_3)_6$, $Fe_8O_4pz_{12}Cl_4$ and $Fe_8O_4pz_{12}Br_4$ were synthesized according to published protocols.[27,28]

$Co_6Te_8(P^nPr_3)_6$

Tri-*n*-propylphosphine (1.5 g, 9.36 mmol) and tellurium powder (.531 g, 4.16 mmol) were combined in 50 mL of toluene in a Schlenk flask and stirred until the solid completely dissolved. Dicobalt octacarbonyl (0.356 g, 1.04 mmol), dissolved in 10 mL toluene, was then added to this solution. The reaction mixture was refluxed for ~12 h then the hot mixture was filtered through a medium Schlenk frit. The dark reddish purple solution (similar in color to red wine) was concentrated *in vacuo* and layered with hexanes. The solution was decanted after 24 h to recover black crystals of $Co_6Te_8(P^nPr_3)_6$. The solid was washed with hexanes and diethyl ether, and dried *in vacuo*. Yield 0.372 g, 45.9%.

^{1}H NMR (400 MHz, [CDCl_3], 298 K): δ = 1.60 (36H, broad peak), 1.34 (36H, broad peak), 0.97 (54H, broad peak).

^{31}P NMR (162 MHz, [CDCl_3], 298 K): δ = 76 (broad peak).

$Co_6Te_8(PEt_2Ph)_6$

Diethylphenylphosphine (4.0 g, 24.07 mmol) and tellurium powder (1.18 g, 9.25 mmol) were combined in 15 mL of toluene in a Schlenk flask and stirred until the solid completely dissolved. Dicobalt octacarbonyl (1.13 g, 3.30 mmol), dissolved in 5 mL

toluene, was then added to the solution. The reaction was refluxed for ~12 h then the hot mixture was filtered through a medium Schlenk frit. The dark reddish purple solution was then concentrated *in vacuo* and layered with hexanes. The solution was decanted after 24 h to recover black crystals of $Co_6Te_8(PEt_2Ph)_6$. The solid was washed with hexanes and diethyl ether and dried *in vacuo*. Yield 0.650 g, 24.9 %.

^{1}H NMR (400 MHz, [CDCl3], 298 K): δ = 7.45−7.15 (30H, broad peak), 1.97 (24H, broad peak), 0.81 (36H, broad peak).

^{31}P NMR (162 MHz, [CDCl3], 298 K): δ = 72 (broad peak).

[Co₆Te₈(PEt₃)₆][Fe₈O₄pz₁₂Cl₄]

The clusters $Co_6Te_8(PEt_3)_6$ (40 mg, 19.2 μmol) and $Fe_8O_4(pz)_{12}Cl_4$ (28.13 mg, 19.2 μmol) were dissolved in 10 mL toluene in separate vials. The solutions were filtered through a 0.2 μm syringe filter and combined in a 20 mL vial. Black crystals were obtained after standing for ~24 h. The solid was collected, rinsed with toluene and hexanes, and dried *in vacuo* for ~12 h. Yield: 45.4 mg, 66.7 %.

[Co₆Te₈(PEt₃)₆][Fe₈O₄pz₁₂Br₄]

Analogous to $[Co_6Te_8(PEt_3)_6][Fe_8O_4(pz)_{12}Cl_4]$. $Co_6Te_8(PEt_3)_6$ (64 mg, 30.7 μmol), $Fe_8O_4pz_{12}Br_4$ (50 mg, 30.7 μmol). Yield: 48.2 mg, 42.3%.

[Co₆Te₈(PⁿPr₃)₆][Fe₈O₄pz₁₂Cl₄]

Analogous to $[Co_6Te_8(PEt_3)_6][Fe_8O_4(pz)_{12}Cl_4]$. $Co_6Te_8(PPr_3)_6$ (30 mg, 12.7 μmol), $Fe_8O_4pz_{12}Cl_4$ (18.7 mg, 12.7 μmol). Yield: 32.7 mg, 67.1%.

[Co₆Te₈(PEt₂Ph)₆][Fe₈O₄pz₁₂Cl₄]

Analogous to $[Co_6Te_8(PEt_3)_6][Fe_8O_4(pz)_{12}Cl_4]$. $Co_6Te_8(PEt_2Ph)_6$ (30 mg, 12.6 μmol), $Fe_8O_4pz_{12}Cl_4$ (18.57 mg, 12.6 μmol). Yield: 22.1 mg, 45.5%.

[Co₆Se₈(PEt₃)₆][Fe₈O₄pz₁₂Cl₄]

Analogous to [Co₆Te₈(PEt₃)₆][Fe₈O₄(pz)₁₂Cl₄]. Co₆Se₈(PEt₃)₆ (30 mg, 23.5 μmol), Fe₈O₄pz₁₂Cl₄ (25.8 mg, 23.5 μmol). Yield: 17.0 mg, 30.5 %.

[CoCp₂][Fe₈O₄pz₁₂Cl₄]

The cluster Fe₈O₄pz₁₂Cl₄ (20 mg, 13.6 μmol) was dissolved in 10 mL of dichloromethane in a vial. Cobaltocene (2.57 mg, 13.6 μmol), dissolved in ~2 mL of dichloromethane, was added dropwise to this solution while stirred. The mixture was stirred for an additional 30 min and then filtered through a 0.2 μm syringe filter. The filtrate was layered with hexanes. Black crystals were obtained after ~12 h. The solid was recovered, washed with toluene and hexanes, and dried *in vacuo* for ~12 h. Yield: 19.56 mg, 86.66 %.

[CoCp₂]₂[Fe₈O₄pz₁₂Cl₄]

The cluster Fe₈O₄pz₁₂Cl₄ (20 mg, 13.6 μmol) was dissolved in 10 mL of dichloromethane in a vial. Cobaltocene (5.14 mg, 27.2 μmol), dissolved in ~3 mL of dichloromethane, was added dropwise this solution while being stirred. The mixture was stirred for an additional 30 min and then filtered through a 0.2 μm syringe filter. The filtrate was layered with hexanes. Black crystals were obtained after ~12 h. The solid was recovered, washed with toluene and hexanes, and dried *in vacuo* for ~12 h. Yield: 17.98 mg, 71.52 %.

[CoCp₂][Fe₈O₄pz₁₂Br₄] <u>AND</u> [CoCp₂]₂[Fe₈O₄pz₁₂Br₄]

Prepared analogously to [CoCp₂][Fe₈O₄pz₁₂Cl₄] and [CoCp₂]₂[Fe₈O₄pz₁₂Cl₄]. The products were not isolated. Spectroscopic characterization performed *in situ*.

3.6: References

(1) Claridge, S. A.; Castleman, A. W.; Khanna, S. N.; Murray, C. B.; Sen, A.; Weiss, P. S. *Acs Nano* **2009**, *3*, 244.

(2) Chevrel, R.; Sergent, M.; Hirrien, M. *J. Solid State Chem.* **1971**, *3*, 515.

(3) Schafer, H.; Eisenman, B; Muller, W. *Angew. Chem. Int. Ed.* **1973**, *12*, 694.

(4) Petrovic, A. P.; Lortz, R.; Santi, G.; Berthod, C.; Dubois, C.; Decroux, M.; Demuer, A.; Antunes, A. B.; Pare, A.; Salloum, D.; Gougeon, P.; Potel, M.; Fisher, O. *Phys. Rev. Lett.* **2011**, *106*, 017003.

(5) Wang, J.; Liu, X. C.; Xia, S. Q.; Tao, X. T. *J. Am. Chem. Soc.* **2013**, *135*, 11840.

(6) Talapin, D. V.; Lee, J. S.; Kovalenko, M. V.; Shevchenko, E. V. *Chem. Rev.* **2010**, *110*, 389.

(7) Choi, C. L.; Alivisatos, A. P. *Annu. Rev. Phys. Chem.* **2010**, *61*, 369.

(8) Auyeung, E.; Cutler, J. I.; Macfarlane, R. J.; Jones, M. R.; Wu, J.; Liu, G.; Zhang, K.; Osberg, K. D.; Mirkin, C. A. *Nat. Nanotechnol.* **2012**, *7*, 24.

(9) Kang, Y. J.; Ye, X. C.; Chen, J.; Qi, L.; Diaz, R. E.; Doan-Nguyen, V.; Xing, G. Z.; Kagan, C. R.; Li, J.; Gorte, R. J.; Murray, C. B. *J. Am. Chem. Soc.* **2013**, *135*, 1499.

(10) Degroot, M. W.; Corrigan, J. F. In *Comprehensive Coordination Chemistry II*; McCleverty, J. A., Meyer, T. J., Eds.; Pergamon: Oxford, 2003; Vol. 7, pp. 57–123.

(11) Reber, A. C.; Khanna, S. N.; Castleman, A. W. *J. Am. Chem. Soc.* **2007**, *129*, 10189.

(12) Reveles, J. U.; Clayborne, P. A.; Reber, A. C.; Khanna, S. N.; Pradhan, K.; Sen, P.; Pederson, M. R. *Nat. Chem.* **2009**, *1*, 310.

(13) Beaudron, S. A.; Batail, P.; Coulon, C.; Clerac, R.; Canadell, E.; Laukhin, V.; Melzi, R.; Wzietek, P.; Jerome, D.; Auban-Senzier, P.; Ravy, S. *J. Am. Chem. Soc.* **2005**, *127*, 11785.

 (14) Zheng, Z. P.; Long, J. R.; Holm, R. H. *J. Am. Chem. Soc.* **1997**, *119*, 2163.

(15) Yoon, B.; Luedtke, W. D.; Barnett, R. N.; Gao, J.; Desireddy, A.; Conn, B. E.; Bigioni, T.; Landman, U. *Nat. Mater.* **2014**, *13*, 807.

(16) Long, D. L.; Burkholder, E.; Cronin, L. *Chem. Soc. Rev.* **2007**, *36*, 105.

(17) Jin, S.; DiSalvo, F. J. *Chem. Mater.* **2002**, *14*, 3448.

(18) Liu, H.; Hsu, C.-H.; Lin, Z.; Shan, W.; Wang, J.; Jiang, J.; Huang, M.; Lotz, B.; Yu, X.; Zhang, W.-B.; Yue, K.; Cheng, S. Z. D. *J. Am. Chem. Soc.* **2014**, *136*, 10691.

(19) Roy, X.; Lee, C. H.; Crowther, A. C.; Schenck, C. L.; Besara, T.; Lalancette, R. A.; Siegrist, T.; Stephens, P. W.; Brus, L. E.; Kim, P.; Steigerwald, M. L.; Nuckolls, C. *Science* **2013**, *341*, 157.

(20) Steigerwald, M. L.; Siegrist, T.; Stuczynski, S. M. *Inorg. Chem.* **1991**, *30*, 4940.

(21) Roy, X.; Schenck, C. L.; Ahn, S.; Lalancette, R. A.; Venkataraman, L.; Nuckolls, C.; Steigerwald, M. L. *Angew. Chem Int Ed.* **2012**, *51*, 12473.

(22) Baran, P.; Boca, R.; Chakraborty, I.; Giapintzakis, J.; Herchel, R.; Huang, Q.; McGrady, J. E.; Raptis, R. G.; Sanakis, Y.; Simopoulos, A. *Inorg. Chem.* **2008**, *47*, 645.

(23) Wells, A. F. *Structural Inorganic Chemistry*; Oxford Univ. Press: Oxford, 1984; 5th Ed.

(24) Whatmore, R. W. *Rep. Prog. Phys.* **1986**, *49*, 1335.

(25) Chakraborty, I.; Baran, P.; Sanakis, Y.; Simopoulos, A.; Fachini, E.; Raptis, R. G. *Inorg. Chem.* **2008**, *47*, 11734.

(26) Orpen, A. G.; Connelly, N. G. *Organometallics* **1990**, *9*, 1206.

(27) Steigerwald, M. L.; Siegrist, T.; Stuczynski, S. M. *Inorg Chem* **1991**, *30*, 4940;

(28) Baran, P.; Boca, R.; Chakraborty, I.; Giapintzakis, J.; Herchel, R.; Huang, Q.; McGrady, J. E.; Raptis, R. G.; Sanakis, Y.; Simopoulos, A. *Inorg. Chem.* **2008**, *47*, 645.

Chapter 4: Superatomic Inorganic Clusters as Probes for Singlet Fission

4.1: Preface

This chapter is based on a journal article published in *Science Advances* entitled "Distinct Properties of the Triplet Pair State from Singlet Fission" by M. Tuan Trinh, Andrew Pinkard, Andrew B. Pun, Samuel N. Sanders, Elango Kumarasamy, Matthew Y. Sfeir, Luis M. Campos, Xavier Roy, and X.-Y. Zhu. I prepared and characterized the compounds investigated in this study along with Andrew Pun of the Campos group. Optical measurements and time-resolved spectroscopy were performed by Dr. Samuel Sanders of the Campos research group under the supervision of Dr. Matt Sfier of Brookhaven National Laboratory and by Dr. M. Tuan Trinh of the Zhu research group.

4.2: Introduction

Chapter 3 illustrated how ligand substitution of the $Co_6Te_8(PEt_3)_6$ with PEt_2Ph and P^nPr_3 could modify the superstructure of the resulting SACs. In this example, however, the electronics of the cluster core remained relatively unchanged, so I was interested in exploring how ligand modification might affect the complementary $Fe_8O_4pz_{12}Cl_4$ cluster perhaps in a non-innocent fashion. A collaboration began in which singlet fission chromophores were attached to the $Fe_8O_4pz_{12}Cl_4$ cluster by replacement of a pendant chloro- ligand. We were interested not only in how ligand modification would change the electronics of the cluster, but also in seeing if this study could lead to further insights about the singlet fission process.

4.2: Background

Singlet fission is a many-body photophysical process in molecules where the photoexcited singlet (S_1) splits into two triplets ($2 \times T_1$) with spin conservation.[1,2] Since its discovery, efficient singlet fission has been reported mostly for solids and aggregates of conjugated molecules[1,2] and a dominant mechanistic picture is the molecular dimer model,[3,4]

$$S_0 + S_1 \leftrightarrows {}^1(TT) \leftrightarrows 2\,T_1 \qquad (1),$$
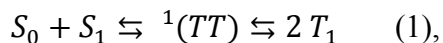
where S_0 is the ground state and the intermediate ${}^1(TT)$ is the correlated triplet pair with both singlet spin and double-excitation characters. Despite its prevalent use, Zhu and co-workers pointed out the inadequacy of the dimer model in describing inherently delocalized excitons in the solid state.[5,6] Indeed, exciton delocalization has been cited as an important driving force for singlet fission.[7–10] This problem is circumvented in recent demonstrations of efficient singlet fission in single molecules, particularly in dimers of acenes,[11–16] that allow for accurate application of the dimer model and for closely connecting experiment with theory.[17] The isolation of the transient ${}^1(TT)$ state in a single molecule leads to a much longer lifetime than that in the condensed phase, thus allowing spectroscopic characterization of this ambiguous and poorly understood state. This is exemplified in the detection by electron spin resonance spectroscopy in pentacene dimers of the quintet state, ${}^5(TT)$, which is mixed with the ${}^1(TT)$ state as predicted by the spin Hamiltonian.[18]

The ${}^1(TT)$ state is a single excited state with double excitation characters and differs from $2 \times T_1$ not only by the electronic and spin entangled nature of the former, but also by the presence of orbital overlap which changes its excitation energy from the sum

of two triplet energies. Scholes recently clarified some persistent confusions on the ^{1}(TT) state in theoretical descriptions.[19] The energetic difference between the correlated triplet pair state and two individual triplets, i.e., the triplet pair binding energy, can be as large as 1 eV, as is known for the excited states of oligoenes,[20–22] including carotenoids,[23] where the tightly bound triplet pair has been called the "dark" S_1 state serving as a sink for nonradiative recombination and a less tightly bound triplet pair (S*) has been associated with singlet fission.[15,24–26] In contrast, in prototypical model systems of pentacene or tetracene dimers (both covalent and van der Waals), computational analysis predicted little, if any, triplet pair binding energy.[17, 27–32] However, a recent finding of similar ^{1}(TT) lifetimes in poly-pentacene and bi-pentacene indicates that the triplet pair does not dissociate even in a long conjugated chain,[33] suggesting the correlated triplet pair state is more strongly bound than previously thought.

A major obstacle to a clear understanding of the ^{1}(TT) state is the lack of spectroscopic signatures from experiments. Zhu and coworkers applied time-resolved two-photon photoemission spectroscopy to quantitatively determine the energetic position of the ^{1}(TT) state from its ionization potential in crystalline pentacene,[34] tetracene,[10] and hexacene.[6] This approach is unambiguous only for hexacene(6) where the ^{1}(TT) state is energetically well separated from S_1 but is difficult for other singlet fission systems where the ^{1}(TT) states are in close energetic resonance with S_1. The most widely used technique to probe singlet fission has been transient absorption (TA) spectroscopy, but most studies to date have only identified spectral features assigned to S_1 and T_1 states and there has been little explanation as why these TA peaks nearly always overlap.[12–16, 35, 36] Exceptions to this prevalent practice can be found in the recent

61

work of Sanders et al.[11] who found in pentacene dimers of an ESA peak at ~ 690 nm whose magnitude is strongly correlated with the strength of inter-triplet electronic coupling, and in the work of Pensack et al.[37] who observed near-IR (1200-1400 nm) ESA in pentacene aggregates assigned to ^{1}(TT), but not to the triplet pair labeled ^{1}(T...T), which has lost electronic coherence but retained spin coherence. These two examples reveal the presence of spectroscopic signatures for the ^{1}(TT) state in transient absorption, but the origins of these transitions and their relationships to the energetics of the ^{1}(TT) state remain unclear.

The distinct electronic structure of the ^{1}(TT) state should be reflected not only in its spectroscopic signature, but also in its chemical and physical properties. The oft-cited motivation for nearly every recent paper on this subject has been the potential "usefulness" of singlet fission to solar energy conversion. The basic argument was put forward initially by Dexter for the sensitization of conventional solar cells by singlet fission chromophores[38] in 1979 but a more recent paper by Hanna and Nozik[39] on using singlet fission to increase the solar cell efficiency above the Shockley-Queisser limit energized the field. A number of research groups have explored the harvesting of triplet pairs from intermolecular singlet fission using solid interfaces between a singlet fission material and an electron or triplet acceptor material.[34, 40–43] These efforts have also led to the successful demonstration of singlet-fission based solar cells with quantum efficiencies exceeding 100%.[44] The recent demonstration of efficient intramolecular singlet fission in single molecules[11–16,36] opens the door to new opportunities for the realization of singlet fission sensitized solar cells.[45] A more exciting opportunity is the potential for the harvesting of two electron-hole pairs for photocatalysis, e.g, by coupling a singlet fission

molecule to a molecular or cluster-based catalytic center[46] to enable two-electron redox reactions. Unlike inter-molecular singlet fission in the solid state in which electronic delocalization[5,47] and entropy[10] are driving forces to split the ^{1}(TT) state to two electronically decoupled triplets (that can nonetheless retain spin coherence) on ultrafast time scales,[19] the confinement in a molecular dimer or oligomer traps the two triplets in the ^{1}(TT) state in a single molecule.[18, 33] Thus, instead of individual triplets at solid state interfaces, the harvesting of triplets in intramolecular single fission would likely come from the ^{1}(TT) state. However, the two triplets in the ^{1}(TT) state from intramolecular singlet fission can be tightly bound and charge or energy transfer from each triplet may be inhibited.

4.3: Approach
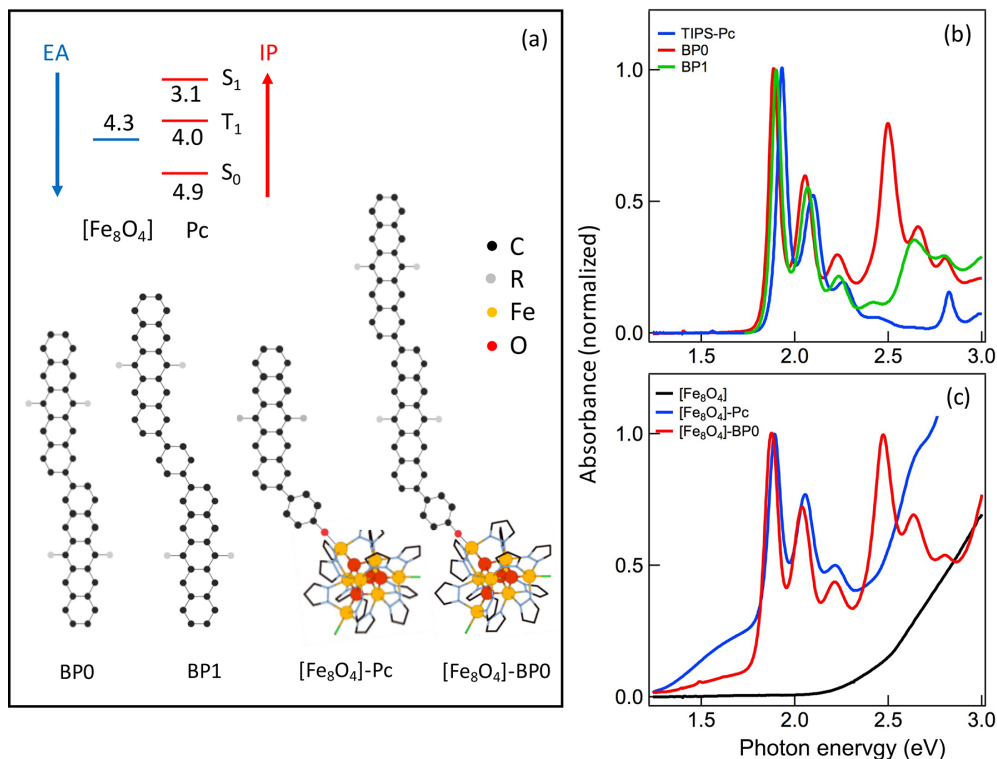
Figure 4.1. Model systems for intramolecular singlet fission and triplet harvesting. (a) Schematics of BP0, BP1, $[Fe_8O_4]$-Pc, $[Fe_8O_4]$-BP0 and $[Fe_8O_4]$-BP1. R = (triisopropysilyl)acetylene (TIPS) for $[Fe_8O_4]$-Pc and *n*-(octyldiisoproylsilyl)acetylene (NODIPS) for $[Fe_8O_4]$-BP0 and $[Fe_8O_4]$-BP1. The inset shows estimated ionization potential (IP) and electron affinity (EA) from electrochemical oxidation/reduction potentials of $[Fe_8O_4]$ and TIPS-pentacene; The left panels show optical absorption spectra of (b) TIPS-Pc, BP0, and BP1 in toluene and (c) $[Fe_8O_4]$, $[Fe_8O_4]$-Pc, $[Fe_8O_4]$-BP0 in dichloromethane solutions.

Here we use triisopropysilylacetylene functionalized pentacene (TIPS-Pc) dimers, each coupled at the 2-position without or with a phenylene spacer, BP0 and BP1 (Figure 4.1),[11] as well as pentacene dimers with different dihedral angles[17] (see Figure 4.4), as model systems to quantitatively probe the nature of the tightly bound ^{1}(TT) state from the excited state absorption spectra. Molecules of this type allow for the systematic tuning of electronic coupling between the two pentacene units and between the S_1 and the ^{1}(TT) states, as reflected in the singlet fission time constants of τ_{SF} = 0.76, 20, 220 ps and triplet

recombination time constants of τ_{AN} = 0.45, 16.5, and 270 ns for dimers with zero, one, and two phenylene spacers (BP0, BP1, BP2), respectively, obtained from analysis of TA spectra in the visible region.[11] We focused on the distinct ESA peak in the near-IR region (hv ~ 1 eV), which is a signature of the ^{1}(TT) state from singlet fission in BP0. Its intensity diminishes as the inter-triplet electronic coupling is lowered in BP1 or significantly decreases in bipentacene with different dihedral angles.[17] The ESA peak of ^{1}(TT) in BP0 closely resembles that of the S_1 state in the near-IR region, both show vibronic progressions of the aromatic ring breathing mode, and can be assigned to the ^{1}(TT)→S_n and S_1→S_n' transitions, respectively. To establish the distinct chemical properties of the ^{1}(TT) state, we use the redox-active molecular cluster $Fe_8O_4pz_{12}Cl_4$ (pz = pyrazolate), which we designate as [Fe_8O_4] for this chapter, as an electron acceptor,[48,49] and tether BP0 to [Fe_8O_4] through a Fe-phenoxide bond (schematically illustrated in Figure 4.1a). As a control, we replace the pentacene dimer BP0 with a pentacene monomer (Pc). It can then be shown that electron transfer from pentacene to [Fe_8O_4] occurs efficiently from a single T_1 state in pentacene ([Fe_8O_4]-Pc), but not from the tightly bound triplet pair state in [Fe_8O_4]-BP0. This finding establishes that the chemical property of the ^{1}(TT) state is distinctively different from that of an individual triplet and suggests that reducing inter-triplet electronic coupling in ^{1}(TT) might be needed for the harvesting of triplets from intramolecular singlet fission.

4.3: Synthesis

The synthesis of TIPS-Pc, BP0, and BP1 molecules,[11] BP0 with different dihedral angles,[17] and the [Fe_8O_4] cluster[49] has been previously described. To install the pentacene-based ligands on [Fe8O4], we first deprotonated the pendent phenol group

with an excess of sodium hydride in tetrahydrofuran (THF). The reaction mixture was filtered through a 0.2 μm syringe filter and added dropwise to a solution of [Fe$_8$O$_4$] in THF. A 1:1 stoichiometric ratio of the ligand to [Fe$_8$O$_4$] was used to prepare the monosubstituted clusters, which were purified by reverse phase chromatography. Synthetic details are presented at the end of this chapter.

4.4: Optical and Transient Absorption

The TIPS-Pc, BP0, and BP1 samples were dissolved in dry toluene (with a concentration < 100 mM) and kept free from oxygen and moisture for optical measurements on a Shimadzu UV 1800 UV-Vis spectrophotometer. UV-Vis absorption spectra of BP0 and BP1, Figure 4.1b, show a slight red-shift from that of TIPS-Pc, but contains otherwise nearly identical vibronic features near the absorption threshold (S0→ S1).[11] Solutions of [Fe$_8$O$_4$], [Fe8O4]-Pc, or [Fe$_8$O$_4$]-BP0 in chloroform were used for absorption measurements. Optical absorption spectra of [Fe$_8$O$_4$], [Fe$_8$O$_4$]-Pc, and [Fe$_8$O$_4$]-BP0 in Figure 4.1c will be subsequently discussed.

.   To investigate singlet fission and triplet transfer, femtosecond transient absorption (fs-TA) spectroscopy was employed. The samples were dissolved in dry toluene and kept free from oxygen and moisture. The pump pulse came from an optical parametric amplifier (tunable from UV to the near IR, 100 fs pulse width, 1 KHz rep-rate). The probe pulse is a white-light supercontinuum (from 450 to 850 nm and from 850 to 1600 nm for the visible and near IR range, respectively). The delay between pump and probe pulses was controlled by a translational stage with a delay time up to 3 ns. The detection consists of a pair of multichannel detector arrays coupled to a high-speed data acquisition system (HELIOS, Ultrafast System Inc.). The sample solution was at room temperature

during measurement. The ns-μs transient absorption measurements were carried out on the same setup as femtosecond transient absorption with the same pump pulse. The probe pulse is a white-light supercontinuum (from 400 to 1600 nm) generated by a supercontinuum laser (Leukos). The laser pulse width was ≤ 1 ns at 2 kHz. The pump-probe delay was controlled electrically.

The triplet sensitizing experiment was carried out on the same setup except the white-light probe beams were generated by a picosecond laser and the pump-probe delay was controlled electrically. A mixture of a (bi)pentacene compound and an excess of anthracene was dissolved in toluene with the concentration of anthracene ~100x that of (bi)pentacene. Photoexcitation at 3.35 eV creates singlets in anthracene which undergo intersystem crossing to form triplets. The triplets in anthracene subsequently transfer to (bi)pentacene molecules via diffusional collisions on a time scale of 1-2 ms.

4.4: Spectroscopic Signatures of the ^{1}(TT) State

Transient absorption spectroscopy was used to probe singlet fission in BP0 and BP1.[11] The S_1 state of each pentacene dimer was excited at $h\nu_1$ = 2.1 eV and probe the subsequent dynamics from the transient absorption of a white-light continuum. Figure 4.2a-b show TA spectra at selected pump-probe delays, Δt = 0.1 (red), 10 (purple), and 100 ps (blue) for BP0. The visible parts of the TA spectra have been discussed extensively before and the broad positive transient absorption features at Δt < 1 ps and Δt > 2ps are assigned to the ESA of S_1 and T_1, respectively.[11] The latter is confirmed by the ESA spectrum of T_1 obtained from sensitization (black). Based on the calculated triplet energies in pentacene (T_3 and T_4 are close in energy and are not distinguished here),[50] the ESA peak at 2.42 eV is assigned to the T1→T3 transition. For the triplet pair from

singlet fission, this transition corresponds to $^1(T_1T_1) \rightarrow {}^1(T_1T_3)$. In each case, the ESA transition also shows vibronic progression ($h\nu_{vib} \sim 0.17$ eV) similar to those in the ground state absorption spectrum.[11] The singlet decay and triplet formation can be clearly seen from kinetic profiles at probe photon energy of $h\nu_2 = 2.13$ (grey) and 2.42 eV (green), respectively (Figure 4.2c) with $\tau_{SF} = 0.7$ ps;[11] note that there is overlapping contribution to ESA signal at $h\nu_2 = 2.42$ eV from the singlet at short times. The two triplets confined to the pentacene dimer can be assigned to $^1(TT)$ which decays on the time scale of $\tau_{TT1} = 450$ ps (see green curve at long pump-probe delays in Figure 4.2c), much shorter than the 30 µs lifetime of a single triplet.[11] Here we focus on the near-IR region which provides key spectroscopic insight into the triplet pair state.
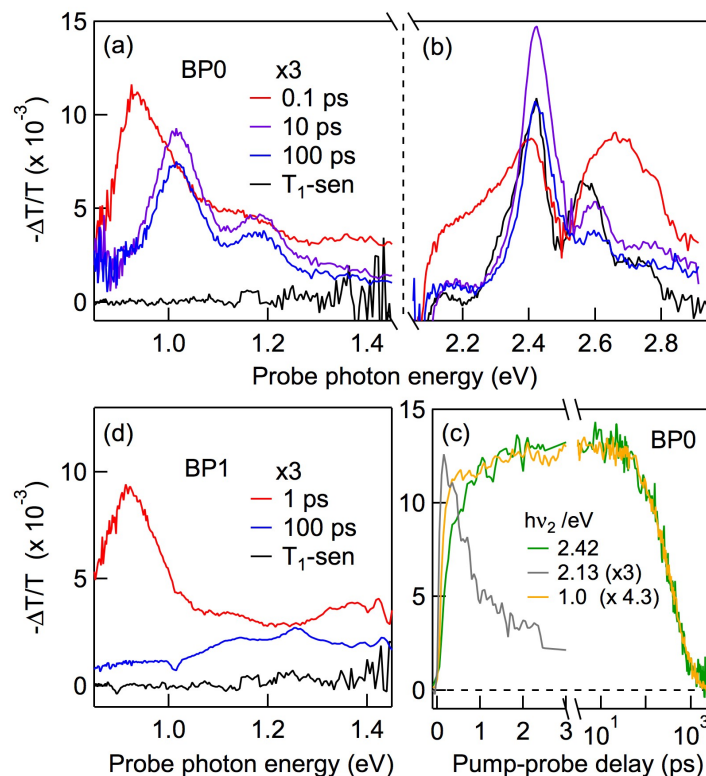
Figure 4.2. Transient absorption in the near-IR and visible regions reveal singlet and triplet characters of $^1(TT)$. TA spectra in (a) the near-IR and (b) the visible regions for BP0 at different pump-probe delays, Δt = 0.1 (red), 10 (purple), and 100 (blue) ps, following excitation at time zero by $h\nu_1 = 2.1$ eV. Also shown in

(a) and (b) is the triplet TA spectrum from sensitization (black). (c) kinetic profiles from TA spectra for BP0 at the indicate probe photon energies. (d) TA spectra at $\Delta t = 1$ (red) and 100 (blue) ps for BP1 following excitation at time zero by $h\nu_1 = 2.1$ eV. Also shown is the corresponding triplet spectrum (black) from sensitization.

There is a distinct ESA peak at 0.922 ± 0.005 eV when the singlet dominates at $\Delta t = 0.1$ ps (red), Figure 4.2a; this peak is also accompanied by a vibronic feature on the higher energy side, with $h\nu_{vib} \sim 0.17$ eV, similar to the vibronic progressions of $S_0 \rightarrow S_1$, $T_1 \rightarrow T_n$, and $^1(T_1T_1) \rightarrow {}^1(T_1T_n)$ discussed above. This ESA is assigned to an $S_1 \rightarrow S_n'$ transition, with transition energy close to the $S_1 \rightarrow S_2$ transition for a single pentacene molecule. In the absorption spectrum of TIPS-Pc in Figure 4.1b (blue), there is a weakly allowed $S_0 \rightarrow S_2$ peak at 2.82 eV, in agreement with two-photon absorption spectrum of the same molecule.[51] Given the $S_0 \rightarrow S_1$ peak at 1.93 eV (blue spectrum in Figure 4.1b), we obtained the $S_1 \rightarrow S_2$ transition energy at 0.89 eV. In conjugated bipentacene dimers, the singlet states are described by linear combinations of two localized states on each pentacene chromophore.[17] While both symmetric and antisymmetric linear combinations are possible, the optically bright S_1 state in BP0 is of odd parity (u). Therefore, excited state transitions must occur to S_n' states of even parity (g). The 0.92 eV peak is then assigned to a transition from S_1 to the symmetric linear combination of the monomer S_2 states.

At longer pump-probe delays, e.g., $\Delta t = 10$ (purple) or 100 ps (blue), when there is only the triplet pair state, the ESA spectrum blue-shifts to 1.012 ± 0.005 eV and the vibronic signature becomes better resolved. This ESA peak does not originate from a $T_1 \rightarrow T_n$ transition, as it is completely absent in the triplet absorption spectrum (black) from

69

sensitization. Based on the similarity of this ESA peak to that of the $S_1 \rightarrow S_n'$ transition at earlier times, the former is assigned to a $^1(TT) \rightarrow S_n$ transition. As the $^1(TT)$ state in BP0 is expected to correspond to the totally symmetric representation,[17] it will be of opposite parity to the S_1 state and will exhibit a distinct set of excited state transitions to states of odd parity. S_n is expected to be close in energy to S_n' since the difference in the $S_1 \rightarrow S_n'$ and $^1(TT) \rightarrow S_n$ transition energies, $\Delta E = 90$ meV is close to the predicted exoergicity of ~100-150 meV for singlet fission in bi-pentacene.[17,27,29–32] The small energy spacing implies that S_n and S_n' likely both originate from different linear combinations of the S_2 monomer state of different parity. Note that, unlike the results shown here for the pentacene dimer, the near-IR ESA assigned to $^1(TT)$ in pentacene aggregates does not show vibronic features.[37]

The ESA spectrum of the $^1(TT)$ state reveals its delocalized singlet and localized triplet characters in the near-IR and the visible regions, respectively. The terms "delocalized singlet" or "delocalization" are used to emphasize $^1(TT)$ in a single electronic state that can be viewed approximately as two T_1 states (on two pentacene units) that are electronically coupled and coherent. Likewise, the term "localized triplet" or "localization" refers to a T_1 state on an individual pentacene unit with physical properties that are insensitive to the presence or absence of electronic coupling and coherence with a neighboring T_1 state. Spectroscopically, delocalization and localization are reflected in the transitions $^1(TT) \rightarrow S_n$ and $^1(T_1T_1) \rightarrow {}^1(T_1T_n)$, respectively. Note the two notations, $^1(TT)$ and $^1(T_1T_1)$, describe the same triplet pair state. The kinetic profiles (Figure 4.2c) for the $^1(TT) \rightarrow S_n$ (orange) and $^1(T_1T_1) \rightarrow {}^1(T_1T_n)$ (green) transitions are

similar; the difference at short time scales (< 1 ps) can be attributed to the different overlapping contributions from ESA of S_1. Note that transitions to S_n is allowed from ^{1}(TT), but spin-forbidden from ^{3}(TT) or ^{5}(TT). The perfect agreement between the decays of ^{1}(TT)$\rightarrow S_n$ and the $^1(T_1T_1)\rightarrow{}^1(T_1T_n)$ signals suggests that there are negligible transitions within the triplet pair manifold, e.g., ^{1}(TT)$\rightarrow{}^5$(TT) or ^{1}(TT)$\rightarrow{}^3$(TT), during the lifetime (450 ps) of the triplet pair state.

Supporting the conclusion that delocalization or inter-triplet electronic coupling in the ^{1}(TT) state is reflected in the ^{1}(TT)$\rightarrow S_n$ transition strength, we find that, in BP1, the weakening of the inter-T_1 electronic coupling diminishes its delocalized character as reflected in the ^{1}(TT)$\rightarrow S_N$ transition strength, Figure 4.2d, where the near-IR peak for ^{1}(TT) at long times, e.g., Δt = 100 ps (blue) becomes not resolvable from the broad background, in distinct contrast to the $S_1\rightarrow S_n$ peak at Δt = 1 ps. In contrast, the localized character represented by the $^1(T_1T_1)\rightarrow{}^1(T_1T_n)$ transition in the visible region remains.[11]

To more quantitatively isolate the singlet spectrum from that of the triplet pair, global analysis was performed based on a sequential kinetic model, $S_1\rightarrow{}^1$(TT)$\rightarrow S_0$.[11] The resulting S_1 (red) and ^{1}(TT) (blue) spectra are shown in Figure 4.3. The global analysis yields time constants of 0.75±0.05 ps and 460±10 ps for singlet fission and triplet pair annihilation, respectively, in agreement with the previous report.[11] Similar to the S_1-S_n' transition, the ^{1}(TT)-S_n transition is also characterized by vibronic peaks assigned to 0-0 and 0-1 transitions, with vibrational energy spacing of 0.16-0.17 eV, which corresponds to the ring breathing mode of pentacene along the short molecular axis.[52] In addition to the near-IR peak, the ^{1}(TT) state in BP0 also features a distinct peak at 1.810±0.005 eV.

Similar to the 1.012 ± 0.003 eV transition, the peak at 1.810 ± 0.005 eV diminishes as the inter-triplet coupling weakens in BP1 and BP2.[11] Thus, the peak at 1.810 ± 0.005 also reflects the singlet character of the $^1(TT)$ state and can be assigned to a $^1(TT) \rightarrow S_n$" transition. Due to the overlapping bleaching feature ($S_0 \rightarrow S_1$), we are not able to resolve vibronic progression for this transition.
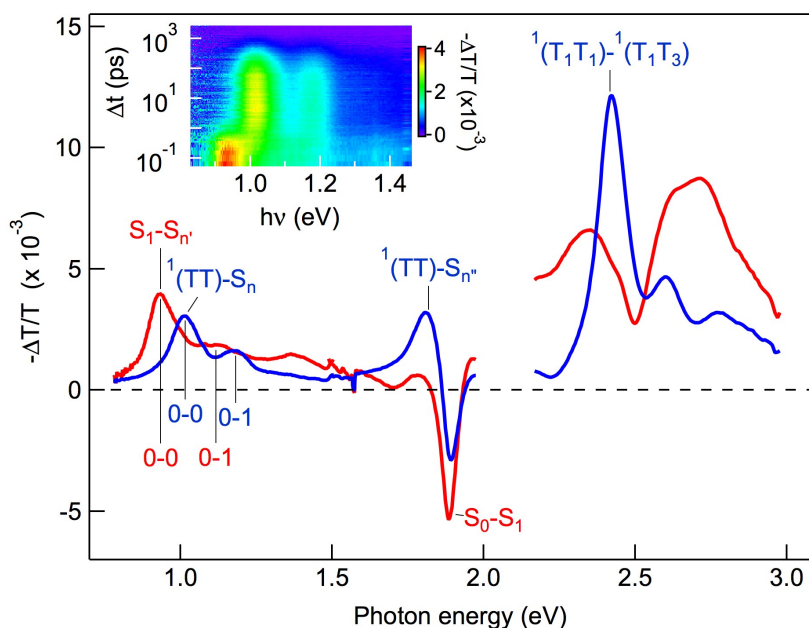
Figure 4.3. Transient absorption spectra of BP0 for the S_1 and $^1(TT)$ states from global analysis. Red: singlet state. Blue: triplet pair state. Inset: Two-dimensional pseudo-color (intensity) plot of TA spectra following excitation at time zero by $h\nu_1 = 2.1$ eV. The transitions, along with vibronic progressions, are shown on each spectrum.

Further supporting the conclusion that the near-IR $^1(TT) \rightarrow S_n$" transition is a spectroscopic signature of the tightly bound triplet pair state, we turn to modified BP0 molecules with different dihedral angles. In this approach, we control the dihedral angle twist by steric hindrance from the phenyl group attached to the 1-position of one or both pentacene units in the bi-pentacne molecule, as shown schematically in the insets in Figure 4.4.[17] Computational analysis gives dihedral angles between the two pentacene

72

molecules of 42° and 57°, and these two molecules are therefore labeled as BP-42 and BP-57, respectively.[17] For comparison, the dihedral angle in BP0 is 37°; thus, BP0 BP-37. Theoretical analysis showed that the inter-triplet electronic coupling decreases with increasing dihedral angle.[17] The singlet fission time constants are τ_{SF} = 0.76 ps, 1.69 ps, and 3.38 ps and the corresponding triplet-triplet annihilation time constants are τ_{SF} = 0.45 ns, 1.6 ns, and 5.2 ns for BP-37, BP-42, and BP-57, respectively.[17] Figure 4.4 shows the near-IR region of the S_1 (red) and ^{1}(TT) (blue) ESA spectra for BP-42 (upper) and BP-57 (lower). We multiply the ^{1}(TT) spectra by factors of 2.5 and 4.6 for BP-42 and BP-57, respectively, to normalize the ^{1}(TT)-Sn peak intensity to the S_1-Sn' intensity in each case. For comparison, the normalization factor would be 1.25 for BP-37 in Figure 4.3. Thus, relative to the S_1-S_n' transition, the ^{1}(TT)-S_n transition strength is 80%, 40%, and 22% for BP-37, BP-42, and BP-57, respectively. This confirms the correlation of between the ^{1}(TT)-S_n ESA transition strength and the inter-triplet electronic coupling in the ^{1}(TT) state.
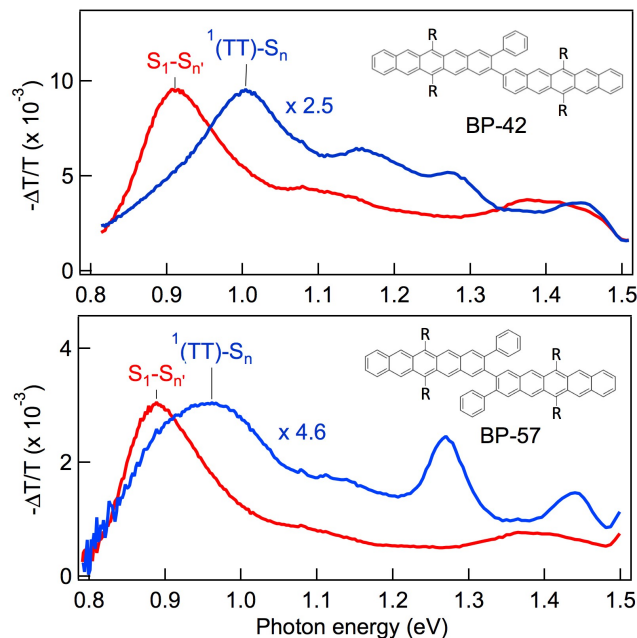
Figure 4.4. Transient absorption of the ^{1}(TT) state in the near-IR region depends on electronic coupling. Near-IR TA spectra of BP-42 (upper) and BP-57 (lower). The ^{1}(TT) spectra (blue) have been multiplied by factors of 2.5 and 4.6 for BP-42 and BP-57, respectively, to normalize to peak intensities of ^{1}(TT) to those S_1 (red).

In all the pentacene dimers investigated here, the decay rate of the triplet pair state is also found to be strongly correlated with the extent of delocalization in the ^{1}(TT) state, which is reflected in the ^{1}(TT)-S_n transition strength. This is understood as the rate of T_1-T_1 annihilation as determined by the inter-pentacene electronic coupling strength, addressed in detail elsewhere.[11, 17]

The relative amplitudes of the 0-0 and 0-1 transitions allow us to estimate the Huang-Rhys factor (S) in each case and, thus, the relative shifts in the potential energy surfaces involved. The Huang-Rhys factor is related to the offset (ΔQe) in the equilibrium positions of the two potential energy surfaces (PES) in an optical transition: $S = 0.5\alpha(\Delta Q_e)^2$, where $\alpha = \mu\omega/\hbar$; μ is the reduced mass and ω is the angular frequency of the vibration.[53] In the harmonic oscillator and low-temperature

74

approximation appropriate for the pentacene ring breathing mode at room temperature, the ratio in the Franck-Condon factors (and the ratio in peak intensities) between the 0-1 and 0-0 transition is equal to the Huang-Rhys factor.[53] Thus, we obtain S = 0.36±0.05 and 0.45±0.05 for the $S_1 \rightarrow S_3$ and $^1(TT) \rightarrow S_3$ transitions, respectively from the near-IR ESA spectra for BP0 in Figure 4.3. For comparison, we obtain from the optical absorption spectrum a value of S = 0.55±0.05 for the S0-S1 transition.[11] For the pentacene ring-breathing mode, we neglect the difference in equilibrium geometries between S_n' and S_n, since they both likely come from the linear combination of S_2 in each pentacene chromophore.

The spectroscopic results obtained above allow us to construct potential energy surfaces for singlet fission in BP0, Figure 4.4. While there are four possible arrangements of the PES from experimental ΔQ values, Figure 4.5 shows the scenario more consistent with expectation of increasing nuclear displacement with excitation energy. The offset in equilibrium positions of the S_1 PES and the $^1(TT)$ PES: ΔQe ~ 0.081 Å is also consistent with theoretical results on the covalent dimer.[17] The barrierless nature of the crossing point between S_1 and $^1(TT)$ explains the fast singlet fission rate for BP0. Furthermore, the PES of $^1(TT)$ crosses that of S_0 with only two vibrational quanta on the former; this opens up an efficient non-radiative decay pathway. Indeed, the nonradiative lifetime of $^1(TT)$ (450 ps in BP0) is shorter than that of the radiative lifetime (~ 13 ns) of S_1 in TIPS-pentacene.[11,54] While Figure 4.5 is only an approximation given the uncertainties in the spectroscopic determination of Huang-Rhys factors, it represents the first estimation of PES for singlet fission from experimental data.
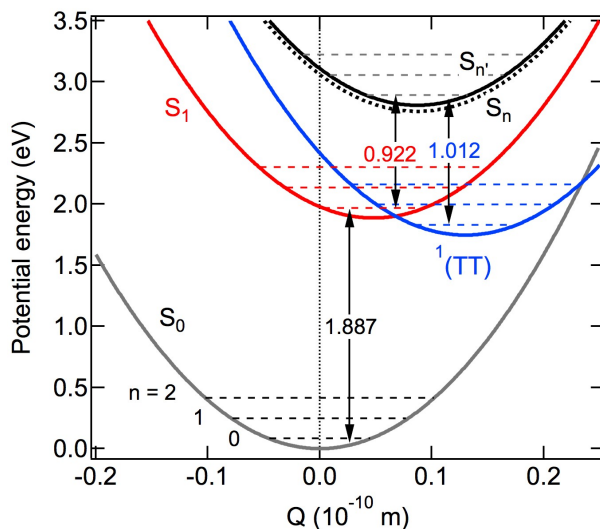
Figure 4.5. Estimated potential energy surface for single fission and near-IR ESA for BP0.

4.5: Distinct Chemical Properties of the ^{1}(TT) State

The above spectroscopic analysis of singlet fission in BP0 provides evidence for a strong coupled triplet pair state, ^{1}(TT), whose delocalized and localized characters are revealed in excited state absorption in the near-IR and visible regions, respectively. We also we show that the tightly bound triplet pair state exhibits different chemical properties from that of an individual triplet.

The inset in Figure 4.1a shows the estimated values for the ionization potential (IP) and electron affinity (EA) for TIPS-Pc and [Fe$_8$O$_4$], respectively. These values are obtained from the electrochemical oxidation potentials for TIPS-Pc[55] and [Fe$_8$O$_4$],[56] respectively, based on the reference value of the Ag/AgCl electrochemical potential at 4.4 eV below vacuum energy (E_V).[57] Also shown are the estimated IPs of S_1 and T_1 states from the excitation energies of TIPS-Pc. The use of IPs and EAs of both ground and excited states allows us to accurately put all relevant energy levels on the same single particle diagram, as discussed in detail previously.[58] Note that the energy levels obtained

from electrochemistry are adiabatic single particle energies and can be used to approximate the vertical single particle energies, i.e., highest occupied molecular orbital (HOMO) and lowest unoccupied molecular orbital (LUMO), when the reorganization energies are negligible.[58] Given this approximate energy level diagram, we expect efficient electron transfer from either the T_1 or the S_1 in pentacene to the $[Fe_8O_4]$ cluster. Figure 4.1c compares optical absorption spectra of $[Fe_8O_4]$ cluster (black) and BP0 (green), and that of compounds $[Fe_8O_4]$-Pc (red) and $[Fe_8O_4]$-BP0 (blue). The absorption spectra of both $[Fe_8O_4]$-Pc and $[Fe_8O_4]$-BP0 primarily arise from the sum of the absorption spectra of $[Fe_8O_4]$ and that of pentacene or bipentacene. An additional broad feature that overlaps with the constituents spectra is visible below 1.75 eV and this tail could arise from a charge transfer (CT) state from the Pc-PhO- or BP0-PhO- ligand to the $[Fe_8O_4]$ cluster.

The energy level alignment in Figure 4.1a suggests that, in addition to direct photoexcitation of the CT state, electron transfer can occur from T_1 in pentacene to $[Fe_8O_4]$ to indirectly form the CT state. We find that CT and T_1 are strongly coupled resonantly. When the CT state in $[Fe_8O_4]$-Pc or $[Fe_8O_4]$-BP0 is directly excited at $h\nu =$ 1.65 eV, Figure 4.6a, we observe in each case a transient absorption (TA) spectrum characteristic of the T_1 state in pentacene, including an excited state absorption (ESA) peak at ~2.4 eV and ground state bleaching at 1.88 and 2.05 eV. While a small differences in the TA spectra for $[Fe_8O_4]$-Pc (green) and $[Fe_8O_4]$-BP0 (red) is observed, they all match very well with their T_1 spectra obtained by sensitization. Neither the isolated $[Fe_8O_4]$ nor the uncoupled pentacene molecules absorb light below ~1.75 eV. Excitation of isolated $[Fe_8O_4]$ at higher photon energies results in completely different

TA spectra. The ultrafast formation of T_1 within experimental time resolution (~100 fs) from the selective excitation of CT indicates that the cluster and pentacene ligands are strongly electronically coupled. Supporting this conclusion, we observe in triplet sensitization experiment that the observable T_1 signal from $[Fe_8O_4]$-Pc is order of magnitude lower than that from TIPS-Pc.
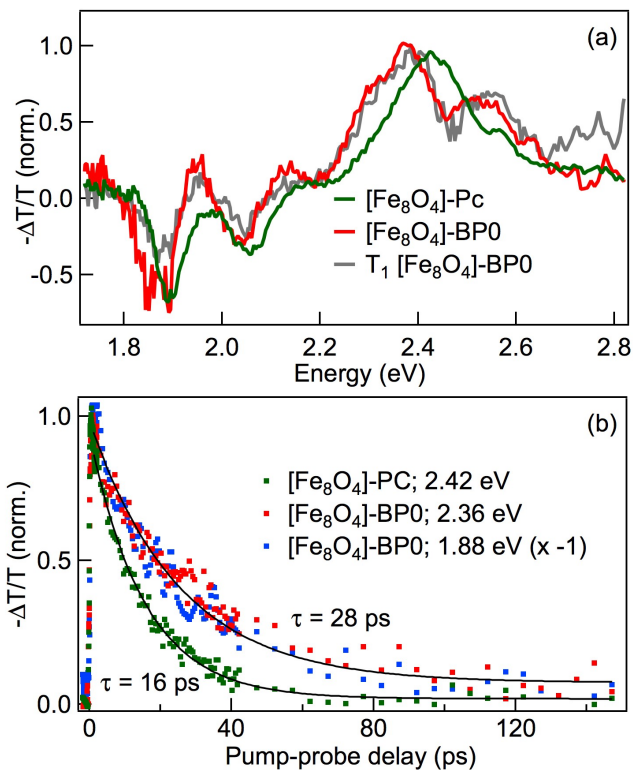
Figure 4.6. Transient absorption reveals the strong coupling of CT sate to T_1. (a) Transient absorption spectra at 1 ps for $[Fe_8O_4]$-Pc (green) and $[Fe_8O_4]$-BP0 (red), and $[Fe_8O_4]$-BP1 (blue) upon CT excitation of 1.65 eV. The grey curve is the triplet spectrum of $[Fe_8O_4]$-BP0 from triplet sensitization. (b) Triplet decay dynamics for $[Fe_8O_4]$-Pc (green), $[Fe_8O_4]$-BP0 (red and blue for ESA and ground state bleaching respectively). The solid curves are single exponential fits with the indicated lifetimes (t = 16 ± 2 ps for $[Fe_8O_4]$-mPc and 28 ± 3 ps for $[Fe_8O_4]$-BP0.

The coupled T_1-CT state features first-order decay kinetics well described by single-exponential decays (solid curves in Figure 4.2b), with time constants of $\tau_{CT\text{-}T1} = 28$ ± 3 ps and 16 ± 2 ps for $[Fe_8O_4]$-Pc and $[Fe_8O_4]$-BP0, respectively. The simple first-order kinetics is reflected in both the decay in T_1-like ESA signal (red dots) and the recovery in

ground state bleaching (blue dots) for $[Fe_8O_4]$-BP0 in Figure 4.6b The T_1-CT decay constant is five orders of magnitude shorter than that of an individual T_1 state in pentacene or bipentacene molecules.[11] Since no fluorescence emission is observed for any of the cluster-pentacene complexes, we assign the fast decay in the T_1-CT state to non-radiative recombination. Both charge transfer across the pentacene-cluster interface and the presence of paramagnetic Fe atoms can couple to electron spins, thus facilitating recombination.[59]

Unlike the strong coupling of individual T_1 in pentacene or bipentacene to the CT state at their interfaces to $[Fe_8O_4]$, triplet state in the tightly bound $^1(TT)$ in BP0 is revealed to not undergo charge transfer to the electron accepting cluster. Figure 4.7a shows TA spectra for $[Fe_8O_4]$-BP0 as a function of pump-probe delay, following initial photo-excitation at $h\nu_1 = 2.1$ eV. Figure 4.7b shows horizontal cuts at selected pump-probe delays ($\Delta t = 0, 10, 100$ ps), along with a T1 spectrum obtained from sensitization of $[Fe_8O_4]$-BP0. At this excitation photon energy, BP0 is known to undergo efficient singlet fission[11] and the results for $[Fe_8O_4]$-BP0 are nearly identical to those in BP0. Initially ($\Delta t = 0$ ps, red spectrum in Figure 4.7b), the TA spectrum is that of S_1 characterized by the broad excited state absorption (ESA) in the visible region and a vibronically resolved ESA in the near-IR. The singlet exciton decay and triplet rise in $[Fe_8O_4]$-BP0 are both characterized by a single-exponential lifetime of $\tau_{SF} = 0.55 \pm 0.02$ ps, which is slightly shorter than the corresponding process in BP0 ($\tau_{SF} = 0.76$ ps).[11] Figure 4.7d compares the $^1(TT)$ decay dynamics in $[Fe_8O_4]$-BP$_0$, as monitored by the decays of ESA signals attributed to both triplet (2.36 eV, red) and singlet (0.97 eV, green) character. For comparison, we also show in Figure 4.7d the $^1(TT)$ decay dynamics

in BP0 (2.36 eV, blue). The three decays traces are superimposable. The data for $[Fe_8O_4]$-BP0 is well described by a single exponential decay with time constant of $\tau_{TT} = 0.42 \pm 0.03$ ns, which is, within experimental uncertainty, identical to that of BP0. In stark contrast to the efficient charge transfer from a single T_1 state in $[Fe_8O_4]$-Pc, there is no measurable charge transfer from the tightly bound ^{1}(TT) state in $[Fe_8O_4]$-BP0.
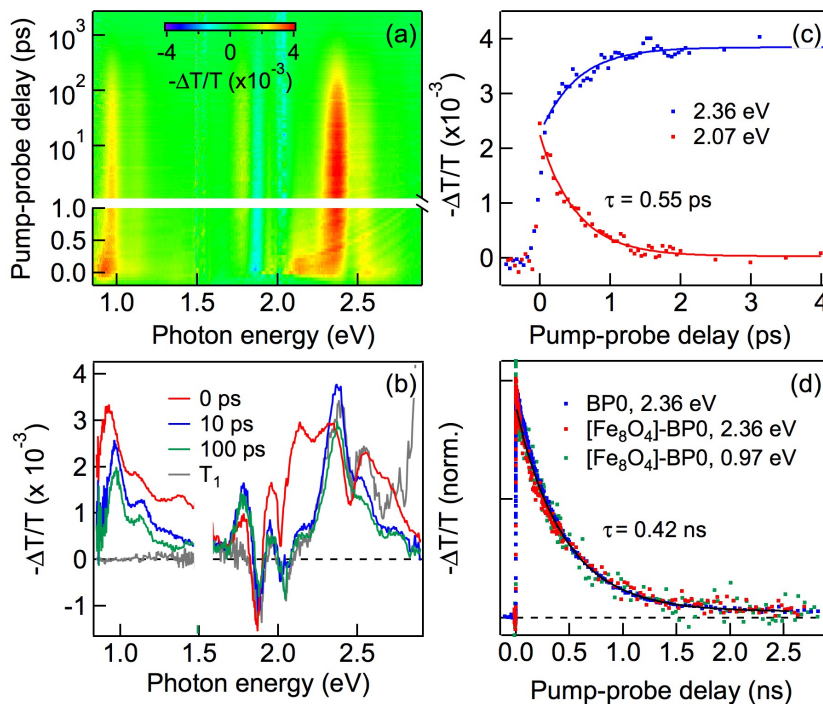
Figure 4.7. Transient absorption (TA) spectra and dynamics of $[Fe_8O_4]$-BP0 under 2.1 eV excitation. (a) 2D pseudocolor plot of TA (= $-\Delta T/T$, T: transmission) as a function of pump-probe delay (Δt) and probe photon energy. (b) TA spectra at $\Delta t = 0$ (red), 10 (blue), and 100 (green) ps, along with T_1 spectrum from sensitization (grey). (c) Singlet fission dynamics, as represented by S_1 decay at 2.07 eV (red) or ^{1}(TT) buildup at 2.36 eV (blue). (d) Comparison of ^{1}(TT) decay dynamics for $[Fe_8O_4]$-BP0 and BP0.

4.6: Conclusions and Outlook

Using covalently-linked pentacene dimers as model systems, we showed strong evidence for a tightly bound triplet pair state, which reveals its delocalized ^{1}(TT) and localized T_1 characters in the near-IR and visible ESA spectra, respectively. The near-IR

ESA spectra can be assigned the $^1(TT) \rightarrow S_n$ transition, which is similar to the $S_1 \rightarrow S_n'$ transition, with vibrational progression corresponding to the well-known aromatic ring breathing mode. The $^1(TT) \rightarrow S_n$ transition is an indicator of the inter-triplet coupling strength; when a phenylene spacer is inserted between the pentacene moieties (BP_1) or varied the angle between the pentacene moieties (BP45, BP90, and 1,2-BP) to decrease this coupling, we find the $^1(TT)) \rightarrow S_n$ ESA peak decreases. This is in contrast to the spectrum in the visible region, assigned to the $^1(T_1T_1)) \rightarrow ^1(T_1T_3)$ transition present with similar intensities for all bipentacene molecules. Using the electron-accepting $Fe_8O_4pz_{12}Cl_4$ molecular cluster linked to pentacene and bi-pentacene (BP0), we show that electron transfer to the cluster occurs efficiently from a single T_1, but not from the $^1(TT)$ state. Thus, the tightly bound $^1(TT)$ state exhibits distinctively different chemical reactivity than that of an individual T_1 state.

4.7: Synthetic Details

Unless stated otherwise, reactions were conducted in oven-dried glassware under an inert atmosphere.
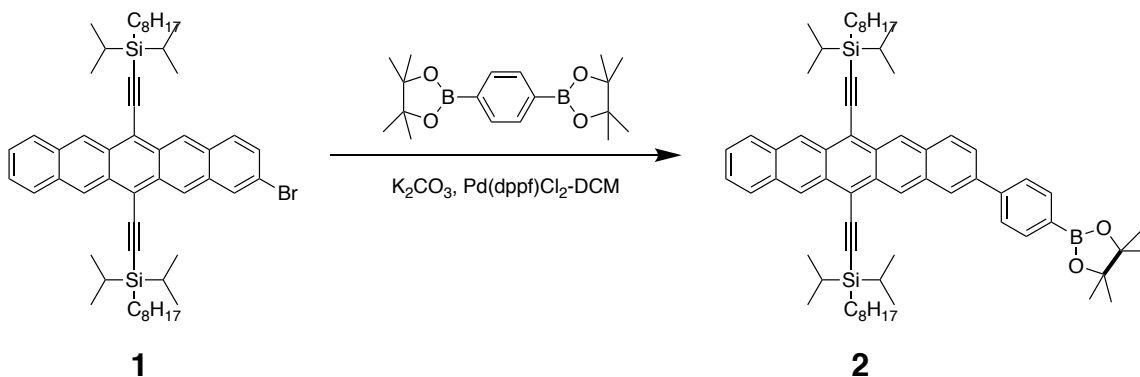
1 (1.5 g, 1.75 mmol), 1,4-benzenediboronic acid bis(pinacol) ester (1.73 g, 5.25 mmol) and Pd(dppf)Cl$_2$·DCM (71.1 mg, 0.09 mmol) were added to a reaction vial,

followed by sequential vacuum and argon atmospheres to degas the solids. K_2CO_3 (1.2 g, 8.75 mmol) was then dissolved in 4.5 mL H_2O and degassed. The solids were then dissolved in 45 mL of a mixture of 9:1 tetrahydrofuran (THF):K_2CO_3 in H_2O solution and allowed to stir at 70 °C overnight in the dark. The reaction was then brought to room temperature and extracted with dichloromethane and the combined organic layers were washed with deionized water and brine, dried over sodium sulfate, filtered and concentrated. The crude reaction mixture was then purified by column chromatography using 25% to 50% dichloromethane in hexanes as the eluent to obtain **2** as a deep blue solid (973 mg, 56.7% yield).

^{1}H-NMR (500 MHz, CDCl$_3$, δ ppm): 9.36 (s, 1H), 9.32 (s, 3H) 8.20 (s, 1H), 8.09 (d, 1H), 8.03- 8.00 (m, 4H), 7.84 (d, 2H), 7.76 (d, 1H), 7.46-7.42 (m, 2H), 1.80 (m, 4H), 1.56 (m, 6H), 1.45- 1.35 (m, 54H), 0.99 (m, 4H), 0.83 (m, 6H).

^{13}C-NMR (125 MHz, CDCl$_3$, δ ppm): 143.47, 138.19, 136.40, 135.43, 132.39, 132.35, 132.32, 131.55, 130.93, 130.78, 130.69, 130.62, 129.34, 129.19, 128.68, 126.77, 126.54, 126.33, 126.29, 126.12, 126.02, 125.57, 118.44, 118.32, 107.66, 107.51, 104.54, 104.51, 83.89, 34.05, 34.02, 33.97, 31.97, 31.92, 29.50, 29.47, 29.39, 29.37, 25.01, 24.96, 24.92, 24.74, 22.64, 18.71, 18.44, 14.08, 14.06, 12.18, 10.47.

MS (ESI): Calculated [M]$^+$: 980.6505; Observed: 980.6499
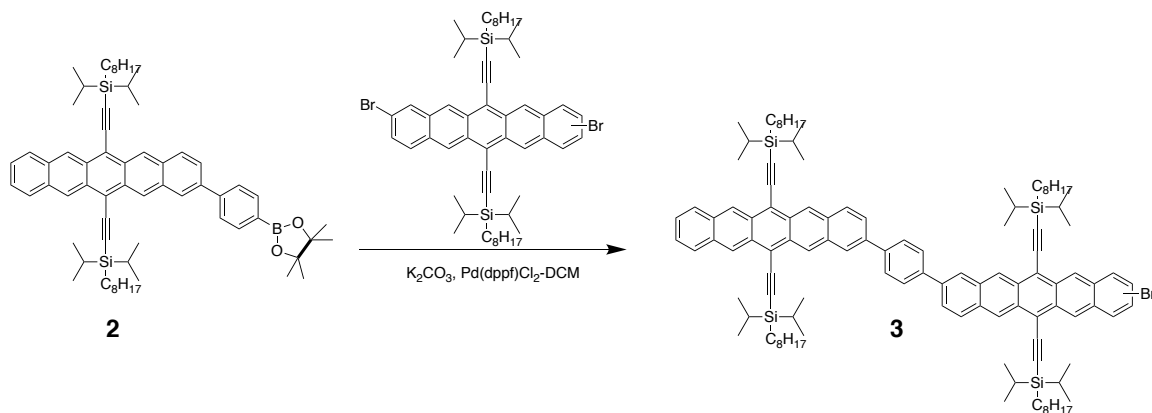
2 (250 mg, 0.25 mmol), dibromo NODIPS pentacene (586 mg, 0.625 mmol) and Pd(dppf)Cl$_2$·DCM (10.2 mg, 0.013 mmol) were added to a reaction vial, followed by sequential vacuum and argon cycles to degas the solids. K$_2$CO$_3$ (173 mg, 1.25 mmol) was then dissolved in 1.2 mL H$_2$O and degassed. The solids were then dissolved in 12 mL of a mixture of 9:1 :K$_2$CO$_3$in H$_2$O solution and allowed to stir at 70 °C overnight in the dark. The reaction was then brought to room temperature and extracted with dichloromethane and the combined organic layers were washed with deionized water and brine, dried over sodium sulfate, filtered and concentrated. The crude reaction mixture was then purified by column chromatography using 0% to 10% dichloromethane in hexanes as the eluent to obtain 3 as a green solid (328 mg, 75.2% yield).

^{1}H-NMR (500 MHz, CDCl$_3$, δ ppm): 9.37-9.30 (m, 8H), 8.26 (s, 2H) 8.13 (t, 3H), 7.99 (m, 6H), 7.83-7.81 (m, 3H), 7.44-7.41 (m, 3H), 7.76 (d, 1H), 7.46-7.42 (m, 2H), 1.79-1.78 (m, 8H), 1.39- 1.34 (m, 90H), 1.01-0.96 (m, 12H), 0.84-0.80 (m, 14H).

^{13}C-NMR (125 MHz, CDCl$_3$, δ ppm): 140.03, 139.87, 137.85, 137.62, 132.46, 132.38, 132.33, 131.53, 131.23, 130.96, 130.82, 130.79, 130.75, 130.63, 130.42, 130.22, 129.49, 128.70, 127.73, 126.92, 126.70, 126.36, 126.29, 126.23, 126.20, 126.15, 126.07, 125.82, 125.76, 125.53, 120.39, 118.63, 118.49, 118.29, 108.11, 108.00, 107.91, 107.64, 107.54,

104.60, 104.53, 104.28, 34.07, 32.01, 31.98, 29.55, 29.51, 29.44, 29.41, 25.00, 22.69, 18.77, 18.49, 14.15, 14.12, 12.21, 12.18.

MS (ESI): Calculated $[M]^+$: 1711.9937; Observed: 1711.9988.

4   **Pc-Phenol**
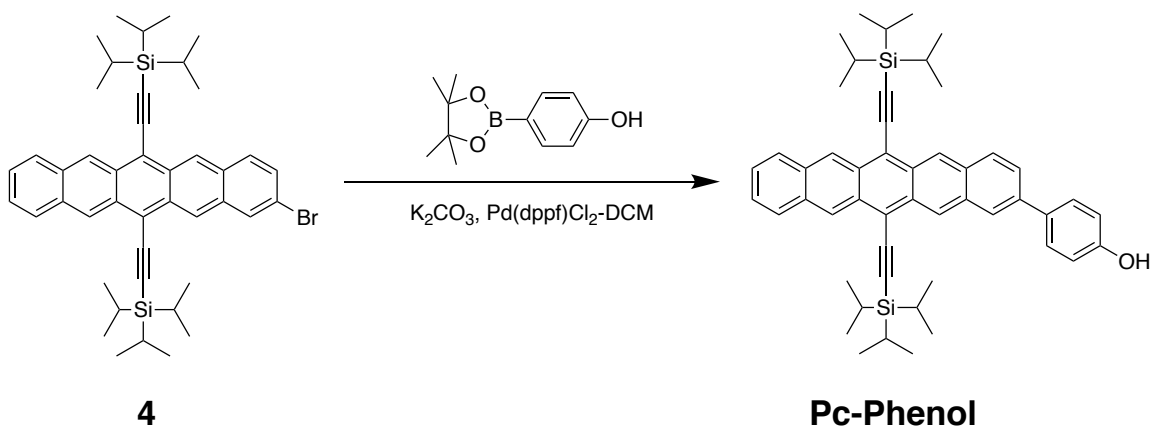
4 (300 mg, 0.42 mmol), 4-hydroxyphenylboronic acid pinacol ester (110 mg, 0.50 mmol) and Pd(dppf)Cl$_2$·DCM (17.1 mg, 0.021 mmol) were added to a reaction vial, followed by sequential vacuum and argon cycles to degas the solids. K$_2$CO$_3$ (577 mg, 4.2 mmol) was then dissolved in 1 mL H$_2$O and degassed. The solids were then dissolved in 10 mL of a mixture of 9:1 THF:K$_2$CO$_3$ in H$_2$O solution and allowed to stir at 70 °C overnight in the dark. The reaction was then brought to room temperature and extracted with dichloromethane and the combined organic layers were washed with deionized water and brine, dried over sodium sulfate, filtered and concentrated. The crude reaction mixture was then purified by column chromatography using 35% to 50% dichloromethane in hexanes as the eluent to obtain **Pc-Phenol** as a teal solid (226 mg, 74.0% yield).

^{1}H-NMR (500 MHz, CDCl$_3$, δ ppm): 9.33 (s, 4H), 8.07 (t, 2H), 8.00 (m, 2H), 7.71 (m, 3H), 7.44 (m, 2H), 7.03 (d, 2H), 4.90 (s, 1H), 1.48-1.39 (m, 42H).

^{13}C-NMR (125 MHz, CDCl3, δ ppm): 155.58, 137.93, 133.74, 132.41, 129.42, 128.83, 128.71, 126.53, 126.18, 126.15, 116.04, 19.16, 11.86.

MS (ESI): Calculated [M]$^+$: 730.4026; Observed: 730.4038.

5   **BP0-Phenol**
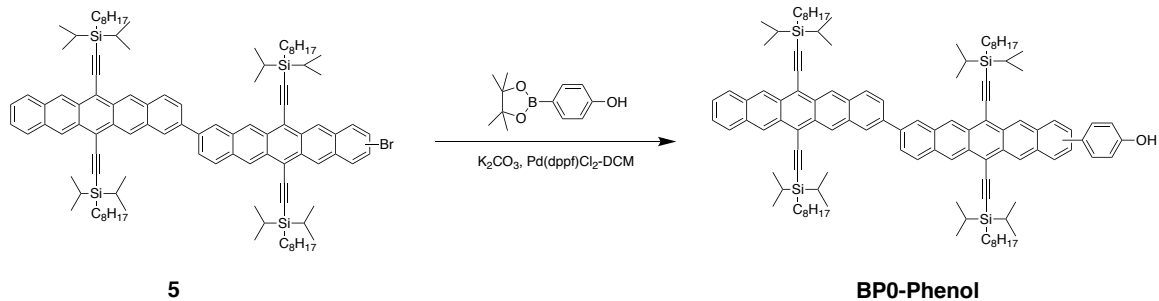
5 (100 mg, 0.06 mmol), 4-hydroxyphenylboronic acid pinacol ester (16 mg, 0.07 mmol) and Pd(dppf)Cl$_2$·DCM (2.5 mg, 0.003 mmol) were added to a reaction vial, followed by sequential vacuum and argon cycles to degas the solids. K$_2$CO$_3$ (84.3 mg, 0.61 mmol) was then dissolved in 1 mL H$_2$O and degassed. The solids were then dissolved in 10 mL of a mixture of 9:1 THF:K$_2$CO$_3$ in H$_2$O solution and allowed to stir at 70 °C overnight in the dark. The reaction was then brought to room temperature and extracted with dichloromethane and the combined organic layers were washed with deionized water and brine, dried over sodium sulfate, filtered and concentrated. The crude reaction mixture was then purified by column chromatography using 50% to 75% dichloromethane in hexanes as the eluent to obtain BP0-Phenol as a green solid (53 mg, 52.7% yield).

^{1}H-NMR (500 MHz, CDCl$_3$, δ ppm): 9.40 (s, 2H), 9.33 (m, 6H), 8.36 (s, 2H), 8.15 (d, 2H), 8.10 (s, 1H), 8.06 (d, 2H), 8.00 (m, 2H), 7.94 (m, 2H), 7.70 (m, 3H), 7.43 (m, 2H), 7.01 (d, 2H), 4.84 (s, 1H), 1.80 (m, 8H), 1.45-1.21 (m, 90H), 0.99 (m, 9H), 0.84 (m, 9H), 0.74 (m, 8H).

^{13}C-NMR (125 MHz, CDCl$_3$, δ ppm): 155.47, 137.85, 133.60, 132.36, 131.60, 130.66, 129.61, 128.70, 128.57, 126.37, 126.20, 126.06, 125.95, 124.86, 115.90, 107.55, 104.53,

34.08, 34.03, 31.98, 31.91, 29.53, 29.47, 29.39, 29.37, 25.04, 24.97, 22.66, 22.61, 18.76, 18.74, 18.48, 14.10, 14.01, 12.21, 10.50.

MS (ESI): Calculated $[M+H]^+$: 1649.0870; Observed: 1649.0900.
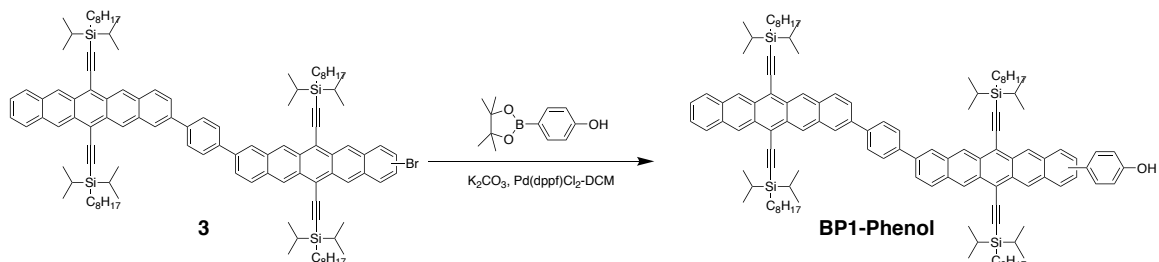
3 (325 mg, 0.2 mmol), 4-hydroxyphenylboronic acid pinacol ester (50.6 mg, 0.23 mmol) and Pd(dppf)Cl2·DCM (8.16 mg, 0.01 mmol) were added to a reaction vial, followed by sequential vacuum and argon cycles to degas the solids. K_2CO_3 (263 mg, 1.9 mmol) was then dissolved in 1 mL H_2O and degassed. The solids were then dissolved in 10 mL of a mixture of 9:1 THF:K_2CO_3 in H_2O solution and allowed to stir at 70 °C overnight in the dark. The reaction was then brought to room temperature and extracted with dichloromethane and the combined organic layers were washed with deionized water and brine, dried over sodium sulfate, filtered and concentrated. The crude reaction mixture was then purified by column chromatography using 50% dichlromethane in hexanes as the eluent to obtain **BP1- Phenol** as a green solid (121 mg, 37.0% yield).

^{1}H-NMR (400 MHz, CDCl3, δ ppm): 9.37 (s, 2H), 9.32 (d, 6H), 8.26 (s, 2H), 8.13-8.04 (m, 4H), 7.99 (m, 6H), 7.81 (d, 2H), 7.70 (m, 3H), 7.43 (m, 2H), 7.01 (d, 2H), 4.83 (s, 1H), 1.79 (m, 8H), 1.43-1.20 (m, 100H), 0.82 (m, 18H).

^{13}C-NMR (125 MHz, CDCl3, δ ppm): 155.59, 140.52, 140.13, 137.83, 133.72, 132.62, 132.52, 132.48, 131.69, 131.12, 130.91, 130.78, 129.61, 129.42, 128.84, 128.70, 127.87, 127.32, 126.82, 126.50, 126.32, 126.20, 125.95, 124.97, 118.64, 118.45, 116.03, 107.80,

107.68, 104.75, 34.23, 34.19, 32.14, 32.11, 29.67, 29.64, 29.59, 29.56, 29.53, 25.18, 25.13, 22.81, 18.91, 18.89, 18.86, 18.64, 18.62, 14.26, 14.23, 12.36, 10.65.

MS (ESI): Calculated $[M+H]^+$: 1725.1184; Observed: 1725.1183
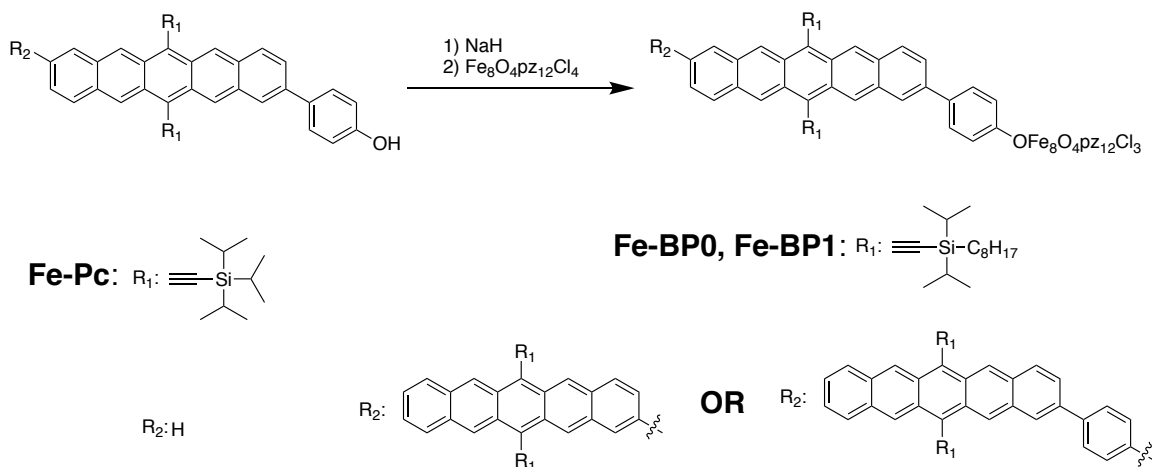
In a nitrogen-filled glovebox, $Fe_8O_4pz_{12}Cl_4$ (1 eq) was dissolved in approximately 10 mL of anhydrous THF. In a separate vial, NaH (10 eq) was suspended in THF to which Pc, BP0, or BP1 Phenol (1 eq.) was added and stirred for about 1 h, turning the suspension from dark green to dark violet. This mixture was then filtered through a syringe filter (0.2 μm PTFE) to give a dark violet solution. This solution was slowly added dropwise to the solution of $Fe_8O_4pz_{12}Cl_4$ and stirred for 16 h at room temperature. The solvent was then removed under vacuum. The residue was removed from the glovebox and purified via flash chromatography using a RediSep® Rf Reversed-phase C-18 column and gradient elution (10% to 50% dichloromethane in acetonitrile). Fractions containing the desired product were collected and concentrated to give the products as dark green solid.

NOTE: Upon reaction of the sodium salt of Pc-PhOH with $Fe_8O_4pz_{12}Cl_4$, a chloride is displaced from the cluster, substituted with a Pc-PhO-, BP0-PhO-, and BP1-PhO- , giving rise to $[Fe_8O_4]$-Pc, $[Fe_8O_4]$-BP0, and $[Fe_8O4]$-BP1, respectively. The high-spin Fe^{3+} centers of the cluster give rise to large paragmagnetic shifting and signal broadening of the resulting adducts, precluding complete characterization by NMR. However, the position of the aromatic protons of the pentacenes shifts from the usual 6-8 ppm region upon addition to the cluster. In the case of the simplest adduct, $[Fe_8O_4]$-Pc, upon treatment with anhydrous HCl, the aromatic resonances associated with the pentacene moiety return to the 6-8 ppm region, evidence that the pentacene moiety goes from being covalently linked to the cluster to the dissociated Pc-PhOH and $Fe_8O_4pz_{12}Cl_4$ molecules. Mass spectrometry of the $[Fe_8O_4]$-Pc adduct shows the molecular ion of the desired compound (m/z = 2152), as well as fragments corresponding to $Fe_8O_4pz_{12}Cl_3$ (m/z = 1420) and Pc-PhOH (m/z = 730). Taken in context of the NMR and IR data, this is used as evidence for the formation of the desired product. The larger size of $[Fe_8O_4]$-BP0 and $[Fe_8O_4]$-BP1 fragment more quickly upon ionization into the BP0/BP1 and $Fe_8O_4pz_{12}Cl_4$, but the distinct electronic absorption and IR spectra, as well as the ability to separate the material from any remaining starting material using RP-chromatography, indicate that monosubstituted adducts have formed.

Fe-Pc: (15 mg, 20% yield) MS (ESI): Calculated $[M]^+$: 2152.1179; Observed: 2152.1206;

Fe-BP0: (23 mg, 22% yield);

Fe-BP1: (18 mg, 17% yield)

4.8: References

(1) M. B. Smith, J. Michl, Singlet fission. *Chem. Rev.* **110**, 6891–6936 (2010).

(2) M. B. Smith, J. Michl, Recent advances in singlet fission. *Annu. Rev. Phys. Chem.* **64**, 361–86 (2013).

(3) R. C. Johnson, R. E. Merrifield, Effects of Magnetic Fields on the Mutual Annihilation of Triplet Excitons in Anthracene Crystals. *Phys. Rev. B*. **1**, 896–902 (1970).

(4) A. Suna, Kinematics of Exciton-Exciton Annihilation in Molecular Crystals. *Phys. Rev. B*. **1**, 1716–1739 (1970).

(5) N. Monahan, X.-Y. Zhu, Charge Transfer–Mediated Singlet Fission. *Annu. Rev. Phys. Chem.* **66**, 601–618 (2015).

(6) N. R. Monahan *et al.*, *Nat. Chem.*, in press.

(7) R. D. Pensack *et al.*, Exciton delocalization drives rapid singlet fission in nanoparticles of acene derivatives. *J. Am. Chem. Soc.* **137**, 6790–6803 (2015).

(8) R. Wang *et al.*, Magnetic dipolar interaction between correlated triplets created by singlet fission in tetracene crystals. *Nat. Commun.* **6**, 8602 (2015).

(9) P. E. Teichen, J. D. Eaves, Collective aspects of singlet fission in molecular crystals. *J. Chem. Phys.* **143**, 44118 (2015).

(10) W.-L. Chan, M. Ligges, X.-Y. Zhu, The energy barrier in singlet fission can be overcome through coherent coupling and entropic gain. *Nat. Chem.* **4**, 840–845 (2012).

(11) S. N. Sanders *et al.*, Quantitative Intramolecular Singlet Fission in Bipentacenes. *J. Am. Chem. Soc.* **137**, 8965–8972 (2015).

(12) E. Busby *et al.*, A Design Strategy for Intramolecular Singlet Fission Mediated by Charge-Transfer States in Donor-Acceptor Organic Materials. *Nat. Mater.* **14**, 426–33 (2015).

(13) E. A. Margulies *et al.*, Enabling singlet fission by controlling intramolecular charge transfer in π-stacked covalent terrylenediimide dimers. *Nat. Chem.* **8**, 1120–1125 (2016).

(14) J. Zirzlmeier *et al.*, Singlet fission in pentacene dimers. *Proc. Natl. Acad. Sci.* **112**, 5325–5330 (2015).

(15) M. T. Trinh *et al.*, Intra- to Intermolecular Singlet Fission. *J. Phys. Chem. C.* **119**, 1312–1319 (2015).

(16) N. V Korovina *et al.*, Singlet Fission in a Covalently Linked Cofacial Alkynyltetracene Dimer. *J. Am. Chem. Soc.* **136**, 617–627 (2016).

(17) E. G. Fuemmeler *et al.*, A Direct Mechanism of Ultrafast Intramolecular Singlet Fission in Pentacene Dimers. *ACS Cent. Sci.* **2**, 316–324 (2016).

(18) M. J. Y. Tayebjee *et al.*, *Nat. Phys.*, in press, doi:10.1038/NPHYS3909.

(19) G. D. Scholes, Correlated Pair States Formed by Singlet Fission and Exciton–Exciton Annihilation. *J. Phys. Chem. A.* **119**, 12699–12705 (2015).

(20) J. Koutecký, J. Paldus, Quantum chemical study of transannular interaction. I. Model of (n, n) paracyclophanes not consideing the benzene rings distortion. *Collect. Czechoslov. Chem. Commun.* **27**, 599–618 (1962).

(21) R. P. Hosteny, T. H. Dunning Jr, R. R. Gilman, A. Pipano, I. Shavitt, A binitio study of the π-electron states of trans-butadiene. *J. Chem. Phys.* **62**, 4764–4779 (1975).

(22) P. Tavan, K. Schulten, Electronic excitations in finite and infinite polyenes. *Phys. Rev. B.* **36**, 4337–4358 (1987).

(23) T. Polívka, V. Sundström, Dark excited states of carotenoids: Consensus and controversy. *Chem. Phys. Lett.* **477**, 1–11 (2009).

(24) C. C. Gradinaru *et al.*, An unusual pathway of excitation energy deactivation in carotenoids: singlet-to-triplet conversion on an ultrafast timescale in a photosynthetic antenna. *Proc. Natl. Acad. Sci. U. S. A.* **98**, 2364–2369 (2001).

(25) E. Papagiannakis, J. T. M. Kennis, I. H. M. van Stokkum, R. J. Cogdell, R. van Grondelle, An alternative carotenoid-to-bacteriochlorophyll energy transfer pathway in photosynthetic light harvesting. *Proc. Natl. Acad. Sci. U. S. A.* **99**, 6017–6022 (2002).

(26) M. R. Antognazza *et al.*, Ultrafast excited state relaxation in long-chain polyenes. *Chem. Phys.* **373**, 115–121 (2010).

(27) T. C. Berkelbach, M. S. Hybertsen, D. R. Reichman, Microscopic theory of singlet exciton fission. II. Application to pentacene dimers and the role of superexchange. *J. Chem. Phys.* **138**, 114103 (2013).

(28) X. Feng, D. Casanova, A. I. Krylov, Intra-and Intermolecular Singlet Fission in Covalently Linked Dimers. *J. Phys. Chem. C*. **120**, 19070–19077 (2016).

(29) P. B. Coto, S. Sharifzadeh, J. B. Neaton, M. Thoss, Low-Lying Electronic Excited States of Pentacene Oligomers: A Comparative Electronic Structure Study in the Context of Singlet Fission. *J. Chem. Theory Comput.* **11**, 147–156 (2015).

(30) T. Zeng, R. Hoffmann, N. Ananth, The low-lying electronic states of pentacene and their roles in singlet fission. *J. Am. Chem. Soc.* **136**, 5755–5764 (2014).

(31) K. Aryanpour, A. Shukla, S. Mazumdar, Theory of Singlet Fission in Polyenes, Acene Crystals, and Covalently Linked Acene Dimers. *J. Phys. Chem. C*. **119**, 6966–6979 (2015).

(32) X. Feng, A. V. Luzanov, A. I. Krylov, Fission of entangled Spins: An electronic structure perspective. *J. Phys. Chem. Lett.* **4**, 3845–3852 (2013).

(33) S. N. Sanders *et al.*, Singlet Fission in Polypentacene. *Chem.* **1**, 505–511 (2016).

(34) W.-L. Chan *et al.*, Observing the multiexciton state in singlet fission and ensuing ultrafast multielectron transfer. *Science.* **334**, 1541–5 (2011).

(35) S. R. Yost *et al.*, A transferable model for singlet-fission kinetics. *Nat. Chem.* **6**, 492–7 (2014).

(36) S. Lukman *et al.*, Tuneable Singlet Exciton Fission and Triplet – Triplet Annihilation in an Orthogonal Pentacene Dimer. *Adv. Funct. Mater.* **25**, 5452–5461 (2015).

(37) R. D. Pensack *et al.*, Observation of Two Triplet-Pair Intermediates in Singlet Exciton Fission. *J. Phys. Chem. Lett.* **7**, 2370–2375 (2016).

(38) D. L. Dexter, Two ideas on energy transfer phenomena: Ion-pair effects involving the OH stretching mode, and sensitization of photovoltaic cells. *J. Lumin.* **18**, 779–784 (1979).

(39) M. C. Hanna, a. J. Nozik, Solar conversion efficiency of photovoltaic and photoelectrolysis cells with carrier multiplication absorbers. *J. Appl. Phys.* **100**, 1–8 (2006).

(40) W.-L. Chan, J. R. Tritsch, X.-Y. Zhu, Harvesting singlet fission for solar energy conversion: one-versus two-electron transfer from the quantum mechanical superposition. *J. Am. Chem. Soc.* **134**, 18295–18302 (2012).

(41) J. R. Tritsch, W.-L. Chan, X. Wu, N. R. Monahan, X.-Y. Zhu, Harvesting singlet fission for solar energy conversion via triplet energy transfer. *Nat. Commun.* **4**, 2679 (2013).

(42) N. J. Thompson *et al.*, Energy harvesting of non-emissive triplet excitons in tetracene by emissive PbS nanocrystals. *Nat. Mater*. **13**, 1039–1043 (2014).

(43) M. Tabachnyk *et al.*, Resonant energy transfer of triplet excitons from pentacene to PbSe nanocrystals. *Nat. Mater.* **13**, 1033–1038 (2014).

(44) D. N. Congreve *et al.*, External quantum efficiency above 100% in a singlet-exciton-fission-based organic photovoltaic cell. *Science*. **340**, 334–7 (2013).

(45) I. Paci *et al.*, Singlet fission for dye-sensitized solar cells: Can a suitable sensitizer be found? *J. Am. Chem. Soc.* **128**, 16546–16553 (2006).

(46) A. J. Esswein, D. G. Nocera, Hydrogen production by molecular photocatalysis. *Chem. Rev.* **107**, 4022–4047 (2007).

(47) C. J. Bardeen, The structure and dynamics of molecular excitons. *Annu. Rev. Phys. Chem.* **65**, 127–48 (2014).

(48) A. Turkiewicz *et al.*, Assembling Hierarchical Cluster Solids with Atomic Precision. *J. Am. Chem. Soc.* **136**, 15873–15876 (2014).

(49) P. Baran *et al.*, Synthesis, characterization, and study of octanuclear iron-oxo clusters containing a redox-active Fe4O4-cubane core. *Inorg. Chem.* **47**, 645–655 (2008).

(50) H. Chakraborty, A. Shukla, Theory of triplet optical absorption in oligoacenes: From naphthalene to heptacene. *J. Chem. Phys.* **141**, 164301 (2014).

(51) K. Kamada *et al.*, Strong Two-Photon Absorption of Singlet Diradical Hydrocarbons. *Angew. Chemie*. **119**, 3614–3616 (2007).

(52) A. A. Bakulin *et al.*, Mode-selective vibrational modulation of charge transport in organic electronic devices. *Nat. Commun.* **6** (2015).

(53) M. de Jong, L. Seijo, A. Meijerink, F. T. Rabouw, Resolving the ambiguity in the relation between Stokes shift and Huang–Rhys parameter. *Phys. Chem. Chem. Phys.* **17**, 16959–16969 (2015).

(54) B. J. Walker, A. J. Musser, D. Beljonne, R. H. Friend, Singlet exciton fission in solution. *Nat. Chem.* **5**, 1019–24 (2013).

(55) M. M. Payne, J. H. Delcamp, S. R. Parkin, J. E. Anthony, Robust, soluble pentacene ethers. *Org. Lett.* **6**, 1609–1612 (2004).

(56) R. G. Raptis, I. P. Georgakaki, D. C. R. Hockless, A FeIII/oxo cubane contained in an octanuclear complex of T symmetry that is stable over five oxidation states. *Angew. Chemie Int. Ed.* **38**, 1632–1634 (1999).

(57) S. Janietz *et al.*, Electrochemical determination of the ionization potential and electron affinity of poly (9, 9-dioctylfluorene). *Appl. Phys. Lett.* **73**, 2453–2455 (1998).

(58) X. Y. Zhu, How to draw energy level diagrams in excitonic solar cells. *J. Phys. Chem. Lett.* **5**, 2283–2288 (2014).

(59) S. K. Lower, M. A. El-Sayed, The triplet state and molecular electronic processes in organic molecules. *Chem. Rev.* **66**, 199–241 (1966).

Chapter 5: Conductance of Oligophenylenediamines using the Scanning Tunneling Microscope-Based Break-Junction Technique

5.1: Preface

This chapter is based on a journal article published in the *Journal of the American Chemical Society* entitled "Electronically Transparent Au–N Bonds for Molecular Junctions" by Yaping Zang, Andrew Pinkard, Zhen-Fei Liu, Jeffrey B. Neaton, Michael L. Steigerwald, Xavier Roy, and Latha Venkataraman. I synthesized and characterized the compounds investigated in this study. Scanning tunneling microscope-based break-junction (STM-BJ) measurements were performed by Dr. Yaping Zhang of the Venkataraman research group and theoretical predictions were performed by Dr. Zhen-Fei.

5.2: Introduction

Chapter 4 discussed probing the chemical behavior of singlet fission chromophores using modified ligands about the $[Fe_8O_4]$-core. Chapter 5 continues examining metal-ligand behavior by probing how charge moves through polyphenylenediamine molecular wires.

The nature of charge transport across metal-organic interfaces plays a crucial role in determining the functionality of molecular scale devices.[1] Linkers that bind to metal electrodes through covalent (e.g., thiols[2]) or dative (e.g., amines[3] and thioethers[4]) bonds

are widely used to wire molecular components into circuits. Amines, which bind selectively to undercoordinated Au atoms through dative interactions, are also used to passivate nanocrystals.[5] Some of these amines, such as aniline and its derivatives, can undergo facile electrochemical oxidation, resulting in chemical reactions localized at the nitrogen atom.[6] In this work, we show that such an electrochemical process can modify charge transport across the Au–N interface. We measure the conductance of oligophenylene diamine single-molecule junctions using the scanning tunneling microscope-break junction (STM-BJ) technique.[2b] We perform these measurements in an ionic medium and show that under a high oxidizing bias, we form junctions whose electrical conductance values are significantly higher than those formed through conventional dative interactions. These measurements, coupled with density functional theory (DFT) calculations, strongly suggest that electrografting of the aniline moiety leads to the formation of a new type of Au–N bond in the junction. Importantly, these junctions show better electronic coupling than those formed with Au–S or Au–C bonds[7]. These results provide not only an unprecedented chemical route to highly transparent Au–organic interfacial contacts but also evidence for an unanticipated mode of Au–N bonding.
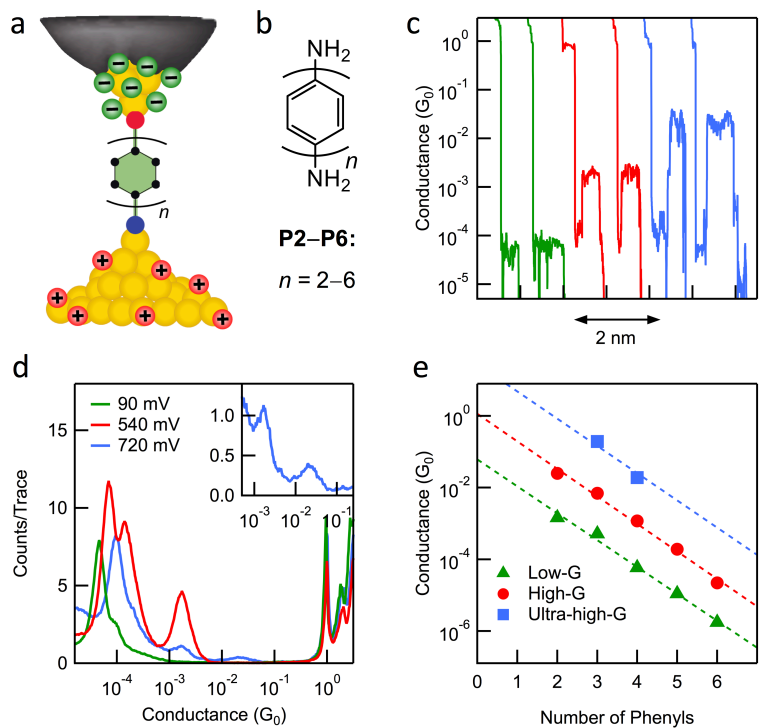
Figure 5.1. (a) Schematic of a single molecule junction created in an ionic environment showing the asymmetric double layer. (b) Molecular structures of the oligophenylene diamines P2–P6. (c) Sample conductance traces of P4 junctions at a tip bias of 90 mV (green), 540 mV (red) and 720 mV (blue). (d) Logarithm-binned 1D histograms for P4 traces at different tip bias. Inset: zoomed-in view of the High-G and Ultra-high-G peaks at 720 mV. (e) Conductance, determined from Gaussian fits to histogram peaks, as a function of the number of phenylene units. Data are acquired at constant tip bias of 90 mV for Low-G, either 360 mV or 720 mV for High-G, and 720 mV for Ultra-high-G. Dashed lines are linear fits to these data. For the Ultra-high-G data, we constrain the line to have the same conductance decay as that of the High-G data and only determine the contact conductance from the fit.

5.3: Single Molecule Conductances of P2-P6

The experimental details for the STM-BJ technique in ionic environment have been described previously.[8] Measurements are performed using an insulated STM Au tip[9] with an exposed area of ~1 μm^2 and an Au substrate with an area larger than 1 cm^2. Figure 5.1a illustrates how, under these conditions, a dense double-layer of charge builds up around the small area of the coated tip and a sparse double-layer is formed on the bottom, large-area, uncoated substrate. Using this approach, we measure the single-

97

molecule conductance of a series of oligophenylene diamines (P2–P6, shown in Figure 5.1b), in propylene carbonate (PC) with tetrabutylammonium perchlorate (TBAClO4) as the supporting electrolyte. The electrolyte concentration (0.1 M) is much higher than that of the diamine (10 µM), ensuring a large concentration of ions around the junction.

Results for p-quaterphenylene-4,4'''-diamine (P4) are presented first. Sample conductance traces are shown in Figure 5.1c. At low tip bias (90 mV), a clear conductance plateau is observed at ~5×10^{-5} G_0 (G_0 = $2e^2/h$ is the quantum of conductance); this is consistent with the formation of P4 single molecule junction with two dative Au←N contacts. When the tip bias is increased to 540 mV, we observe that 30 % of the traces show a significantly higher conductance plateau, and as the tip bias is increased further to 720 mV, an even higher conductance plateau appears. These measurements are repeated thousands of times at different tip biases. Figure 5.1d presents the one-dimensional (1D) log-binned histograms compiled for P4 without data selection at three different biases. The peaks close to integer multiples of G_0 indicate the formation of Au point contacts. The histogram of the 90 mV bias data shows a clear peak around ~5×10^{-5} G_0 (labeled as Low-G). We have previously shown that this value is characteristic of molecular junctions formed with two dative Au←N interactions.[10] A well-defined high conductance peak at ~1.7×10^{-3} G_0, labeled High-G, and another even higher conductance peak (Ultra-high-G) at ~2.1×10^{-2} G_0 emerge at 540 and 720 mV tip bias, respectively (see inset of Figure 5.1d). These two conductance peaks are respectively ~20 and ~400 times higher than the high-bias Low-G values. Note that as the tip bias is increased, the Low-G peak evolves into a double peak and shifts slightly to higher conductance. The double peak results from the formation of junctions with two

98

molecules in parallel,[11] while the conductance shift is due to a strongly energy-dependent transmission function around the Fermi energy, resulting in an increase of the junction conductance when the bias is increased.

Similar features are observed for P2–P6. The 1D histograms; all have Low-G peaks at low tip bias and High-G peaks emerging at high positive bias. As with P4, P3 exhibits an Ultra-high-G peak at 630 mV tip bias with a conductance of ~0.2 G_0. To date, these are the highest reported conductance values for oligophenylene systems, regardless of the contact group used[3,7a,12]. Figure 5.1e is a plot of the conductance value of each peak as a function of the number of phenylene units in the molecular backbone. It shows that the conductance of the Low-G and High-G series decrease exponentially with increasing molecular length. Using a linear fit to the data on a semi-logarithm scale, a decay constant of β ~1.8/phenyl is obtained for both series, indicating that the same π-conjugated oligophenylene backbone dominates transport trends.[13] Note that a similar trend is also seen for the Ultra-high-G data (with the caveat that only two data points could be measured in that case). The key result here is that the difference between the Low-G and High-G junctions arises from differences at the contacts: by extending the fit to zero phenylene units, we estimate a contact resistance which provides a metric by which to compare them. Note that the contact resistance does not give the resistance of the contact group alone as this resistance will, in principle, be limited to $1/G_0$=12.9 kΩ (assuming a single conducting channel across a junction). For the Low-G junctions, a contact resistance of 205 kΩ is obtained. By contrast, the High-G junction has a contact resistance of 11 kΩ, about 20 times lower than that of the Low-G junction; and the Ultra-

high-G has a contact resistance of 400 Ω, more than 400 times lower than that of the Low-G junction.

To further verify that both Low-G and High-G peaks stem from tunneling across the same oligophenylene backbone, Figure 5.2a compiles the two-dimensional (2D) conductance histogram of P4. At 540 mV tip bias, P4 shows Low-G and High-G conductance plateaus extending to ~0.6 nm beyond the Au point-contact rupture. Based on the molecular length of P4, the length profile of the two conductance features and previous measurements under the same solvent/electrolyte conditions, these plateau lengths indicate that both types of junctions are formed by the quaterphenylene backbone bridging across the two electrodes, and not by one of the electrodes coupling directly to the conjugated π-system, short-circuiting the linker.[14]
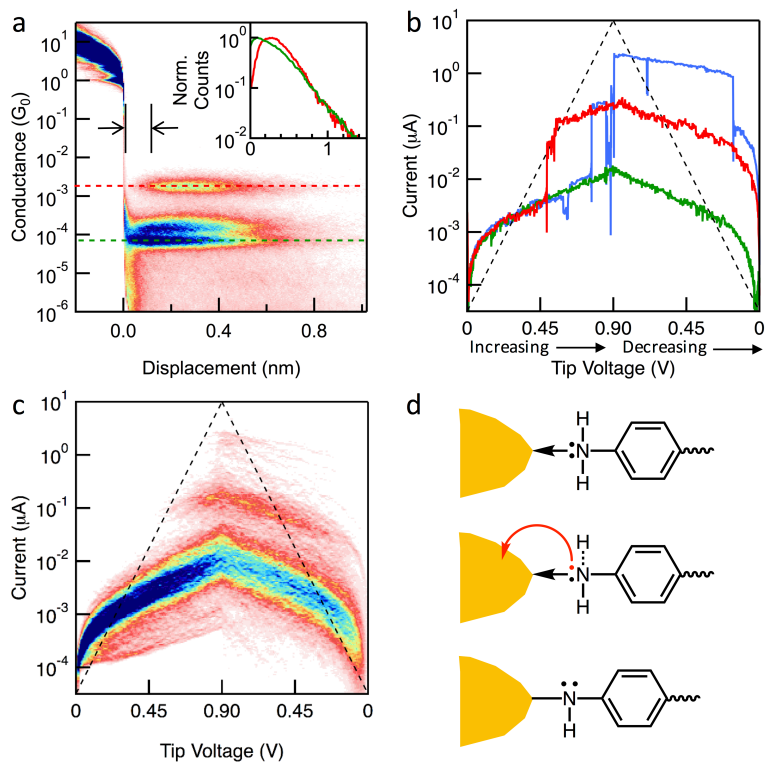
Figure 5.2. (a) 2D conductance-displacement histogram of P4 junction created by aligning and overlaying 5000 (tip bias: 540 mV). Inset: The normalized length profiles determined from the 2D histograms (along

the dashed lines) confirm that Low-G (green) and High-G (red) junctions have the same extensions. (b) Sample current-voltage (I-V) curves of P4. The dashed black line illustrates the 50 ms bias ramp. (c) 2D I-V histogram of P4 junctions, created by overlaying over 1000 I-V curves selected from 8000 (see Supporting Information). (d) Schematic illustrating the formation of the novel Au‑N contact upon oxidation of a dative Au←N bond.

The Low-G, High-G, and Ultra-high-G peaks are discrete conductance states of the molecular junction, as evidenced by current-voltage (I-V) curves shown in Figure 4.2b. Each of these curves shows the behavior of a different junction as the applied bias is changed. They are measured by first establishing and maintaining a molecular junction and thereafter sweeping the bias from 0 to 0.9 V and then back down to 0 V. At low bias, only the Low-G state is observed in all three sample curves. At ~0.5 V tip bias, the well-separated High-G state appears in one of the sample I-V curves (red). The transition between these states occurs within the data acquisition time step of 25 μs. Once formed, the High-G state endures even as the bias is decreased down to 0 V. A third trace (blue) shows a transition first to the High-G state and then to the Ultra-high-G state. This latter state demonstrates a current exceeding 1 μA across the single-molecule junction. Figure 2c shows a 2D overlay of over 1000 I-V curves of P4 junctions. Not all junctions switch from a Low-G to a High-G state, and not all High-G junctions can endure the full bias ramp. These I-V data clearly establish that the High-G and Ultra-high-G state are not accessed through a simple off-resonance/in-resonance mechanism whereby a resonant conductance level is gradually approached as we vary the tip bias.

5.4: Origins of "High-G" State

The use of the primary aromatic amine linker appears to be necessary for the emergence of the High-G state. It has been shown in a number of systems[11] that under a high positive tip bias, molecules that do not contain such amine groups only exhibit Low-

G peaks that are consistent with dative contacts. To test this assertion, we synthesized and measured the single molecule conductance of an asymmetrical terphenylene analog with one pyridyl group that can bind to Au through dative interaction and one amine group (P2Py). The 1D and 2D histograms show that P2Py forms High-G junctions (though it does not form Ultra-high-G junctions), suggesting that the higher-conducting state is accessed through a reaction of the primary aromatic amine at one of the electrodes, presumably at the tip.

We emphasize that the High-G state is accessed only at a high positive tip bias, as the High-G peak is not visible at negative and positive biases below ~300 mV. It has been previously shown that ferrocene can be oxidized at the STM tip at a positive bias as a result of the dense double layer of negative ions that forms around the tip under these conditions8. The 2D histograms in Figure 5.2a suggest that an oxidation process is at play as we note a ~0.1 nm gap between the rupture of the Au point-contact and the formation of the High-G junctions. This gap suggests that a build-up of the double layer is necessary to create this state.

A mechanistic scheme that rationalizes these results must accommodate these observations: (1) The High-G state forms under oxidizing positive tip biases. (2) The Ultra-high-G state forms under higher tip biases but not for P2Py (3) The conductance decay for all three conducting states is the same and (4) These states are only seen when a double-layer is present around the tip. We posit that as the applied bias increases an electron is removed from the N lone-pair, and the protonated amido-complex so formed then loses a proton. Thus a primary aromatic amine, which initially forms a dative Au←N bond to an under-coordinated Au atom, is converted to a highly conducting Au–N

bond upon loss of an electron and a proton from the N lone pair (see Figure 5.2d). (Conversion of both dative Au←N contacts enables the Ultra-high-G state.) This proposal, while speculative, accounts for all of our experimental observations.

Such an oxidation of the dative bond would generate a local positive charge which would most likely settle on the polar N–H bond. In polar medium, this acidic proton would dissociate from the N, at least in the sense of an acid-base equilibrium. In support of this hypothesis, we note the rich literature on the catalytic oxidative dehydrogenation of amines on Au, and on the spontaneous and electrochemical grafting of primary amines to surfaces.[6a,15] In most cases, under-coordinated Au atoms and/or adsorbed oxygen on the surface are implicated in the formation of covalently anchored amine species under oxidizing conditions. Our data indicate that the new Au–N bond forms when a small gap between the tip and the substrate is opened. For the shorter P3 and P4, it is possible that the amines on both ends of the molecule become electrografted as a result of the strong electric field. In light of past works, this transport data provides the first example of an in situ amine–Au grafting reaction triggered by the oxidizing electrochemical potential within the junction.

The electrochemically induced grafting of an amine to an Au surface (presented in Figure 5.2d) is analogous to the formation of thiolate-based self-assembled monolayers on Au[6a,15a,15b,15f,16]. In support of this hypothesis, DFT-based transport calculations of the P4 single-molecule junctions were performed that support this assertion. The Low-G junction is modeled with two dative Au←N contacts in which N is a primary aromatic amine NH_2R. The High-G and Ultra-high-G junctions are modeled by respectively

replacing one and both Au←N bonds with the new Au‑N contact in which one H atom has been removed from N (with the N having an NHR form) as shown in Figure 5.3a.

The Au←N contact is a donor-acceptor (dative) bond between the N sp^3-like lone pair orbital and the conduction band of the Au electrode. The computed optimized Au← N bond length is 2.35 Å. Upon oxidation, the resulting Au‑N bond takes on more p character, shortening the bond to 2.14 Å and increasing the coupling to the π-system of the aryl backbone. The nitrogen lone-pair, which remains after the loss of the proton, is computed to exhibit greater s character and deepens in energy relative to the Fermi energy (E$_F$).
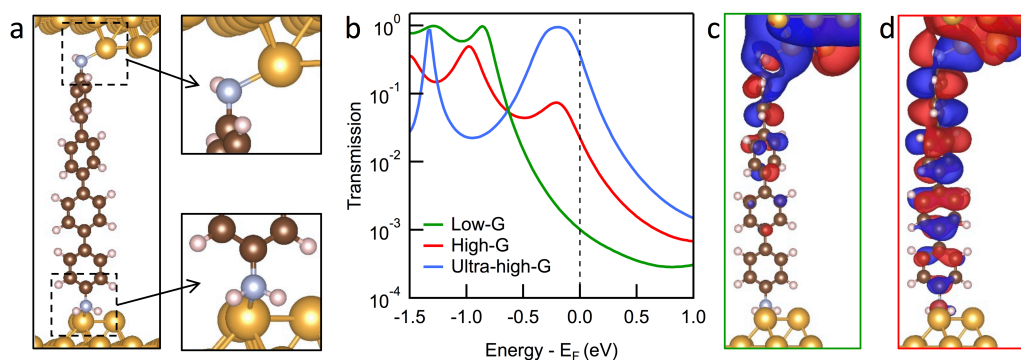
Figure 5.3. (a) Junction structure used to compute the transmission function for the High-G P4 junction. (b) Transmission functions for all three types of P4 junctions. (c,d) Calculated scattering state at the Fermi energy for Low-G (c) and High-G (d) P4 junctions. The scattering state across the Au‑N contact exhibits a much slower decay than that across the Au←N contact.

Figure 5.3b presents the calculated transmissions as a function of energy relative to E$_F$ for all three types of P4 junctions. The transmission functions for the High-G and Ultra-high-G junctions have two peaks between -1.5 and 1.0 eV. The lower energy peak arises from the HOMO-1 and it shifts towards the E$_F$ as the molecular backbone increases in length. The peak close to EF arises from the partially occupied HOMO of the

molecule. This peak is pinned at -0.2 eV, regardless of the molecular backbone length. It does not reach unit transmission in the case of the High-G junction because of the asymmetric electronic coupling at the contacts. By contrast, the transmission function for the Low-G junction does not have a peak close to E_F. The transmission functions at E_F for the computed High-G and Ultra-high-G junctions are respectively ~22 and ~360 times larger than that for the Low-G junction, a trend in excellent agreement with experimental results. Figure 5.3c and 5.3d show isosurface plots of the transmitting scattering state at Fermi for the High-G and low-G P4 junctions. Along the backbone, the scattering state resembles the π-based HOMO for both junctions. The scattering state of the High-G junction decays much more slowly across the length of the backbone than that of the Low-G junction, providing further evidence for a strong electronic coupling.

The transmission functions of the High-G and Ultra-high-G junctions are dominated by the peak pinned close to E_F.[7b] The implication is that these states should be much less susceptible to electrochemical gating than the Low-G peak. To gain further insight, a dipole layer is added to one side of the computed P4 junctions[8] (Figure 5.4a and 5.4b). The resonance energy for the symmetric dative junction shifts by ~0.3 eV, altering the Low-G conductance. By contrast, the dipole layer has almost no effect on the position of the peak close to E_F. This prediction is confirmed by the experiment shown in Figure 5.4c, which compares the 1D conductance histograms of P4 measured in different ionic environments.[11] Similar High-G and Low-G features are observed but the Low-G peak position shifts depending on the electrolyte while the High-G conductance values are essentially unchanged.
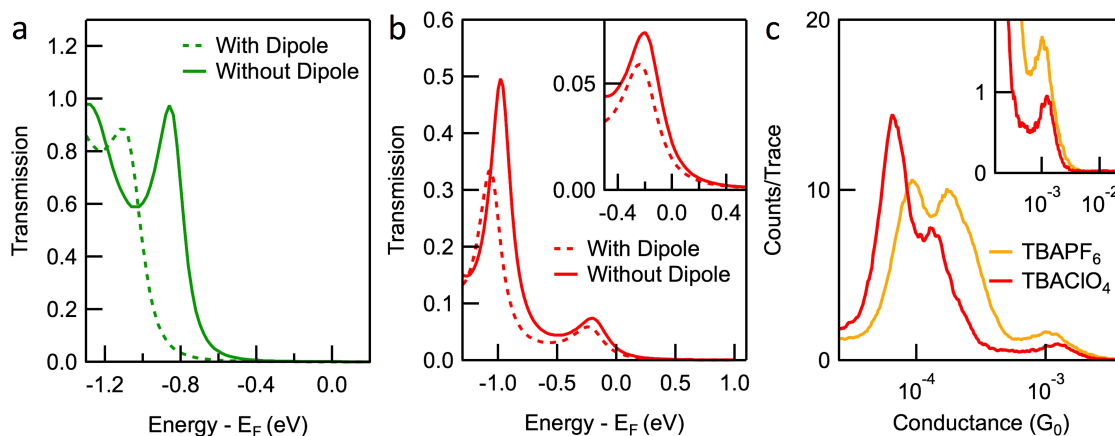
Figure 5.4. (a) Calculated transmission function for Low-G P4 junction with (dashed-green) and without (solid green) a dipole layer. (b) Transmission function for the High-G P4 junction with (dashed-red) and without (solid-red) a dipole layer. Inset: Zoomed-in view of the peak close to E_F. (c) Logarithm-binned 1D histograms of P4 in PC with TBAClO$_4$ (red) and TBAPF$_6$ (yellow) as the supporting electrolytes. Data taken at 360 mV tip bias. Inset: Zoomed-in view of the High-G peak region.

5.5: Conclusion and Outlook

By creating molecular junctions in an ionic oxidizing environment using primary aniline-like linkers, record low-contact resistance in single-molecule devices were achieved, the lowest contact resistance observed through phenylene backbones to date. Based on the synthetic accessibility of such amines and the simplicity of our experimental setup, this approach charts a clear path to designing and building junctions with transparent metal-organic interfaces for electron transfer. Such devices could enable the study of whole new families of molecular phenomena whose transport signatures are at the moment obscured by the resistivity of the contacts.

5.6 Synthesis

The molecules measured in this chapter were prepared using simple Suzuki coupling chemistry, followed by deprotection of the BOC (*tert*-butyloxycarbonyl) protecting group. P2 and P3 are commercially available, and P4, P5, and P6 were

106

prepared by using the appropriate dibromopolyphenyl, **1** (P4: n=0, P5: n=1, P6: n=2) and appropriate coupling reagents. The synthesis of P5 is described as an example below.
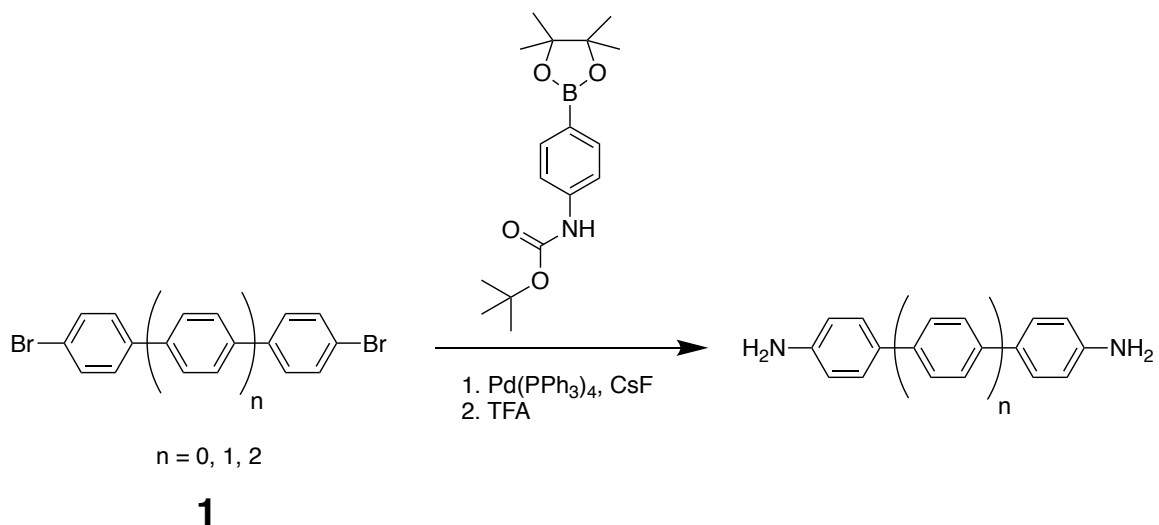
Synthesis of **P5**:

4,4'-Dibromoterphenyl (0.500 g, 1.29 mmol), 4-(N-BOC-amino)phenylboronic acid pinacol ester (0.864 g, 2.71 mmol), cesium fluoride (0.783 g, 5.15 mmol), tetrakis(triphenylphosphine)palladium(0) (0.075 g, 5 mol %) were combined in a pressure vessel with a teflon screw-cap and gently purged with nitrogen. Anhydrous THF (40 mL) was added, the vessel was sealed and stirred at 80 °C for 16 h. The mixture was cooled to room temperature and the resulting solid was collected by filtration. The solid was washed with water, followed by THF. The solid was then suspended in dichloromethane and cooled to 0 °C to which 12 mL of trifluoroacetic acid was added. The reaction was warmed to room temperature and stirred for 16 h. The reaction was filtered and basified by the addition of 3.2 g of NaOH in 100 mL of water. The resulting solid was washed with dichloromethane, water, and acetone to give the desired product as an off-white solid (0.070 g, 13% yield).

^{1}H NMR (300 MHz, DMSO-d$_6$, 25 °C) δ = 4.00 (br), 6.85 (s, 4 H), 7.68 (m, 16 H). HRMS calculated for C30H25N2$^+$ [M+H]$^+$ 413.2018, observed 413.2016 [M+H]$^+$.

P6:

The desired product was obtained as a tan solid (0.095g, 20% yield). Insolubility of the compound precluded ^{1}H NMR characterization. HRMS calculated for C36H28N2$^+$ [M+H]$^+$ 489.2331, observed 489.2332 [M+H]$^+$.

Synthesis of **P2Py**:
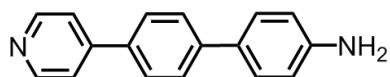
P2Py

P2Py was synthesized by first preparing *tert*-butyl(4'-bromo-[1,1'-biphenyl]-4-yl)carbamate from an adapted literature procedure.[17] 1,4-dibromobenzene (3.70 g, 3.68 mmol), 4-(*N*-BOC-amino)phenylboronic acid pinacol ester (1.00 g, 3.14 mmol), cesium carbonate (2.04 g, 6.26 mmol), and tetrakis(triphenylphosphine)palladium(0) (0.362 g, 10 mol %) were combined in Schlenk flask and placed under nitrogen. Toluene (20 mL) and Argon-sparged deionized water (40 mL) were added to the mixture. The reaction was refluxed for 72 h and then cooled to room temperature. The phases were separated in a separatory funnel and the organic layer was extracted with ethyl acetate, dried with MgSO$_4$ and concentrated. The residue was purified by silica gel chromatography (gradient of 0 to 70 % dichloromethane in hexanes). The solvents were removed *in vacuo* to give the desired product, *tert*-butyl(4'-bromo-[1,1'-biphenyl]-4-yl)carbamate, as a white, fluffy solid (0.864 g, 80% yield).^{1}H NMR (300 MHz, DMSO-d$_6$, 25 °C) δ = 1.48 (s, 9 H), 7.62 (m, 12 H), 9.43 (s, 1 H).

tert-Butyl(4'-bromo-[1,1'-biphenyl]-4-yl)carbamate (0.475 g, 1.36 mmol), 4-(Boc-amino)pyridine (0.308 g, 1.59 mmol), cesium fluoride (0.414 g, 2.73 mmol), and tetrakis(triphenylphosphine)palladium(0) (0.089 g, 5 mol %) were combined in a Schlenk flask and purged with nitrogen. The flask was sealed under nitrogen and 100 mL of anhydrous THF was added. The reaction was refluxed for 16 h, and then cooled to room temperature. The solvent was removed in vacuo and the resulting solid was washed with water and dichloromethane and suspended in dichloromethane. The mixture was cooled to 0 °C to which 12 mL of trifluoroacetic was added. The reaction was stirred for 16 h and basified by the addition of 2.0 M NaOH. The product was filtered and washed with dichloromethane, followed by water and dried under high vacuum to give an off-white solid (0.086 g, 26% yield). ^{1}H NMR (300 MHz, DMSO-d$_6$, 25 °C) δ = 5.26 (s, 2 H), 6.66 (m, 2 H), 7.51 (m, 2 H), 7.70 (m, 4 H), 7.81 (m, 2 H), 8.61 (m, 2 H). HRMS calculated for C17H14N2$^+$ [M+H]$^+$ 247.1238, observed 247.1235 [M+H]$^+$.

5.7: References

(1) (a) Ratner, M. *Nat. Nanotechnol.* **2013**, *8*, 378; (b) Perrin, M. L.; Burzurí, E.; van der Zant, H. S. *Chem. Soc. Rev.* **2015**, *44*, 902; (c) Su, T. A.; Neupane, M.; Steigerwald, M. L.; Venkataraman, L.; Nuckolls, C. *Nature Reviews Materials* **2016**, *1*, 16002.

(2) (a) Reed, M. A.; Zhou, C.; Muller, C. J.; Burgin, T. P.; Tour, J. M. *Science* **1997**, *278*, 252; (b) Xu, B. Q.; Tao, N. J. *Science* **2003**, *301*, 1221.

(3) Venkataraman, L.; Klare, J. E.; Nuckolls, C.; Hybertsen, M. S.; Steigerwald, M. L. *Nature* **2006**, *442*, 904.

(4) Park, Y. S.; Whalley, A. C.; Kamenetska, M.; Steigerwald, M. L.; Hybertsen, M. S.; Nuckolls, C.; Venkataraman, L. *J. Am. Chem. Soc.* **2007**, *129*, 15768.

(5) (a) Harun, M. K.; Lyon, S. B.; Marsh, J. *Prog. Org. Coat.* **2005**, *52*, 246; (b) Leff, D. V.; Brandt, L.; Heath, J. R. *Langmuir* **1996**, *12*, 4723.

(6) (a) Adenier, A.; Chehimi, M. M.; Gallardo, I.; Pinson, J.; Vila, N. *Langmuir* **2004**, *20*, 8243; (b) Grirrane, A.; Corma, A.; García, H. *Science* **2008**, *322*, 1661.

(7) (a) Mishchenko, A.; Vonlanthen, D.; Meded, V.; Burkle, M.; Li, C.; Pobelov, I. V.; Bagrets, A.; Viljas, J. K.; Pauly, F.; Evers, F.; Mayor, M.; Wandlowski, T. *Nano Lett.* **2010**, *10*, 156; (b) Chen, W.; Widawsky, J. R.; Vázquez, H.; Schneebeli, S. T.; Hybertsen, M. S.; Breslow, R.; Venkataraman, L. *J. Am. Chem. Soc.* **2011**, *133*, 17160.

(8) Capozzi, B.; Xia, J.; Adak, O.; Dell, E. J.; Liu, Z.-F.; Taylor, J. C.; Neaton, J. B.; Campos, L. M.; Venkataraman, L. *Nat. Nanotechnol.* **2015**, *10*, 522.

(9) Nagahara, L. A.; Thundat, T.; Lindsay, S. M. *Rev. Sci. Instrum.* **1989**, *60*, 3128.

(10) (a) Venkataraman, L.; Klare, J. E.; Tam, I. W.; Nuckolls, C.; Hybertsen, M. S.; Steigerwald, M. L. *Nano Lett.* **2006**, *6*, 458 ; (b) Quek, S. Y.; Choi, H. J.; Louie, S. G.; Neaton, J. B. *Nano Lett.* **2009**, *9*, 3949.

(11) Capozzi, B.; Low, J. Z.; Xia, J. L.; Liu, Z. F.; Neaton, J. B.; Campos, L. M.; Venkataraman, L. *Nano Lett.* **2016**, *16*, 3949.

(12) Martin, C. A.; Ding, D.; Sorensen, J. K.; Bjornholm, T.; van Ruitenbeek, J. M.; van der Zantt, H. S. J. *J. Am. Chem. Soc.* **2008**, *130*, 13198.

(13) Hsu, L. Y.; Rabitz, H. *J Chem Phys* **2016**, *145*, 234702.

(14) Meisner, J. S.; Kamenetska, M.; Krikorian, M.; Steigerwald, M. L.; Venkataraman, L.; Nuckolls, C. *Nano Lett.* **2011**, *11*, 1575.

(15) (a) Belanger, D.; Pinson, J. *Chem. Soc. Rev.* **2011**, *40*, 3995; (b) Gallardo, I.; Pinson, J.; Vila, N. *J. Phys. Chem. B* **2006**, *110*, 19521; (c) Gong, J.; Yan, T.; Mullins, C. B.

Chem. Commun. **2009**, 761; (d) Angelici, R. J. *Catal. Sci. Technol.* **2013**, *3*, 279; (e) Xu,

B.; Friend, C. M.; Madix, R. J. *Farad. Discuss.* **2011**, *152*, 241; (f) Xu, B.; Zhou, L.;

Madix, R. J.; Friend, C. M. *Angew. Chem. Int. Ed.* **2010**, *49*, 394.

(16) Green, M. L. H. *J. Organomet. Chem.* **1995**, *500* 127.

(17) Sánchez-Molina, M., López-Romero, J. M., Hierrezuelo-León, J., Martín-Rufián, M.

Díaz, A., Valpuesta, M.& Contreras-Cáceres, R. *Asian J. Org. Chem.* **2016,** *5,* 550.

Chapter 6: Microporous Cobalt Chalcogenide Battery Electrodes Prepared from Superatomic Inorganic Clusters

6.1: Preface

This chapter is based on a manuscript in publication authored by Andrew Pinkard, Boyu Qie, Alexander Aydt, Yuan Yang, and Xavier Roy. I performed the synthesis of the material, as well as battery preparation and interpretation of the results with Boyu Qie.

6.2: Introduction

Cobalt chalcogenides have attracted considerable attention due to their rich structural chemistry[1] and their potential use for hydrodesulfurization,[1,2] electrocatalysis,[3,4] dye-sensitized solar cells,[5,6] supercapacitors,[7,8,9] and battery[10-14] applications. While a variety of cobalt chalcogenide polymorphs can be prepared using bulk synthesis techniques (e.g., solid state,[15] solution phase,[13] and solvothermal reactions[16]), there is a sustained interest in creating nanostructures and/or amorphous compounds whose performances can rival and even surpass their bulk crystalline counterparts due to unique structures, morphologies, quantum confinement effects, and surface properties.[17]

Here we report a new family of microporous cobalt chalcogenide microparticles synthesized from molecular cluster precursors, and on their performances as battery electrode materials. Metal chalcogenide molecular clusters have recently been deployed as superatomic building blocks to assemble functional materials[18,19] and have previously been shown to convert to bulk crystalline solids when their passivating ligands are

112

removed via thermolysis.[20,21] In this work, we develop a new solution-phase chemical approach to remove the capping ligands from the molecular clusters $Co_6S_8(PEt_3)_6$ and $Co_6Se_8(PEt_3)_6$ using elemental S or Se as phosphine scavenger. The resulting amorphous cobalt chalcogenide microspheres, designated **MS-CoS** and **MS-CoSe**, have high surface areas and robust electrochemical properties, a combination of properties that is particularly attractive for battery applications. Among several cluster-derived materials we prepare for comparison, we find that **MS-CoS** performs well as a Li-ion battery electrode material featuring a high specific capacity of ~600 mAh/g, good cycle life, and excellent performance under high current rates. We find that replacing sulfur with selenium modifies the electrochemical properties of the material; **MS-CoSe** performs best for Na-ion battery applications, with a specific capacity comparable to **MS-CoS** (~550 mAh/g) and excellent cycling performance (81% retention after 100 cycles). These results establish metal chalcogenide molecular clusters as powerful precursors for creating new, tunable energy storage materials.

6.3 Microporous Cobalt Chalcogenides from Molecular Cluster Precursors

Figure 6.1 illustrates the synthesis of **MS-CoS** and **MS-CoSe** starting from the parent molecular cluster. The syntheses of the cluster precursors $Co_6S_8(PEt_3)_6$ and $Co_6Se_8(PEt_3)_6$ from $Co_2(CO)_8$, PEt_3, and S or Se are detailed in the Supporting Information. To dissociate PEt_3 from the Co_6E_8 core (E = S, Se), we combine the molecular cluster with six equivalents of E in toluene and heat the suspension to 150 °C in a thick-walled pressure vessel sealed under N_2. A black solid, **MS-CoS** or **MS-CoSe**, precipitates after 24 h and is collected in an inert atmosphere by filtration and dried under

vacuum. The key concept is that the phosphine ligands are somewhat labile at high temperatures in solution and upon dissociation from the core, they become kinetically trapped as Et$_3$P=E, which can be identified by ^{1}H and ^{31}P NMR in the filtrate of the reaction mixture (see SI). We propose that upon ligand dissociation, the naked cluster cores fuse together through Co–E (E= S or Se) linkages to form an extended structure. Champsaur et al. recently reported a related fusion reaction in a model Co$_6$Se$_8$ cluster.[22]
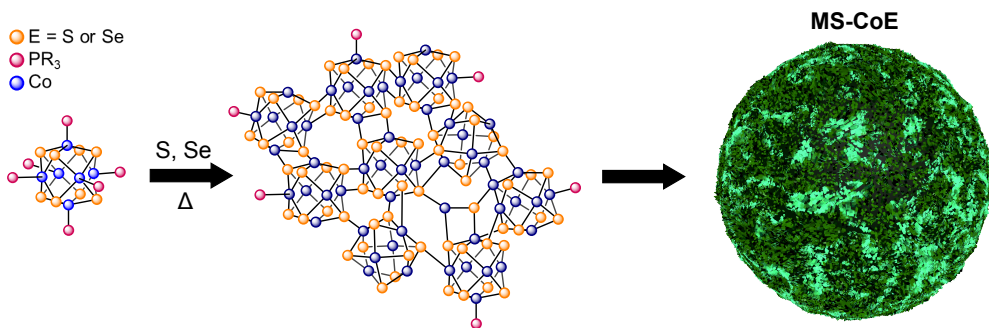
Figure 6.1. Schematic illustrating cluster-based synthesis of CoE-MS. Elemental S or Se acts as a phospine scavenger allowing for cluster cores to bridge via chalcogenide bridging. The resulting materials are amorphous and highly porous.

Powder x-ray diffraction (PXRD) measurements show that **MS-CoS** is essentially amorphous (see SI), suggesting that the clusters are either linked into a disordered network or that their internal structure breaks down during the polymerization. Remarkably, scanning electron microscopy (SEM) reveals that **MS-CoS** consists of microscopic spheres of cobalt sulfide with diameters typically on the order of 1 to 5 μm (Figure 6.2). Energy dispersive x-ray (EDX) spectroscopy establishes the composition of the solid as CoS$_{1.1}$, with a small fraction of P arising from leftover PEt$_3$ ($\sim$ 3%) (Table S1 EDX). A similar reaction using Co$_6$Se$_8$(PEt$_3$)$_6$ as the precursor and Se as the phosphine scavenger produces **MS-CoSe**. Analogous to **MS-CoS**, this solid consists of amorphous

cobalt selenide microspheres with typical diameters in the range 0.5–1 μm (Figure 6.2) and elemental composition $CoSe_{1.2}P_{0.07}$.
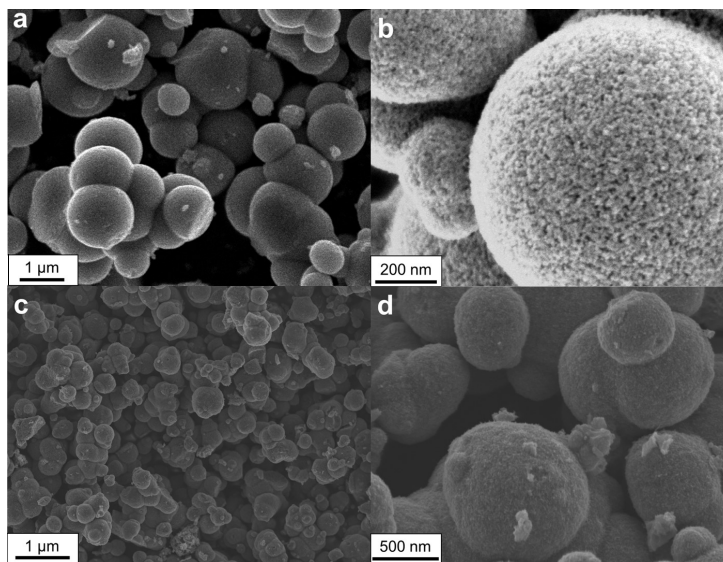
Figure 6.2. SEM images of **MS-CoS** and **MS-CoSe**. (a) low magnification of **MS-CoS**, (b) is high magnification of **MS-CoS**, (c) is low magnification of **MS-CoSe** and d) is high magnification of **MS-CoSe**.

The high magnification SEM images of the microspheres shown in Figure 6.2b and 2b hint at a porous structure. N_2 adsorption isotherm measurements and Brunauer–Emmett–Teller (BET) analysis confirm this key observation: the N_2 isotherms for **MS-CoS** and **MS-CoSe** show H3- and H4-type hysteresis loops associated with microporous or mesoporous structures.[23] **MS-CoS** and **MS-CoSe** have specific surface areas of ~360 and ~130 m^2/g, respectively, and average pore diameter of ~1.7 nm, as estimated by Barrett-Joyner-Halenda (BJH) analysis.

With their porous structure and spherical morphology, **MS-CoS** and **MS-CoSe** differ significantly from other cobalt chalcogenide materials. To illustrate this, we prepared a series of materials by heating pristine microcrystalline powders of $Co_6S_8(PEt_3)_6$ and $Co_6Se_8(PEt_3)_6$ in a sealed tube to dissociate PEt_3. The SEM images of the resulting materials reveal that the thermolysis approach produces submicron irregular

115

particles, much different than those observed for **MS-CoS and MS-CoSe**. As additional comparison materials, we annealed **MS-CoS** and **MS-CoSe** to 400 °C for 4 h. In these cases, the microsphere morphology is maintained but the internal surface area of **control-1** and **control-2** is dramatically decreased to 19 and 7 m^2/g, respectively. The N_2 isotherms show essentially no hysteresis, consistent with non-porous structures. The final composition of **control-1** and **control-2** is $CoS_{1.1}P_{0.01}$ and $CoSe_{1.1}P_{0.01}$, respectively. Note that the crystallinity of these compounds is only slightly improved by the annealing process.

6.4 Electrochemical and Battery Performance

The combination of microspherical morphology, microporosity and amorphous structure impart **MS-CoS** and **MS-CoSe** with unique electrochemical properties. To explore these properties, we fabricated working electrodes by depositing a slurry of the materials, carbon black, and polytetrafluoroethylene onto Al substrates. All electrochemical analyses are performed in coin cells with Li/Li^+ or Na/Na^+ counter electrodes (details of the working electrode and cell fabrication are contained in the SI). We find that **MS-CoS** and **MS-CoSe** work best as Li- and Na-ion battery electrode materials, respectively. Highlighting these findings, Figure 6.3 presents the cyclic voltammetry (CV) characterization and galvanostatic voltage profiles of both materials. At scan rates of 0.2 mV/s, the voltammogram shows two redox couples: one couple at 1.5 / 2.3 V and the other at 1.2 /2.0 V vs. Li^+/Li (Figure 6.3a). Consistent with previous report on CoS,[24] the voltammogram suggests a two-step conversion reaction: $CoS_x + Li^+$ $+ e^- \rightarrow Co + x\ Li_2S$. The shift of the cathodic peak from 1.5 to 1.7 V after the first cycle originates from an activation process and implies that less overpotential is needed for

subsequent cycles. The narrow peak widths indicate fast ion transport through the microporous material and the process appears to be quasi-reversible. The main features observed in the voltammogram are also reflected in the galvanostatic charge and discharge profiles (Figure 6.3b): for the **MS-CoS**/Li cell, two plateaus are observed at 1.7 and 1.4 V at a current density of 200 mA/g, corresponding to the two cathodic peaks at 1.7 and 1.2 V in the cyclic voltammogram.

Electroactive materials for Na-ion batteries are much less common than those for Li-ion.[ref] In this context, the electrochemical properties of the **MS-CoSe**/Na cell presented in Figure 6.3d-f are particularly exciting. The cyclic voltammogram reveals that the main cathodic and anodic peaks, respectively at 1.0 V and 1.5 V vs. Na/Na$^+$, are essentially unchanged after cycling, indicating a reversible reaction. A new peak at 0.6 V vs. Na$^+$/Na, which gradually grows in with each cycle, suggests that the structure of the material is changing (potentially forming polyselenides). The galvanostatic voltage profile of **MS-CoSe** measured at a current density of 200 mA/g reflects the voltammogram features (Figure 6.3e). During discharge, after a short plateau at 1.8 V, the voltage quickly drops down to 1.2 V, at which point a second, longer plateau occurs between 1.2 V and 1 V. This plateau corresponds to the major peak at 1.0 V in the cyclic voltammogram. Upon cycling, an additional plateau gradually appears at 0.7 V, which is consistent with the peak growing in at 0.6 V in the CV.
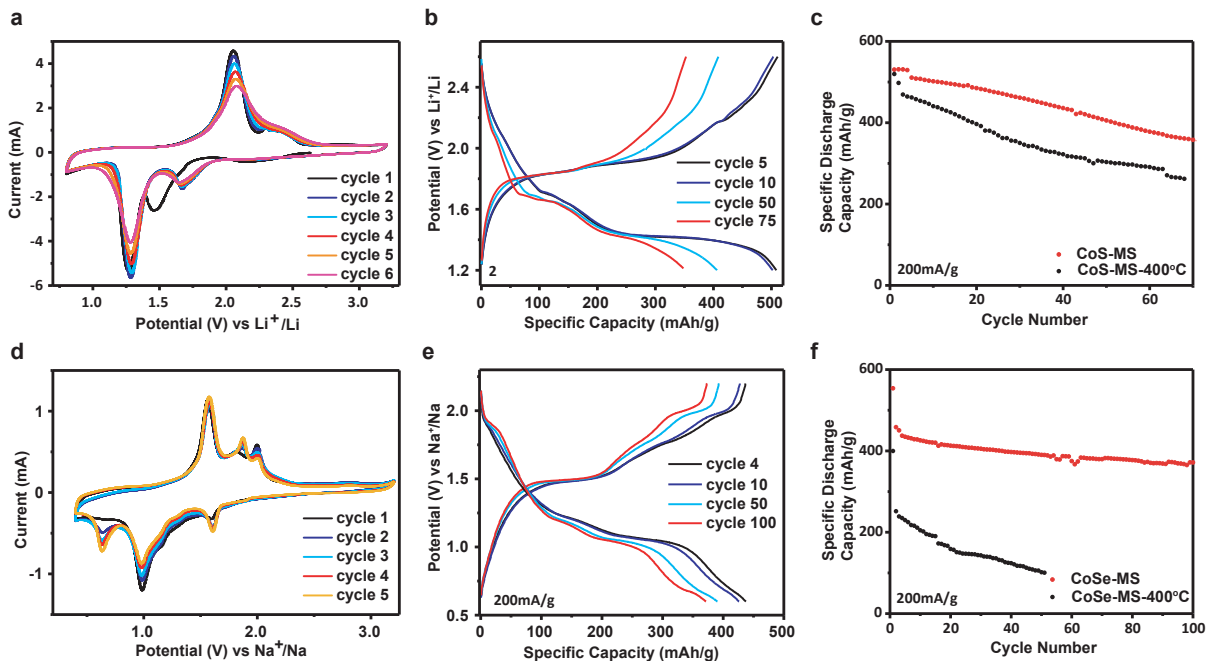
Figure 6.3. Electrochemical characterizations of **MS-CoS**/Li and **MS-CoSe**/Na half-cells. (a) cyclic voltammetry of **MS-CoS** vs. Li metal in 1 M LiTFSI (TFSI = bis(trifluoromethylsulfonyl)amine) in DOL (dioxolane) (b) galvanostatic charge and discharge profiles of **MS-CoS**. The electrode is charged/discharged at 50 mA/g for the first four cycles and 200 mA/g for the rest. (c) cycling performance of **MS-CoS**/Li half-cell and **MS-CoS**-400°C/Li half-cell. The testing conditions are the same as (b). (d) cyclic voltammetry of **MS-CoSe** vs. Na/Na$^+$ in 1 M NaPF$_6$ in 1:1 DOL:DME (DME = dimethoxyethane) (e) galvanostatic charge and discharge profiles of **MS-CoSe** at 50 mA/g for the first three cycles and followed by 200 mA/g for the rest. (f) cycle stability of **MS-CoSe**/Na and **MS-CoSe**-400°C/Na half-cells. The testing condition is the same as (e).

To gain further insight into the electrochemical properties of **MS-CoS** and **MS-CoSe**, we performed galvanostatic cycling experiments, and compared the performances of these nanomaterials with those of the annealed control samples (Figure 6.3c,f). Overall, these measurements confirm the higher capacity and significantly better cycling stability of the microporous **MS-CoS** and **MS-CoSe**. We hypothesize that the porous structure helps relieve strain inside the materials and leads to stable cycling.

At a current density of 50 mA/g, the **MS-CoS**/Li cell shows an initial capacity of 531 mAh/g. When the current density is increased to 200 mA/g after four cycles, the capacity is 510 mAh/g; it remains at ~360 mAh/g after 70 cycles at 200 mA/g, for a capacity

retention of 71% (Figure 6.3c). While the exact root of this capacity loss remains unknown, we note that it is mainly due to the shortening of the plateau at 1.4 V. One likely cause is the conversion reaction between the material and Li^+ ions. Because **MS-CoS** is amorphous, however, diffraction experiments are unable to detect these structural changes. SEM confirms that the morphology of the electrode material is essentially unchanged after cycling, indicating that the microporous structure allows the structure to relase the strains created by the conversion reaction and prevents the spherical particles from breaking apart.

A very different behavior is observed wit the annealed, non-porous **MS-CoS**: the initial capacity is lower (469 mAh/g at current density 200 mA/g) and decays faster, to 262 mAh/g after 70 cycles. This represents a capacity retention of only 55%. Comparison experiments with bulk cobalt sulfide compounds prepared by either by direct thermolysis of $Co_6S_8(PEt_3)_6$ (**control-1**) and by solvothermal reaction of $Co(OAc)_2$ (cobalt acetate) and Na_2S (sodium sulfide) (**control-3**)[16] are useful for evaluating the performance of **MS-CoS**. These material lower initial capacities, which fade even faster: the initial capacities for **control-1** and **control-3** are 468 and 372 mAh/g, and decrease to 156 and 35 mAh/g after 100 cycles, respectively

The difference between the microporous and non-porous annealed structures is even more striking when **MS-CoSe** is used as the electroactive material for Na-ion batteries. The **MS-CoSe**/Na cell is initially cycled at a current density of 50 mA/g for three cycles: the initial capacity is 554 mAh/g. The current density is then increased to 200 mA/g for 100 cycles: the capacity starts at 458 mAh/g and decreases to 371 mAh/g at the 100th cycle, for a capacity retention of 81%, a remarkable value for Na-ion batteries.

By comparison, **control-2** has a much lower initial capacities of 399 and 252 mAh/g at current densitites of 50 and 200 mA/g, respectively. The capacity decreases to 10 mAh/g after only 50 cycles. These results indicate that the microporous structure of **MS-CoSe** is critical in determining the electrochemical performance of the material, presumably by enabling transport of the Na$^+$ ions and reducing the lattice strains. This is supported by SEM images of the **MS-CoSe** electrode after 100 cycles, showing intact microspheres.
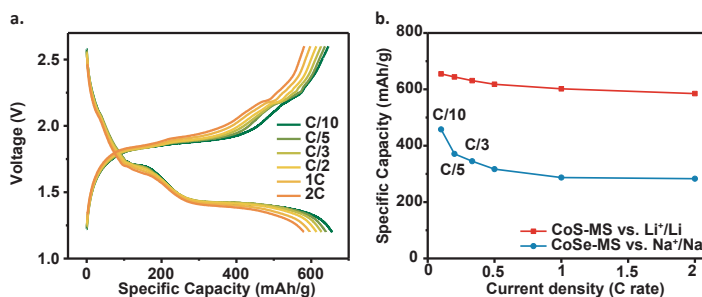
Figure 6.4. Rate capacity of **MS-CoS**/Li and MS-CoSe/Na half-cells. (a) Representative charge and discharge profiles of MS-CoS-Li half-cell at various rates from 0.1 C to 2 C (b) Rate capacity of the **MS-CoS**/Li half-cell and the **MS-CoSe**/Na half-cell at various rates from 0.1 C to 2 C (1 C = 500 mA/g).

The microporosity also improve the power capacity of the materials as ions can access higher surface areas and the diffusion through the solid is reduced. The **MS-CoS**/Li cell delivers capacities of 644, 631, 618, 602, 585 mAh/g at rates of 0.2, 0.33, 0.5, 1, 2 C (1 C = 500 mA/g), respectively, which are 98%, 96%, 94%, 92% of that at 0.1 C (655 mAh/g) (Figure 6.4). The plateaus at 1.4 and 1.7 V are unchanged, indicating that the reaction mechanism remains the same across different current densities (Figure 6.4a). Similarly, the **MS-CoSe**/Na cell shows attractive performance across a wide range of rates, even though the Na$^+$ ions are much larger than Li$^+$ ions. The cell delivers capacities of 371, 345, 317, 287, 283 mAh/g at rates of 0.2, 0.33, 0.5, 1, 2 C, respectively, corresponding to 81%, 75%, 69%, 63%, and 62% of that at 0.1 C (Figure 6.4b). These

120

results show that the high surface area and microporosity of **MS-CoS** and **MS-CoSe** can improve the reaction and ion diffusion kinetics, enabling excellent power capacities.

6.5 Conclusion

The use of cobalt chalcogenide superatomic clusters as precursors tonanostructure cobalt chalcogenide has allowed for the new synthesis of a highly spherical, microporous material. These materials have been demonstrated to have notably performance as battery electro materials and paves the way for a new class of materials that may prove useful in fabrication the next generation of advanced battery materials.

6.6 Synthetic Details

Unless otherwise stated, all reactions and sample preparations were carried out under inert atmosphere using standard Schlenk techniques or in a nitrogen-filled glovebox. $Co_6S_8(P^nBu_3)_6$ and $Co_6Se_8(PEt_3)_6$ were prepared according to previously published protocols. Control samples of CoS were prepared following a literature procedure[1]. The preparation of $Co_6S_8(PEt_3)_6$ has been previously described, but was instead prepared using the method described below.

$Co_6S_8(PEt_3)_6$. In a 200 mL Schlenk flask, elemental sulfur (1.16 g, 0.0362 mol, 3 eq) was suspended and stirred in approximately 30 mL of toluene. In two separate flasks, $Co_2(CO)_8$ (4.12 g, 0.0120 mol, 1 eq) and triethylphosphine (4.27 g, 0.0351 mol, 3 eq) was dissolved in approximately 20 mL of toluene. The solution of $Co_2(CO)_8$ was added to the suspension of elemental sulfur followed by quick addition of the triethylphosphine solution the reaction mixture. The reaction mixture was then refluxed under nitrogen for 2 days. (NOTE: this reaction can be monitored by IR spectroscopy by taking small aliquots from the reaction mixture, removing the solvent, and checking the solid for the

disappearance of the CO stretches.) Next, the reaction mixture was cooled to 100 °C, opened to air, and hot filtered through a bed of Celite. The filtrate was cooled to room temperature and left to stand for approximately 3 hours. This suspension was then filtered through a fine frit and the precipitate washed with toluene, followed by ether. The dark, black crystals were then collected, dried under vacuum, and stored under nitrogen. Yield: 2.2 g (42%). MS-MALDI m/z calculated 1317.9220; found, 1317.9467.

MS-CoS. In a nitrogen-filled glovebox, $Co_6S_8(PEt_3)_6$ (0.900 g, 0.682 mmol, 1 eq) and elemental sulfur (0.131, 4.08 mmol, 6 eq) were suspended approximately 150 mL of toluene in a pressure vessel and sealed with a Teflon cap. The reaction mixture was removed from the glovebox and stirred at 150 °C for 16 hours. After 16 hours, the reaction mixture is a suspension of black solids and a clear, colorless solution. The reaction mixture was then cooled to room temperature and filtered under nitrogen, the precipitate washed with toluene, followed by hexanes. The black powder was then dried under high vacuum. Yield: 0.424 g (102%, assuming stoichiometric removal of PEt_3 from $Co_6S_8(PEt_3)_6$.

MS-CoSe. **MS-CoSe** was prepared using the same method described above for **MS-CoS** above, except replacing $Co_6S_8(PEt_3)_6$ and elemental sulfur with $Co_6S_8(PEt_3)_6$ and elemental (gray) selenium.

control-1, **control-2**. These samples were prepared by loading approximately 30 cm long borosilicate glass tubes (O.D. 0.25 mm, I.D. 3 mm) with $Co_6S_8(PEt_3)_6$ and $Co_6Se_8(PEt_3)_6$, respectively under an inert atmosphere, evacuating, and flame sealing these tubes, and annealing the materials at 400 °C in a tube furnace. A cooler end of

about 1 cm was left outside of the tube furnace to allow condensation of any vapors released by the material.

6.7 References

(1)   Delmon, B.; Grange, P. The Role of Cobalt and Molydenum Sulphides in Hydrodesulphurisation Catalysts: A review. *J. Less. Common. Met.* **1974**, *1,* 353-360.

(2)   Bouwens, S. M. A. M.; Van Veen, J. A. R.; Koningsberger, D. C.; De Beer, V. H. J.; Prins, R. EXAFS Determination of the Structure of Cobalt in Carbon-supported Cobalt and Cobalt-molybdenum Sulfide Hydrodesulfurization Catalysts. *J. Phys. Chem.* **1991**, *95*, 123-134.

(3)   Sun, Y.; Liu, C.; Grauer, D. C.; Yano, J.; Long, J. R.; Yang, P.; Chang, J. S. Electrodeposited Cobalt-Sulfide Catalyst for Electrochemical and Photoelectrochemical Hydrogen Generation from Water. *J. Am. Chem. Soc.* **2013**, *135*, 17699-17702.

(4)   Bonde, J.; Mose, P. G.; Jaramillo, T. F.; Nørskov, J. K.; Chorkendorff, I. Hydrogen Evolution on Nano-Particulate Transition Metal Sulfides. *Faraday Discuss*. **2009**, *140*, 219-231.

(5)   Wang, M.; Anghel, A. M.; Marsan, B.; Ha, N. L. C.; Pootrakulchote, N.; Zakeeruddin, S. M.; Grätzel. CoS Supersedes Pt as Efficient Electrocatalyst for Triiodide Reduction in Dye-Sensitized Solar Cells. *J. Am. Chem. Soc.* **2009**, *131*, 15976-15977.

(6)   Kung, C. W.; Chen, H. W.; Lin, C. Y.; Huang, K. C.; Vittal, R.; Ho, K. C. CoS Acicular Nanorod Arrays for the Counter Electrode of an Efficient Dye-Sensitized Solar Cell. *ACS Nano*. **2012**, *6*, 7016-7025.

(7)   Bao, S. J.; Li, C. M.; Guo, C. X.; Qiao, Y. Biomolecule-Assisted Synthesis of Cobalt Sulfide Nanowires for Application in Supercapacitors. *J. Power Sources*. **2008**, *180*, 676-681.

(8)   Justin, P.; Ranga Rao, G. CoS Spheres for High-Rate Electrochemical Capacitive Energy Storage Application. *Int. J. Hydrog. Energy*. **2010**, *35*, 9709-9715.

(9)   Yang, Z.; Chen, C. Y.; Chang, H. S. Supercapacitors Incorporating Hollow Cobalt Sulfide Hexagonal Nanosheets. *J. Power Sources*. **2011**, *196*, 7874-7877.

(10)   Huang, G.; Chen, T.; Wang, Z.; Chang, K.; Chen, W. Synthesis and Electrochemical Performances of Cobalt Sulfides/Graphene Nanocomposite as Anode Material of Li-Ion Battery. *J. Power Sources*. **2013**, *235*, 122-128.

(11)   Wang, Q.; Jiao, L.; Han, Y.; Du, H.; Peng, W.; Huan, Q.; Song, D.; Si, Y.; Wang, Y.; Yuan, H. CoS_2 Hollow Spheres: Fabrication and Their Application in Lithium-Ion Batteries. *J. Phys. Chem. C*. **2011**, *115*, 8300-8304.

(12)   Wang, Y.; Wu, J.; Tang, Y.; Lü, X.; Yang, C.; Qin, M.; Huang, F.; Li, X.; Zhang, X. Phase-Controlled Synthesis of Cobalt Sulfides for Lithium Ion Batteries. **2012**, *ACS Appl. Mater. Interfaces*, **2012**, *4*, 4246-4250.

(13)   Wang, J.; Ng, S. H.; Wang, G. X.; Chen, J.; Zhao, L.; Chen, Y.; Liu, H. K. Synthesis and Characterization of Nanosize Cobalt Sulfide for Rechargeable Lithium Batteries. *J. Power Sources*. **2006**, *159*, 287-290.

124

(14)   Wu, C.; Jiang, Y.; Kopold, P.; van Aken, P. A.; Maier, J.; Yu, Y. Peapod-Like Carbon-Encapsulated Cobalt Chalcogenide Nanowires as Cycle-Stable and High-Rate Materials for Sodium-Ion Anodes. *Adv. Mater.* **2016**, *28*, 7276-7283.

(15)   Matsuzaki, R.; Yajima, A.; Eguchi, M.; Saeki, Y. The Formation Process of Cobalt Sulfide from Tricobalt Tetraoxide Using Sulfur Dioxide as a Sulfidizing Agent. *Bull. Chem. Soc. Jpn.* **1982**, *55*, 1480-1483.

(16)   Zhan, J. H., Xie, Y.; Yang, X. G.; Zhang, W. X., Qian, Y. T. Hydrazine-Assisted Low-Temperature Hydrothermal Preparation of Nanocrystalline Jaipurite. *J. Solid State Chem.* **1999**, *146*, 36-38.

(17)   McDowell, M. T.; Lee, S. W.; Harris, J. T.; Korgel, B. A.; Wang, C.; Nix, W. D.; Cui, Y. In Situ TEM of Two-Phase Lithiation of Amorphous Silicon Nanospheres. *Nano Lett.* **2013**, *13*, 758-764.

(18)   Claridge, S. A.; Castleman, A. W.; Khanna, S. N.; Murray, C. B.; Sen, A.; Weiss, P. S. Cluster-Assembled Materials. *ACS Nano.* **2009**, *3*, 244-255.

(19)   Pinkard, A.; Champsaur, A. M.; Roy, X. Molecular Clusters: Nanoscale Building Blocks for Solid-State Materials. *Acc. Chem. Res.* **2018**, *51*, 919-929.

(20)   Brenna, J. G.; Siegrist, T.; Stuczynski, S. M.; Steigerwald, M. L. The Transition From Molecules to Solids: Molecular Syntheses of $Ni_9Te_6(PEt_3)_8$, $Ni_{20}Te_{18}(PEt_3)_{12}$ and NiTe. *J. Am. Chem. Soc.* **1989**, *111*, 9240-9241.

(21)   Stucyzynski, S. M.; Kwon, Y. U.; Steigerwald, M. L. The Use of Phosphine Chalcogenides in the Preparation of Cobalt Chalcogenides. *J. Organomet. Chem.* **1993**, *449*, 167-172.

(22)   Champsaur, A. M.; Hochuli, T. J.; Paley, D. W.; Nuckolls, C.; Steigerwald, M. L. Superatom Fusion and the Nature of Quantum Confinement. *Nano Lett.* **2018**, *18*, 4564-4569.

(23)   Sing, K. S. W.; Everett, D. H.; Haul, R. A. W.; Moscou, L.; Pierotti, R. A.; Rouquerol, P.; Siemieniewska, T. Pure. Appl. Chem. **1985**, *57*, 603-619.

(24)   Peng, S.; Han, X.; Li, L.; Zhu, Z.; Cheng, F.; Srinivansan, M.; Adams, S.; Ramakrishna, S. Unique Cobalt Sulfide/Reduce Graphene Oxide Composite as an Anode for Sodium-Ion Batteries with Superior Rate Capability and Long Cycling Stability. **2016**, *10*, 1359-1368.